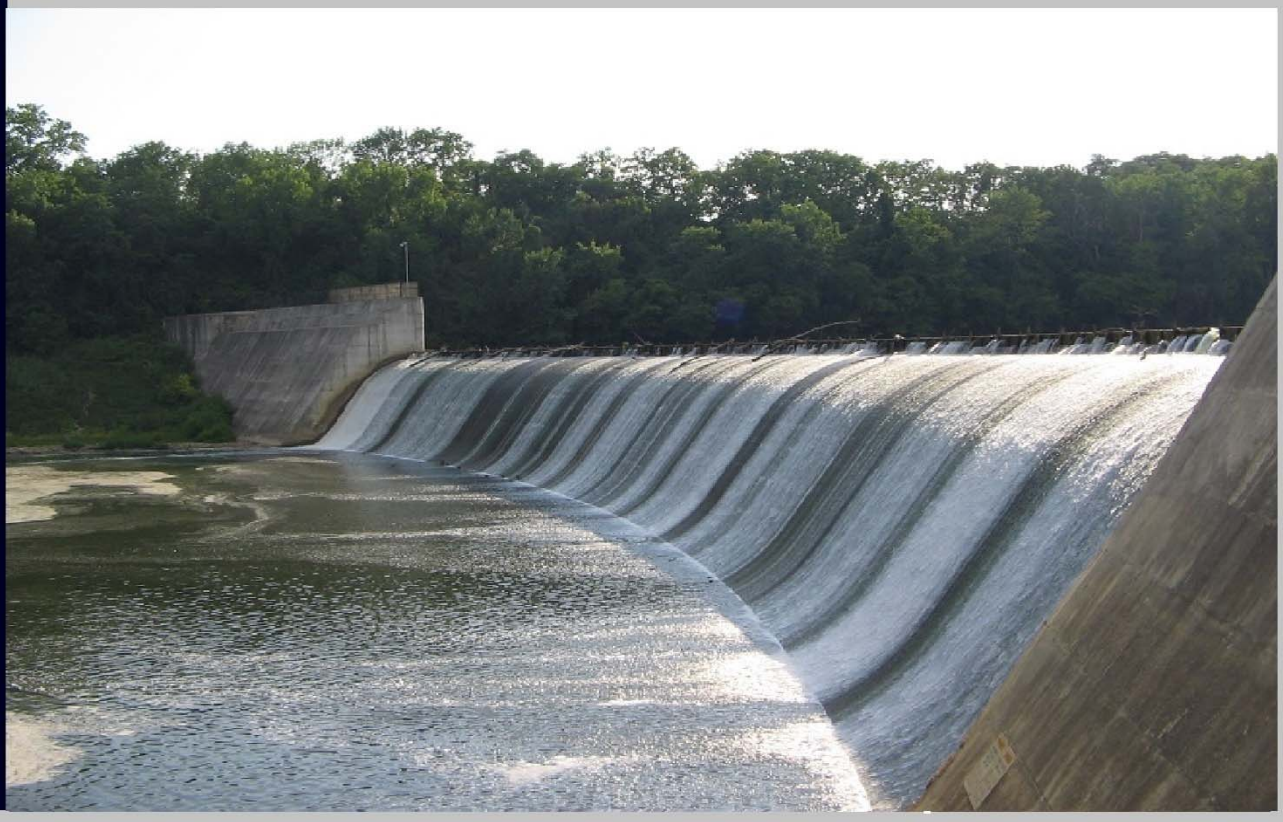
Volume 4 | Issue 1 | Summer 2018

انجمن هیدرولیک ایران
Iranian Hydraulic Association

Shahid Chamran University of Ahvaz

Journal of
Hydraulic Structures

Scientific Professional Journal



ISC
Islamic World Science Citation Center
نشریه علمی پژوهشی

ISSN 2345-413X
http://jhs.scu.ac.ir

In the name of GOD

Journal of Hydraulic Structures
Department of Civil Engineering
Faculty of Engineering
Shahid Chamran University of Ahvaz

JORNAL OF
HYDRAULIC STRUCTURES
SHAHID CHAMRAN UNIVERSITY OF AHVAZ

Manager: *Prof. Hamid R. Ghafouri*
Editor-in-chief: *Dr. Ali Haghighi*
Editorial coordinator: *Dr. Seyed Mohammad Ashrafi*
Department of Civil Engineering, Faculty of Engineering, Shahid Chamran University of Ahvaz, Ahvaz, Iran.

Members
Prof. Hossein M. V.Samani
Civil Engineering Department, Shahid Chamran University of Ahvaz, Ahvaz, Iran
Prof. Hamid R. Ghafouri
Civil Engineering Department, Shahid Chamran University of Ahvaz, Ahvaz, Iran
Dr. Ali Haghighi
Civil Engineering Department, Shahid Chamran University of Ahvaz, Ahvaz, Iran
Prof. Mahmood S. Bajestan
Hydraulic Structures Department, Shahid Chamran University of Ahvaz, Ahvaz, Iran
Prof. Saeed R. S. Yazdi
Civil Engineering Department, K.N.Toosi University of Technology, Tehran, Iran
Dr. Mohammad S. Pakbaz
Civil Engineering Department, Shahid Chamran University of Ahvaz, Ahvaz, Iran
Dr. Arash Adib
Civil Engeering Department, Shahid Chamran University of Ahvaz, Ahvaz, Iran
Dr. Mojtaba Labibzadeh
Civil Engineering Department, Shahid Chamran University of Ahvaz, Ahvaz, Iran
Prof. Helena M. Ramos
Instituto Superior Técnico (IST), University of Lisbon
Dr. S. Mohammad Ashrafi
Civil Engineering Department, Shahid Chamran University of Ahvaz, Ahvaz, Iran
Dr. S. Abbas Haghshenas
Institute of Geophysics, University of Tehran | UT, Tehran, Iran
Dr. Mohammad Zounemat-Kermani
Department of Water Engineering, Shahid Bahonar University of Kerman, Kerman, Iran
Dr. Taher Rajaee
Civil Engineering Department, University of Qom, Qom, Iran
Dr. Mohammad Vaghefi
Civil Engineering Department, Faculty of Engineering, Persian Gulf University, Bushehr, Iran
Dr. A. A. Telvari
Soil Conservation and Watershed Management Research Institute; Department of Civil Engineering, Islamic Azad University, Ahvaz branch, Ahvaz, Iran

Shahid Chamran University of Ahvaz

Iranian Hydraulic Association

CONTENTS

VOL 4, Issue 1, Summer 2018

I. ***In the name of God***

II. ***Table of Contents***

III. ***Aims and Scope***

01 Development of a Direct Explicit Equation for Hydraulic Design of Semi-elliptical Channels
H. Nikroy Motlagh; Hossein M.V. Samani; H. Hassanpour Darvishi

08 An Alternating Direction Implicit Method for Modeling of Fluid Flow
I. Saeedpanah; A. Adib

19 Wave Evolution in Water Bodies using Turbulent MPS Simulation
H. Imanian; M. Kolahdoozan; A.R. Zarrati

36 Ocean Currents Modeling along the Iranian Coastline of the Oman Sea and the Northern Indian Ocean
M. Jedari Attari; S.A. Haghshenas; A. Bakhtiari; M.H. Nemati

55 Study of Streamlines under the Influence of Displacement of Submerged Vanes in Channel Width, and at the Upstream Area of a Cylindrical Bridge Pier in a 180 Degree Sharp Bend
C.A. Chooplou; M. Vaghefi; S.H. Meraji

75 Frequency domain analysis of transient flow in pipelines; application of the genetic programming to reduce the linearization errors
M.M. Riyahi; M. Rahmanshahi; M.H. Ranginkaman

Aims and Scope

Hydraulic Structure Journal is an interdisciplinary journal which publishes high-quality peer-reviewed articles addressing the latest developments and applied methods **in construction, maintenance, management, and operation policy of Hydraulic Structures.**
The Journal aims at providing an efficient route to fast-track publication, **within 10-12 weeks after manuscript submission**. Manuscripts will be considered for publication in the following categories: **research articles**, **technical notes**, **case reports** and **discussions**.

The general areas covered by the Journal include:

- Technical and methodological advances in application, design/selection, production, modification of construction materials
- Advances in numerical and analytical methods
- Hydro informatics and soft computing
- Hydraulic aspects of hydraulic structures
- Applied surface and subsurface hydrology and hydrometeorology
- Forecasting approaches in water resources engineering
- Economic and social aspects of hydraulic structures
- Uncertainty analysis and risk management in hydraulics and water resources engineering
- Application of Nanotechnology in Hydraulic Structures
- Geotechnics of Hydraulic Structures
- Damage detection techniques

The following might be considered as hydraulic structures:

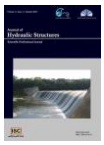
- Dams and associated structures
- River and Watershed Structures
- Offshore and Onshore Structures
- Irrigation and Drainage Channel Networks
- Bridges
- Water Storage and Conveyance Structures
- Pipelines and Pump Stations
- Sewerage Systems
- Water and Wastewater Treatment Plants
- Historical Water Structures

General Information

Title: Journal of Hydraulic Structures
Subject: Hydraulics and water resources engineering
Coverage area: International
Journal Type: Scientific and technical
License Holder: Shahid Chamran University of Ahvaz
Editor-in-Chief: Dr. Ali Haghighi
Manager: Prof. Hamid R. Ghafouri
Editorial coordinator: Dr. Seyed Mohammad Ashrafi

Language Editors:
Majid SadollahKhani
Soroosh Kamali
Address: Department of Civil Engineering, Faculty of Engineering, Shahid Chamran University of Ahvaz
Phone #: +986133330011-19 (5610 & 5603)
Fax #: +986113337010
Language: English
Email: jhs@scu.ac.ir
Website: jhs.scu.ac.ir

Journal of Hydraulic Structures
***J. Hydraul. Struct.*, 2018; 4(1):1-7**
DOI: 10.22055/JHS.2018.24972.1066



OPEN ACCESS

Development of a Direct Explicit Equation for Hydraulic Design of Semi-elliptical Channels

Hossein Nikroy Motlagh[1]
Hossein M. V. Samani[2]
Hossein Hassanpour Darvishi[3]

Abstract

One of the common concrete channels in irrigation networks is the semielliptical prefabricated channels. Manning formula is usually used to design these channels. The cross-sectional area and the wetted perimeter are required to be calculated in Manning formula. There are no analytical solutions to directly compute these parameters. Thus, numerical integration methods are inevitably used. In this paper, a wide number of various semielliptical channels are regarded and their cross-sectional areas and wetted perimeters for different depths were computed numerically to produce databases for three-dimensional curve fitting. Direct relationships for the cross-sectional area and the wetted perimeter in terms of the channels size and the hydraulic parameters were developed. These relationships were used in the design of the semielliptical concrete channels and the results were compared with the numerical ones. The results were quite close to each other.

Keywords: semielliptical, Manning formula, Numerical method, correlation coefficient

Received: 11 February 2018; Accepted: 10 April 2018

1. Introduction

Now a day, prefabricated concrete channels are widely used in irrigation networks. These channels are constructed in various shapes. This includes traditional sections such as trapezoidal ones [1, 2, 3, 4] and parabolic sections [5, 6, 7]. One of the other channel sections used is the elliptic sides with horizontal bottoms [8]. The semielliptical concrete channels have been

[1] Graduate student, Water Resources Engineering Department, Faculty of Engineering, Shahr Qods Islamic Azad University, Shahr Qods, Tehran.
[2] Professor, Water Resources Engineering Department, Faculty of Engineering, Shahr Qods Islamic Azad University, Shahr Qods, Tehran. (**Corresponding author**)
[3] Associated Professor, Water Resources Engineering Department, Faculty of Engineering, Shahr Qods Islamic Azad University, Shahr Qods, Tehran.

CC BY

recently widely utilized in irrigation projects. They have the advantages of reducing of the constructional cost and land acquisition, reducing evaporation by having smaller water surface widths, reducing sedimentation and they can be constructed fast [9, 10, 11, 12]. There are no explicit direct solutions for the semielliptical cross sections and the wetted perimeters to be used in Manning formula. Vatankhah [12], used a numerical method to calculate the integrals of the cross-section and the wetted perimeter.

In this research, explicit direct relationships for the cross-sectional area and the wetted perimeter of the semielliptical channels are found by using three-dimensional regression analysis. Then, they were used in Manning formula for design purposes.

2. Design Method

Manning formula is used for the design of the semielliptical channels as follows:

$$Q = \frac{1}{n} R^{2/3} A S_0^{1/2} \tag{1}$$

Where:

Q = Flow discharge

n = Manning coefficient

R = Hydraulic radius which is equal to the ratio of the flow cross-sectional area, A, to the wetted perimeter, P

S_0 = Channel bed slope

The flow discharge, Manning coefficient, and the channel bed slope are known. There are many prefabricated concrete semielliptical channels available in the market. The economic optimum design of the semielliptical channel should have the capacity to carry the flow with a limited freeboard. A computer program is developed in this regard in which all the prefabricated available channel sizes are used in the calculation and then the smallest size that is able to pass the flow properly is chosen. The integrals of the cross-sectional areas and the wetted perimeters are calculated by using the trapezoidal rule.

3. Calculation of Flow Cross Sectional Area and Wetted-Perimeter

Figure 1 depicts a typical semielliptical cross-section in which ***a*** and ***b*** are the horizontal and vertical radii of the ellipse, respectively. The cross-section is symmetrical with respect to the **y**-axis. Hence, it is possible to calculate half of the total cross section and then multiplies that by 2 to obtain the total cross-sectional area. The half cross-section is divided into several elements as shown in the figure. Each element is assumed to be trapezoidal. The coordinates of the intersections of the vertical lines of the elements with the elliptical curve of the channel wall can be determined by the equation:

$$\frac{(x-x_0)^2}{a^2} + \frac{(y-y_0)^2}{b^2} = 1 \tag{2}$$

In which x_0 and y_0 are the coordinates of the ellipse center. It is clear that the summation of the trapezoids areas will produce the area of the half of the total flow cross sectional area.

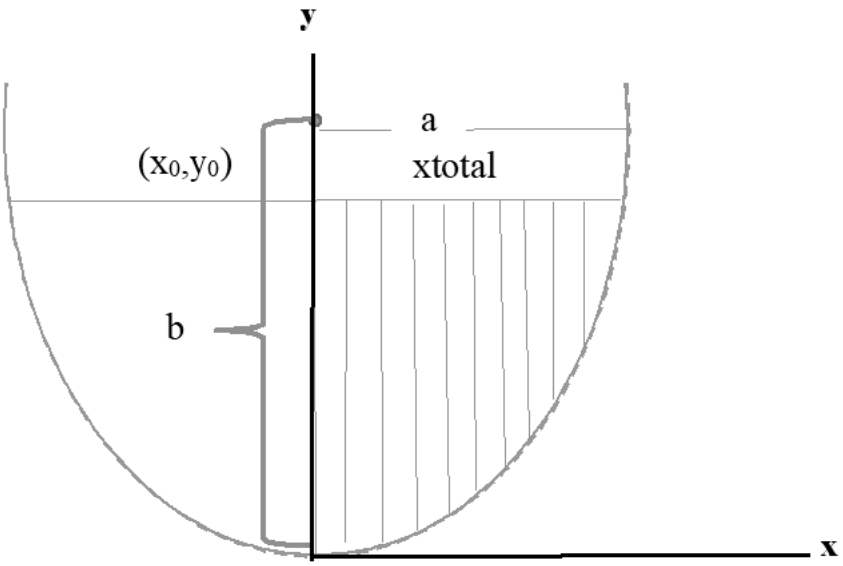


Figure 1. Flow Cross Sectional Area in the Semi-elliptical Channel

The wetted perimeter of each element depicted in Figure 1 can be calculated by the following equation:

$$\Delta L_i = \sqrt{(\Delta x)^2 + (\Delta y)^2} = \sqrt{(x_{i+1} - x_i)^2 + (y_{i+1} - y_i)^2} \quad (3)$$

In which (x_i, y_i) and (x_{i+1}, y_{i+1}) are the coordinates of two sequential points of the ellipse shown in Figure 1. The summation of ΔL_i s results in half of the total wetted perimeter. As an example, semielliptical prefabricated concrete types are considered for the design of a channel to carry out 500 L/s and the bed slope is 0.0005. Manning coefficient is regarded as 0.015. The results of the developed computer program are introduced in Table 1.

Table1. Semielliptical channel types for the given example

Type	Depth (cm)	*b*(cm)	*a*(cm)	n	Q(L/s)	Qcalc(L/s)	Bed Slope
70	26.4	33.4	27.7	0.015	500	15.1609	0.0005
80	28.7	35.7	29.6	0.015	500	18.6132	0.0005
100	32.9	39.9	32.9	0.015	500	25.8852	0.0005
120	36.7	43.7	36	0.015	500	33.9412	0.0005
135	39.4	46.4	38.1	0.015	500	40.3424	0.0005
150	41.9	48.9	40	0.015	500	46.8109	0.0005
180	44.6	51.6	45.4	0.015	500	61.1335	0.0005
200	45.6	52.6	49.4	0.015	500	71.2627	0.0005
230	48.8	55.8	53.5	0.015	500	87.2413	0.0005
250	48.9	55.9	58	0.015	500	98.5231	0.0005
280	50.5	57.5	63	0.015	500	115.764	0.0005
315	52.3	59.3	69	0.015	500	138.064	0.0005

350	53.9	60.9	74.6	0.015	500	160.501	0.0005
400	55.6	62.6	82.8	0.015	500	193.766	0.0005
450	56.1	63.1	92.2	0.015	500	227.925	0.0005
520	56.5	63.5	105.6	0.015	500	277.212	0.0005
600	58.2	65.2	118.7	0.015	500	337.818	0.0005
700	62.8	69.8	135.6	0.015	500	447.656	0.0005
800	**64.62604954**	74.4	144.7	0.015	500	500	0.0005
900	**62.74162577**	78.7	153.4	0.015	500	500	0.0005
1000	61.23847894	82.8	161.6	0.015	500	500	0.0005

The first column of Table 1 represents the channel type and the calculated flow depths are given in the second column. The third and fourth columns represent the vertical and horizontal radii, respectively. The seventh column represents the calculated flow corresponds to the channel size types. The results show that channel types 70 to 700 are too small to pass the given flow and types 800, 900, and 1000 are able to pass the flow. It is clear that type 800 is the economical one which should be regarded as a final design.

4. Explicit Relationships for the Flow Cross Sectional Area and the Wetted Perimeter

In order to develop explicit direct relationships for the flow cross-sectional area and the wetted perimeter, a large number of condition combinations of semielliptical channels with various hydraulic conditions are considered. The developed computer program is applied to all these combinations similar to that which is shown in Table 1. Based on the obtained results the dimensionless flow cross-sectional area A/ab is regarded as a function of the dimensionless variables y/a, y/b and the least squares method was used to obtain the best fitted function. This task was done by the Table-curve 3D software. The results indicated that A/ab is only a function of y/b and the best-fitted function is obtained as:

$$\frac{A}{ab} = e^{0.552486-0.111776(y/b)^2+1.46526Ln(y/b)} \quad (4)$$

The correlation coefficient for the above function is calculated as $r^2 = 0.99999994$. Similarly, the dimensionless wetted perimeter $L/\sqrt{a^2+b^2}$ is considered as a function of the dimensionless variables y/a, y/b and the best-fitted function is obtained as:

$$\frac{L}{\sqrt{a^2+b^2}} = \frac{0.413705}{\sqrt{y/a}} + 3.2257358\sqrt{y/b} - 1.3992385 \quad (5)$$

The correlation coefficient for the function given in Equation (5) is calculated as $r^2 = 0.99999994$.

Substituting the calculated functions for the flow cross-sectional area and the wetted perimeter given by Equations (4) and (5), respectively, in Manning equation results in:

$$Q=\frac{1}{n}\left(\frac{abe^{0.552486-0.111776(y/b)^2+1.46526Ln(y/b)}}{\sqrt{a^2+b^2}\left(\frac{0.413705}{\sqrt{y/a}}+3.2257358\sqrt{y/b}-1.3992385\right)}\right)^{2/3} abe^{0.552486-0.111776(y/b)^2+1.46526Ln(y/b)}\sqrt{S_0} \quad (6)$$

The developed equation (6) can be used simply for the design of semielliptical channels.

5. Evaluation of the Developed Equation

Various semielliptical channels with different slopes are considered and the flow discharges are calculated by two methods, the developed equation [Equation (6)] and the numerical trapezoidal method. The results are given in Table 2. Column 7 represents the difference percent between the developed and numerical methods. It is noted that the differences are very small which proves that the developed equation has the desired accuracy.

Table2. Percent of differences Between the Developed Equation and The Numerical Method

Depth (cm)	*a*	*b*	Bed Slope *S*	*n*	*Q* Eq.(6)	Q(Numerical)	Error %
46.23724	0.315	0.575	0.0005	0.015	99.9	99.99	0.10001
43.25029	0.345	0.593	0.0005	0.015	99.59	99.99	0.414032
51.95147	0.461	0.631	0.0005	0.015	200.17	200	0.08504
46.93797	0.528	0.635	0.0005	0.015	199.86	200	0.067927
54.36399	0.5935	0.652	0.0005	0.015	299.2	300	0.268229
58.88418	0.678	0.698	0.0005	0.015	398.07	400.00	0.484581
64.62605	0.7235	0.744	0.0005	0.015	497.41	500.00	0.520581
62.74163	0.767	0.787	0.0005	0.015	497.97	500	0.406979
69.53065	0.767	0.787	0.0005	0.015	596.76	600	0.542812
67.69017	0.808	0.828	0.0005	0.015	597.29	600	0.454458
46.67753	0.29	0.559	0.0006	0.015	100.05	100	0.05304
43.82707	0.315	0.575	0.0006	0.015	99.65	100	0.350047
53.65199	0.414	0.626	0.0006	0.015	200.52	200	0.258765
49.30414	0.461	0.631	0.0006	0.015	199.98	200	0.01005
56.09775	0.528	0.635	0.0006	0.015	300.01	300	0.003339
51.65093	0.5935	0.652	0.0006	0.015	299.32	300	0.22821
55.95632	0.678	0.698	0.0006	0.015	398.38	400	0.407195
61.38002	0.7235	0.744	0.0006	0.015	497.72	500	0.457451
66.01671	0.767	0.787	0.0006	0.015	597.08	600	0.488993
70.12686	0.808	0.828	0.0006	0.015	696.47	700	0.506404
75.71512	0.808	0.828	0.0006	0.015	795.54	800	0.560142

6. Summary and Conclusions

A new explicit equation for the hydraulic design of the semielliptical channels has been developed in this research. In this regard, a computer program has been initially prepared in which the flow discharge is calculated by the Manning formula and the flow cross-sectional area

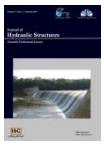
and the wetted perimeters are calculated by using the trapezoidal numerical integration method. A large number of the database include the flow discharges against the channel characteristics were provided by the developed computer program. The database was converted to dimensionless parameters for the cross-sectional area and the wetted perimeter versus other dimensionless hydraulic parameters and then the Table-curve 3D software was utilized to obtain the best functions which fit the data using the least square method. As a result, explicit direct equations were obtained whose correlation coefficients are equal to almost unity which indicate that the fitted functions have desired accuracies. The accuracy of the developed final equation of the Manning formula was tested by comparing its results with those obtained by the numerical integration method. The results indicate close agreement with each other which shows that the developed explicit direct Manning equation can be used for the purpose of semielliptical channel design with a proper accuracy.

7. References

1. Guo, C. and Hughes, W. (1984). “Optimal channel cross-section with freeboard.” Journal of Irrigation and Drainage Engineering, Vol. 110, No. 3, pp. 304-314, DOI: 10.1061/(ASCE)0733-9437(1984)110:3(304).
2. Frochlich, D. C. (1994). “Width and depth constrained best trapezoidal section.“ Journal of Irrigation and Drainage Engineering, Vol. 120, No. 4, pp. 828-835, DOI: 10.1061/(ASCE) 0733-9437 (1994)120:4(828).
3. Jain, A., Bhattachariya, R. K. and Sanaga, S. (2004). “Optimal design of composite channels using a genetic algorithm. “Journal of Irrigation and Drainage Engineering, Vol. 130, No. 4, pp. 286-295. DOI: 10.1061/(ASCE)0733-9437(2004)130:4(286).
4. Bhattachariya, R. K., and Satish, M. G. (2007). “Optimal design of a stable trapezoidal cross section using hybrid optimization technique.” Journal of Irrigation and Drainage Engineering, Vol. 133, No. 4, pp. 323-329, DOI: 10.1061/(ASCE) 0733-9437 (2007) 133:4(323).
5. Longanathan, G. V. (1991). “Optimal design of parabolic canals.” Journal of Irrigation and Drainage Engineering, Vol. 1117, No. 5, pp. 716-735, DOI: 10.1061/(ASCE) 0733-9437 (1991)117:5(716).
6. Chahar, B. R. (2005). “Optimal design of parabolic canal section.” Journal of Irrigation and Drainage Engineering, Vol. 131, No. 6, pp. 546-554, DOI: 10.1061/(ASCE) 0733-9437 (2005)131:6(546).
7. Aksoy, B. and Altan-Sakarya, A. (2006). “Optimal lined channel Design.” Canadian Journal of Civil Engineering, Vol. 33, No. 5, pp. 535-545, DOI: 10.1139/106-008.
8. Easa, S. M. (2016). “Versatile general elliptic open channel cross section.” Korean Journal of Civil Engineering, Vol. 20, No. 4, pp. 1572-1581, DOI: 10.1007/s12205-008-8045-3.
9. Park, S. K., Ji, U., Yeo, W., and Kim, D. (2013). “Analysis for the effectiven1134-y.
10. Kang, H. (2013). “Flow characteristics and morphological changes in open-channel flow with ultimate vegetation zones. “ Korean Journal of Civil Engineering, Vol. 17, No. 5, pp. 1157-1165, DOI: 10:1007/s12205-013-0346-5.

11. Dey, S. and Papanicolaou, A. (2008). “Sediment threshold under streamflow: A state-of-the-art review.“ Korean Journal of Civil Engineering, Vol. 12, No. 1, pp. 45-60, DOI: 10.1007/s12205-015-0494-x.
12. Vatankhah, A. R., Ghafari, S., Mahdavi, M. A. (2015). "New and improved hydraulic radius for channels of the second kind." Ain Shams Engineering Journal, 6, 767-773.

Journal of Hydraulic Structures
***J. Hydraul. Struct.*, 2018; 4(1):8-18**
DOI: 10.22055/JHS.2018.24452.1061



OPEN ACCESS

An alternating direction implicit method for modeling of fluid flow

Iraj Saeedpanah[1]
Arash Adib[2]

Abstract

This research includes of the numerical modeling of fluids in two-dimensional cavity. The cavity flow is an important theoretical problem. In this research, modeling was carried out based on an alternating direction implicit via Vorticity-Stream function formulation. It evaluates different Reynolds numbers and grid sizes. Therefore, for the flow field analysis and prove of the ability of the scheme, the numerical solution was carried out for different values of the Reynolds numbers. Also, the behavior of the vortex flow in cavity was predicted. This research compares results of applied numerical model with the results of Chia et al. [1] and Chen & Pletcher [2]. Comparing the results with those of the benchmarks show that alternating direction implicit is an effective and suitable formulation for the solution of the Navier–Stokes equations.

Keywords: Alternating direction implicit, Unsteady 2-D incompressible N-S equation, Two-dimensional, Cavity, Vortex flow

Received: 26 December 2017; Accepted: 22 April 2018

1. Introduction

Developing numerical methods for solving the Navier-Stokes equations (NSE) has its own challenges and difficulties. Also, the development of numerical methods to simulate fluid flows with applications has been a research area of great progress over the past half-century. The very common schemes used in computational fluid dynamics could be divided into three categories as: finite difference methods (FDM), finite element methods (FEM) and finite volume methods (FVM). Investigation about hydraulic structures is an interesting subject. Therefore, there are many studies which examine the hydraulic structures in different geometries. Driesen et al. [3] analyzed the flow pattern in a cavity. This problem thus is a good test for experimental flow

[1] Assistant Professor, Department of Civil Engineering, Faculty of Engineering, University of Zanjan, Zanjan, Iran. (*Corresponding author, saeedpanah@znu.ac.ir)
[2] Associate Professor, Department of Civil Engineering, Shahid Chamran University of Ahvaz, Ahvaz, Iran

CC BY

research [4–7]. Gurcan [8] researched about the effect of the Reynolds number on streamline cavity with free surfaces. An incompressible flow behavior inside the different triangular cavities is also presented in [7]. In addition, other researchers such as Agarwal [10], Ghia et al. [1], Chen and Pletcher [2] have studied about the numerical solution of NSE. The most recent works carried out in this regard are those by Ghia & Shin and Chen. They have analyzed the flow field in a cavity for the examination of their solution with different Reynolds numbers. Consequently, in this research, also, flow field in a cavity was taken as the case study, so that, the results of the simulations could be compared with the results of the simulations done by other researchers. According to Anderson et al. [11], the cavity is an excellent test for the solution of NSE for an incompressible fluid flow. This case of flow is important for inspection of the results from the view point of the ability of the scheme to predict complex of the flow fields. Moreover, in the case of flow in a cavity, vortex flow in a bounded geometry is created. Simulation of such a flow is of vital importance from the view point of applications of this type of flow. In this research, analysis of flow field in a cavity with Reynolds number of 100, 400, 1000 and 2000 was carried out by solving NSE.

2. Methodology

The problem considers incompressible flow in a cavity with an upper lid moving with a velocity U as shown in Figure 1.

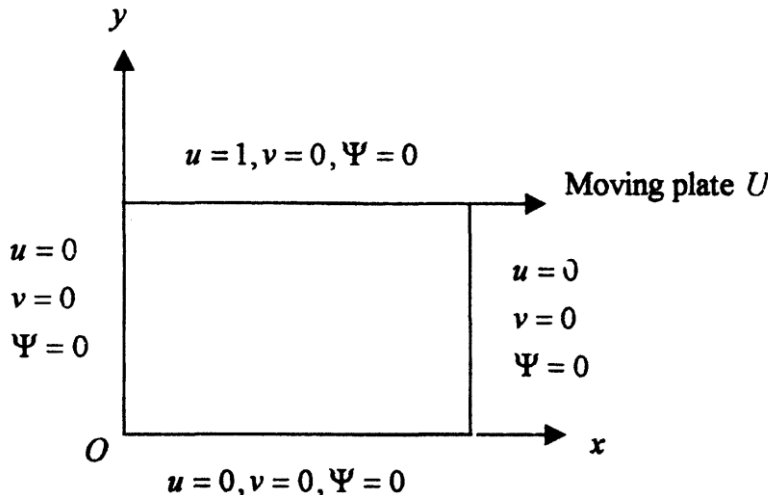


Figure 1. Schematic of the cavity flow

The general non-dimensional, non conservative form of NSE:

$$\frac{\partial u}{\partial x}+\frac{\partial v}{\partial y}=0$$

$$\frac{\partial u}{\partial t}+u\frac{\partial u}{\partial x}+v\frac{\partial u}{\partial y}+\frac{\partial p}{\partial x}=\frac{1}{\mathrm{Re}}\left[\frac{\partial^2 u}{\partial x^2}+\frac{\partial^2 u}{\partial y^2}\right] \tag{1}$$

$$\frac{\partial v}{\partial t}+u\frac{\partial v}{\partial x}+v\frac{\partial v}{\partial y}+\frac{\partial p}{\partial y}=\frac{1}{\mathrm{Re}}\left[\frac{\partial^2 v}{\partial x^2}+\frac{\partial^2 v}{\partial y^2}\right]$$

Application of certain mathematics operations on the Eqs, (1), (2) and (3) for the purpose of obtaining a Vorticity–Stream function formulation, the above equations are given in the following form as

$$\frac{\partial \Omega}{\partial t} + u\frac{\partial \Omega}{\partial x} + v\frac{\partial \Omega}{\partial y} = \frac{1}{\mathrm{Re}}\left[\frac{\partial^2 \Omega}{\partial x^2} + \frac{\partial^2 \Omega}{\partial y^2}\right] \tag{2}$$

$$\frac{\partial^2 \psi}{\partial x^2} + \frac{\partial^2 \psi}{\partial y^2} = -\Omega \tag{3}$$

which are of parabolic and elliptic type, respectively.

An important advantage of this formulation is that pressure is not appeared in the above equations explicitly. So, the Vorticity–Stream function formulation does not contain the pressure term.

$$u = \frac{\partial \psi}{\partial y} \quad , \quad v = -\frac{\partial \psi}{\partial x} \tag{4}$$

$$\frac{\partial^2 p}{\partial x^2} + \frac{\partial^2 p}{\partial y^2} = 2\left[\left(\frac{\partial^2 \psi}{\partial x^2}\right)\left(\frac{\partial^2 \psi}{\partial y^2}\right) - \left(\frac{\partial^2 \psi}{\partial x \partial y}\right)^2\right] \tag{5}$$

Using numerical formulation of Vorticity-Stream function and employing the ADI scheme and Eq. (11), the velocity field is computed.

2.1. Discretization of vorticity equation

With regard to the fact that Eq. (4) is of parabolic type, this equation is discretized using the ADI scheme resulting in the efficient use of the nodes from the entire boundary. This provides high accuracy and more physical adaptation of the solution. More over with this scheme, three diagonal sets of equations are solved instead of five diagonal sets of equations. There is possibility of selection of better space and time steps and unconditional stability exists. Solution of ADI formulation gives the two following equations which are solved successively:

$$\frac{(\Omega_{i,j}^{n+1/2} - \Omega_{i,j}^{n})}{\Delta t/2} + U_{i,j}^{n}\frac{\Omega_{i+1,j}^{n+1/2} - \Omega_{i-1,j}^{n+1/2}}{2\Delta x} + V_{i,j}^{n}\frac{\Omega_{i,j+1}^{n} - \Omega_{i,j-1}^{n}}{2\Delta y} = \frac{1}{\mathrm{Re}}\frac{\Omega_{i+1,j}^{n+1/2} - 2\Omega_{i,j}^{n+1/2} + \Omega_{i-1,j}^{n+1/2}}{(\Delta x)^2} + \frac{1}{\mathrm{Re}}\frac{\Omega_{i,j+1}^{n} - 2\Omega_{i,j}^{n} + \Omega_{i,j-1}^{n}}{(\Delta y)^2} \tag{6-a}$$

$$\frac{(\Omega_{i,j}^{n+1} - \Omega_{i,j}^{n+1/2})}{\Delta t/2} + U_{i,j}^{n+1/2}\frac{\Omega_{i+1,j}^{n+1/2} - \Omega_{i-1,j}^{n+1/2}}{2\Delta x} + V_{i,j}^{n+1/2}\frac{\Omega_{i,j+1}^{n+1} - \Omega_{i,j-1}^{n+1}}{2\Delta y} = \frac{1}{\mathrm{Re}}\frac{\Omega_{i+1,j}^{n+1/2} - 2\Omega_{i,j}^{n+1/2} + \Omega_{i-1,j}^{n+1/2}}{(\Delta x)^2} + \frac{1}{\mathrm{Re}}\frac{\Omega_{i,j+1}^{n+1} - 2\Omega_{i,j}^{n+1} + \Omega_{i,j-1}^{n+1}}{(\Delta y)^2} \tag{6-b}$$

In linearization of Eq. (6), values of u and v are used in the time step n. In this case, it would not be necessary to solve the stream function at n+1/2 time step, otherwise, if u and v are to be used at time step n+1/2, they have to be computed at n+1/2 time step. Consequently, linearization of u and v at time step n leads to considerable decrease of computational costs. With those assumptions Eq. (6) is rewritten as

$$-\frac{1}{2}\left(\frac{1}{2}C_x+d_x\right)\Omega_{i-1,j}^{n+½}+\left(1+d_x\right)\Omega_{i,j}^{n+½}+\frac{1}{2}\left(\frac{1}{2}C_x-d_x\right)\Omega_{i+1,j}^{n+½}=D_x \quad (7\text{-a})$$

$$-\frac{1}{2}\left(\frac{1}{2}C_y+d_y\right)\Omega_{i,j-1}^{n+1}+\left(1+d_y\right)\Omega_{i,j}^{n+1}+\frac{1}{2}\left(\frac{1}{2}C_y-d_y\right)\Omega_{i,j+1}^{n+1}=D_y \quad (7\text{-b})$$

where the Courant and diffusion numbers are defined as

$$C_x=u\frac{\Delta t}{\Delta x} \quad , \quad C_y=v\frac{\Delta t}{\Delta y}$$

$$d_x=\frac{1}{\mathrm{Re}}\frac{\Delta t}{(\Delta x)^2} \quad , \quad d_y=\frac{1}{\mathrm{Re}}\frac{\Delta t}{(\Delta y)^2}$$

The right hand sides of Eq. (7) are defined respectively as

$$D_x=\frac{1}{2}\left(\frac{1}{2}C_y+d_y\right)\Omega_{i,j-1}^{n}+\left(1-d_y\right)\Omega_{i,j}^{n}+\frac{1}{2}\left(-\frac{1}{2}C_y+d_y\right)\Omega_{i,j+1}^{n} \quad (8\text{-a})$$

$$D_y=\frac{1}{2}\left(\frac{1}{2}C_x+d_x\right)\Omega_{i-1,j}^{n+½}+\left(1-d_x\right)\Omega_{i,j}^{n+½}+\frac{1}{2}\left(-\frac{1}{2}C_x+d_x\right)\Omega_{i+1,j}^{n+½} \quad (8\text{-b})$$

The values of u and v used in Eq. (7) could be used at time n or n+1/2. If the later time is taken, the stream function equation should be solved at time n+1/2, for which larger computation time will be utilized. Simplification of the above equations leads to

$$\begin{aligned} A_x\Omega_{i-1,j}^{n+\frac{1}{2}}+B_x\Omega_{i,j}^{n+\frac{1}{2}}+C_x\Omega_{i+1,j}^{n+\frac{1}{2}}&=D_x \\ A_y\Omega_{i,j-1}^{n+\frac{1}{2}}+B_y\Omega_{i,j}^{n+\frac{1}{2}}+C_y\Omega_{i,j+1}^{n+\frac{1}{2}}&=D_y \end{aligned} \quad (9)$$

in which

$$\begin{aligned} A_x&=-\frac{1}{2}\left(\frac{1}{2}C_x+d_x\right) \\ B_x&=1+d_x \\ C_x&=\frac{1}{2}\left(\frac{1}{2}C_x-d_x\right) \\ A_y&=-\frac{1}{2}\left(\frac{1}{2}C_y+d_y\right) \\ B_y&=1+d_y \\ C_y&=\frac{1}{2}\left(\frac{1}{2}C_y-d_y\right) \end{aligned} \quad (10)$$

2.2. Discretization of stream function equation

Regarding that the stream function Eq. (3) is of elliptic type, the Guass Seidal point to point method is employed for solving this equation as

$$\psi_{i,j}^{k+1}=\frac{1}{2(1+\beta^2)}\left[(\Delta x)^2\Omega_{i,j}^{k}+\psi_{i+1,j}^{k}+\psi_{i-1,j}^{k+1}+\beta^2\left(\psi_{i,j+1}^{k}+\psi_{i,j-1}^{k+1}\right)\right] \quad (11)$$

in which

$$\beta = \frac{\Delta x}{\Delta y} \tag{12}$$

Computation begins with solving the vorticity Eq. (6). Then, the vorticity in Eq. (11) is given a new value and the stream function equation is solved for ψ. This process is repeated until the final convergent solution is achieved. After ψ computation, the velocity components are computed using Eq. (4).

$$\begin{aligned} u_{i,j} &= \frac{\psi_{i,j+1} - \psi_{i,j-1}}{2\Delta y} \\ v_{i,j} &= -\frac{\psi_{i+1,j} - \psi_{i-1,j}}{2\Delta x} \end{aligned} \tag{13}$$

2.3. Discretization of poison equation

Computing the final flow field, in order to obtain pressure field, the poison Eq. (5) is discretized as follows;

$$\nabla^2 p = 2\left[\left(\frac{\partial^2 \psi}{\partial x^2}\right)\left(\frac{\partial^2 \psi}{\partial y^2}\right) - \left(\frac{\partial^2 \psi}{\partial x \partial y}\right)^2 \right] \tag{14}$$

This equation could be rewritten as

$$\nabla^2 P = S \tag{15}$$

In which

$$S = 2\left[\left(\frac{\partial^2 \psi}{\partial x^2}\right)\left(\frac{\partial^2 \psi}{\partial y^2}\right) - \left(\frac{\partial^2 \psi}{\partial x \partial y}\right)^2 \right] \tag{16}$$

Therefore, we would have

$$\begin{aligned} S_{i,j} = 2\Bigg[&\left(\frac{\psi_{i+1,j} - 2\psi_{i,j} + \psi_{i-1,j}}{(\Delta x)^2}\right) \times \left(\frac{\psi_{i,j+1} - 2\psi_{i,j} + \psi_{i,j-1}}{(\Delta y)^2}\right) \\ &- \left(\frac{\psi_{i+1,j+1} - \psi_{i+1,j-1} - \psi_{i-1,j+1} + \psi_{i-1,j-1}}{4\Delta x \Delta y}\right)^2 \Bigg] \end{aligned} \tag{17}$$

Now, having $S_{i,j}$ and using the point by point Guass-Seidal elimination to discretize Eq. (15), pressure at all points of the flow domain is computed by

$$p_{i,j}^{k+1} = \frac{1}{2(1+\beta^2)}\left[(\Delta x)^2 s_{i,j}^k + p_{i+1,j}^k + p_{i-1,j}^{k+1} + \beta^2\left(p_{i,j+1}^k + p_{i,j-1}^{k+1}\right)\right] \tag{18}$$

2.4. Initial conditions

With regard to Figure 1, the initial conditions are defined as

$$u = 0, v = 0, \quad at \quad t = 0 \qquad and \qquad 0 \le x \le 1, \quad 0 \le y \le 1 \tag{19}$$

2.5. Boundary conditions

The wall of the cavity is a stream line, and the stream function is constant on this surface and its value could be taken arbitrarily.

There is no explicit boundary condition for vorticity, so, boundary conditions should be constructed. The method for this purpose is the stream function equation and its Taylor series expansion. As a result, distinct formulations with different degrees of approximation are obtained. In this research, the first degree formulation is employed. With regard to Figure 1, the boundary conditions are defined as

$$\mathrm{i}=1:\ \{\mathrm{j}=1 \quad \text{to} \quad \mathrm{j}=\mathrm{JM} \quad \Rightarrow \begin{cases} \psi=0 \\ u=0 \\ v=-\psi_x=0 \\ \Omega=-\psi_{xx} \end{cases} \tag{20-a}$$

$$\mathrm{i}=\mathrm{IM}:\ \{\mathrm{j}=1 \quad \text{to} \quad \mathrm{j}=\mathrm{JM} \quad \Rightarrow \begin{cases} \psi=0 \\ u=0 \\ v=-\psi_x=0 \\ \Omega=-\psi_{xx} \end{cases} \tag{20-b}$$

$$\mathrm{j}=1:\ \{\mathrm{i}=1 \quad \text{to} \quad \mathrm{i}=\mathrm{IM} \quad \Rightarrow \begin{cases} \psi=0 \\ u=\psi_y=0 \\ v=0 \\ \Omega=-\psi_{yy} \end{cases} \tag{20-c}$$

$$\mathrm{j}=\mathrm{JM}:\ \{\mathrm{i}=1 \quad \text{to} \quad \mathrm{i}=\mathrm{IM} \quad \Rightarrow \begin{cases} \psi=0 \\ u=\psi_y=U \\ v=0 \\ \Omega=-\psi_{yy} \end{cases} \tag{20-d}$$

So, using certain mathematics for boundary conditions, the following relations are obtained for the boundaries.

$$\begin{aligned} \Omega_{1,j} &= \frac{2\left(\psi_{1,j}-\psi_{2,j}\right)}{(\Delta x)^2} \\ \Omega_{IM,j} &= \frac{2\left(\psi_{IM,j}-\psi_{IMM1,j}\right)}{(\Delta x)^2} \\ \Omega_{i,1} &= \frac{2\left(\psi_{i,1}-\psi_{i,2}\right)}{(\Delta y)^2} \\ \Omega_{i,JM} &= \frac{2\left(\psi_{i,JM}-\psi_{i,JMM1}\right)}{(\Delta y)^2}-\frac{2U}{\Delta y} \end{aligned} \tag{21}$$

Imposing the initial and boundary condition on the discretized Eqs. (9-13), these equations

are solved with the assumption that value of flow stream function on solid borders are zero. It should be mentioned that imposing boundary conditions of higher degrees leads to higher accuracy while causes instability in higher Reynolds numbers.

Eqs. (2) and (3) should be solved simultaneously. For this purpose, first the vorticity equation is solved, then, having the vorticity distribution, the poisson equation is solved for the stream function distribution. With stream function the boundary conditions of vorticity equation could be computed so that the vorticity equation could be solved for new solution at the next time-step. This process is repeated until the solution for the desired time is reached or the steady solution is achieved.

3. Results and Discussion

The fluid flow in a square cavity is the best problem to verify numerical results [4-7, 11]. Therefore flow field in a cavity was simulated. The velocity field at the top moving wall of the cavity shows a large recirculation region inside the cavity. With increasing moving wall velocity and the Reynolds number value, additional smaller recirculation zones appear in the corners of the cavity.

Figures 2 and 3 show the streamlines for Reynolds number 100 in two different computational grids of 31×31 and 11×11. As shown in Figures 4, 5 and 6, Computations are presented here for the Reynolds number 400 and 1000 in a 31×31 computational grid and for Reynolds number 2000 in a 51×51 computational grid. The 11×11 computational grid is not able to display the vortex at the edges of the cavity. In other words at Re=100 there is no formation of secondary circulation at the bottom of the cavity and has only primary circulation towards the upward direction of the cavity. There is a formation of small secondary circulation at Re=400 and large secondary circulation at Re=1000. So higher the lid velocity, faster is the formation of secondary circulation. However, convergence of the solution in such a complicated flow shows the power of the numerical solution scheme. It can be seen that the excitation U creates a vortex near the right upper corner of the fluid domain that spins clockwise and gradually gathers strength while moving into the direction of the domain's centre. This so-called primary vortex finally comes to a halt at a height of roughly y = 0.74. If we vary the parameters, it is seen that the appearance and position of the emerging vortices is strongly dependent on the Reynolds number. If we use, for example, Re=1000, the flow pattern is much more complex and the occurring vortices are much larger and stronger than in the situation above. At Re=1000, it is seen, that the large primary vortex causes the development of two smaller vortices along the right boundary of the fluid domain. These two vortices merge into each other after 6.5 units of time and create the actual secondary vortex in the bottom right corner. It should be noted that in the above situation the centre of the primary vortex moves much further than for Re=100 – up to a height of approximately y = 0.565. In general, it can be observed that the rotation speed and the magnitude of the vortices increase with the Reynolds number and that the final position of the main vortex approaches the geometric centre of the cavity as Re tends to infinity. As shown in Re=2000, for higher Re values the primary vortex shifts more to the centre and more corner secondary vortices are formed. The secondary vortices are also convected towards the centre of the domain for higher Re values. Also with the convection of secondary vortices more vortices are formed at the corners.

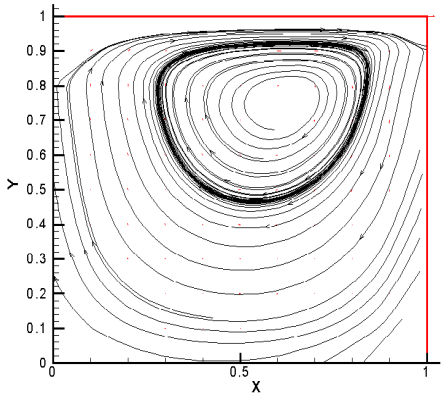


Figure 2. Streamlines plot of cavity flow for Mesh = 11×11 & Re = 100

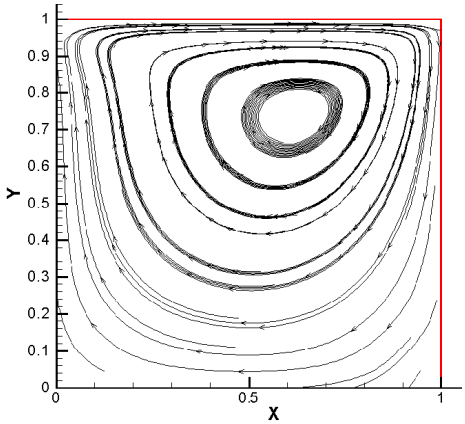


Figure 3. Streamlines plot of cavity flow for Mesh = 31×31 & Re = 100

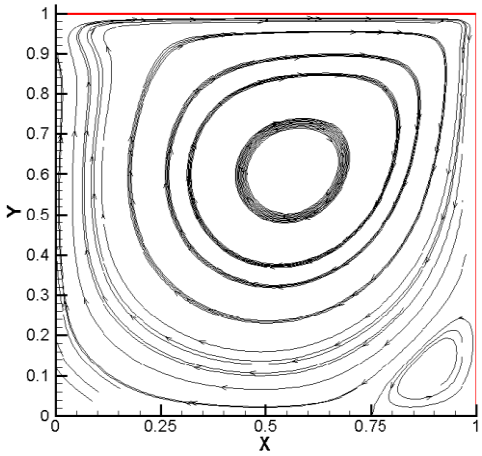


Figure 4. Streamlines plot of cavity flow for Mesh = 31×31 & Re = 400

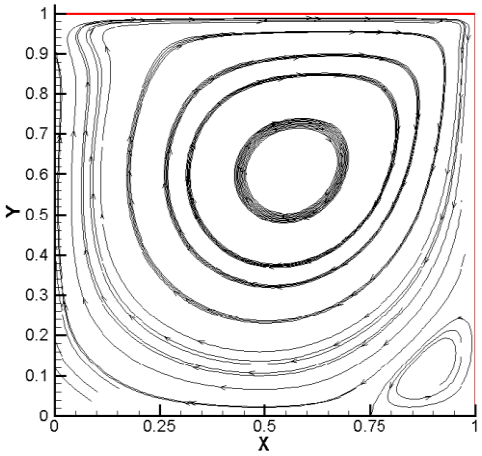


Figure 4. Streamlines plot of cavity flow for Mesh = 31×31 & Re = 400

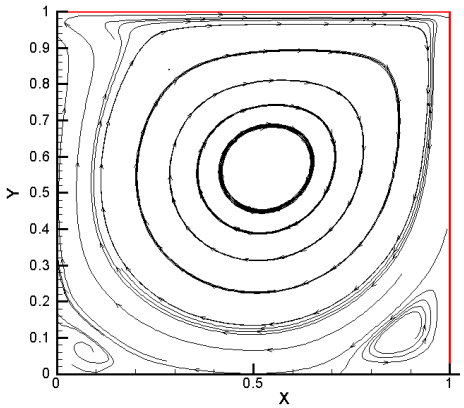


Figure 5. Streamlines plot of cavity flow for Mesh = 31×31 & Re = 1000

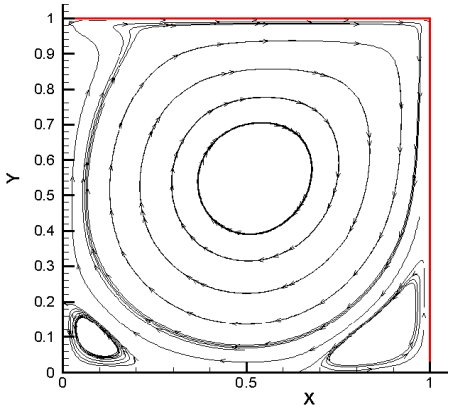


Figure 6. Streamlines plot of cavity flow for Mesh = 51×51 & Re = 2000

Figure 7 shows velocity field distribution in y direction and at x=L/2 (with L as the Length of the cavity). At the top boundary, the horizontal velocity component is equal to the velocity of the plate and on the solid boundary the velocity is zero. It is seen that the velocity component in x

direction on the top is equal to the input value and at the solid boundary is zero. The vertical component is trivial compared with horizontal one due to swirling nature of flow. In other words the velocity fluctuations in the vertical direction are significantly higher than those in the horizontal direction.

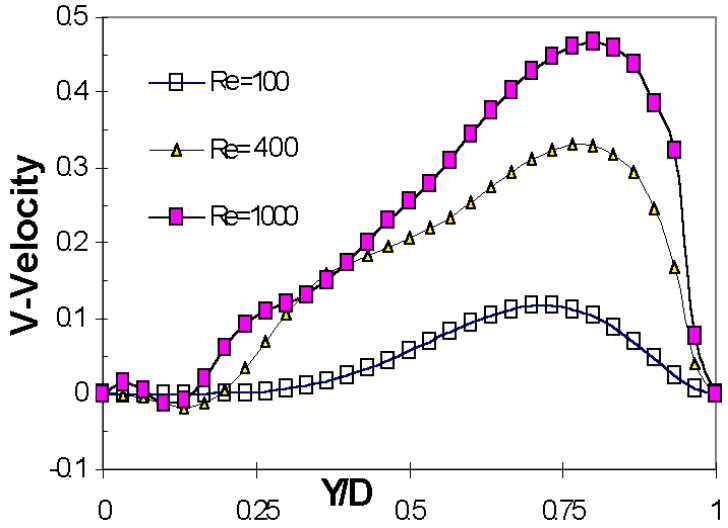


Figure 7. Vertical component of velocity distribution in x=1/2

Figure 8 shows velocity field distribution at the centre of the cavity in x direction at y=D/2 (with D as the height of the cavity). On the solid boundary, the values of the velocity components are zero and the results show the nature and behavior of the flow very well.

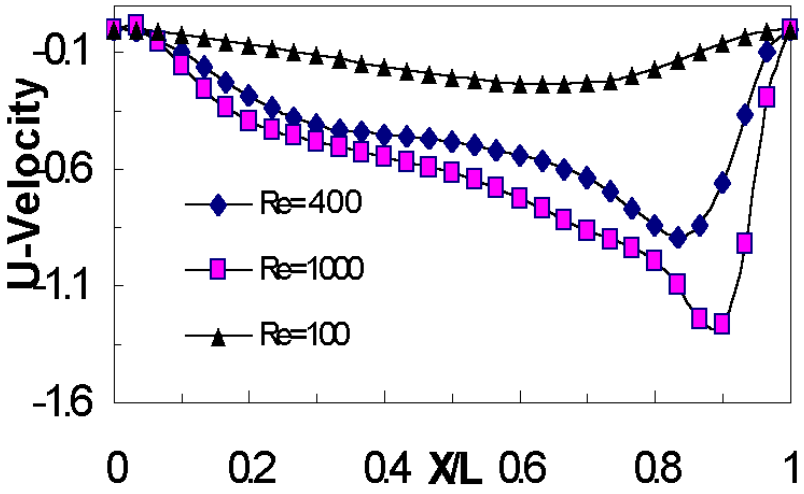


Figure 8. Horizontal component of velocity distribution in y=D/2

As shown in Figure 9, the results of this research were compared with Ghia (1982) and chen's (1991) results which show promising results.

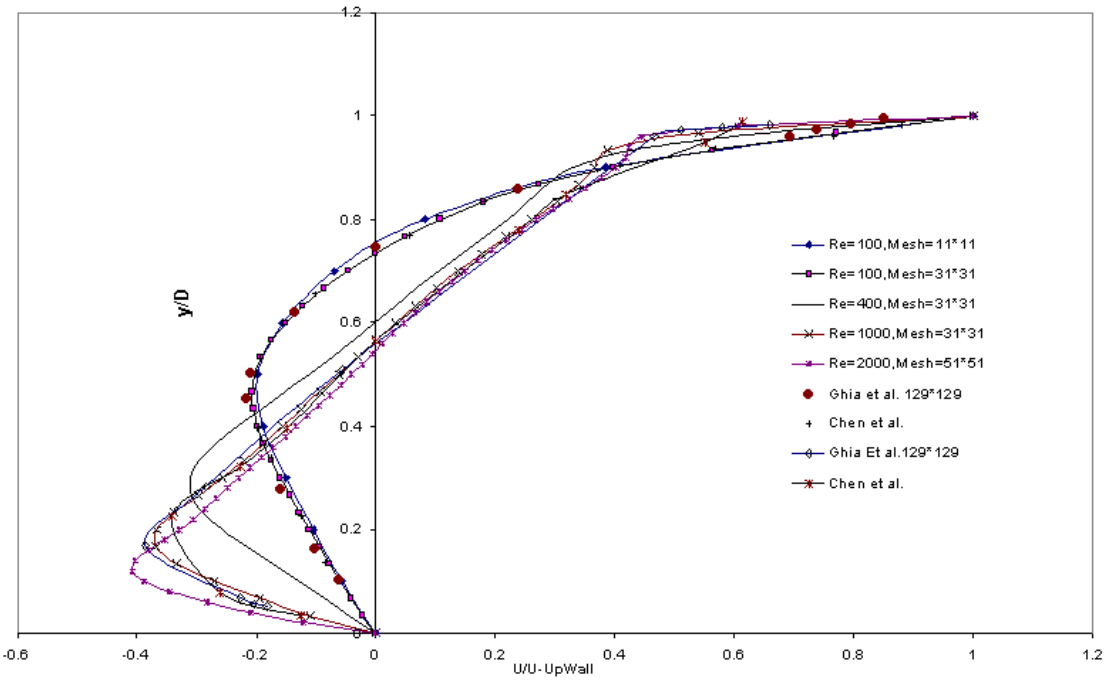


Figure 9. Comparison of vertical component of velocity distribution in x=L/2 with Ghia & Chen results

4. Conclusion

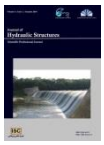
We have extended a vorticity-Stream function formulation for computation of unsteady incompressible fluid flow based on an alternating direction implicit. Therefore in this research, analysis of flow field in a cavity with different values of the Reynolds numbers 100, 400, 1000 and 2000 was carried out by solving the NSE using and Vorticity–Stream function formulation and the ADI algorithm. The solutions for wall cavity flow are stable and convergent. Moreover, we believe that more work need to be done in this subject. Therefore, we will try to solve this problem by using an ADI finite difference method. To this, special formulations with different degrees of approximation which satisfy the boundary conditions are obtained. Finally, comparing the results with the benchmarks show that alternating direction implicit is an effective and suitable formulation for the solution of NSE. Therefore the method is an efficient with promising results.

5. References

1. Ghia U, Ghia K N, Shin C T. (1982). High-Re solution for incompressible flow using the Navier-Stokes equations and a multigrid method. Journal of Computational Physics, 48(3), 387-411.
2. Chen KH, Pletcher RH, (1991), Primitive variable strongly implicit calculation procedure for viscous flows at all speeds. AIAA Journal, 29(8), 1241-1249.
3. Driesen C H, Kuerten J G M, Streng M. (1998). Low-Reynolds-number flow over partially covered cavities. Journal of Engineering Mathematics, 34(1-2), 3–21.
4. Koseff J R, Street R L. (1984). On end wall effects in a lid-driven cavity flow. Journal of Fluids Engineering, 106(4), 385–389.
5. Koseff J R, Street R L. (1984). The lid-driven cavity flow: A synthesis of qualitative and

quantitative observations. Journal of Fluids Engineering, 106(4), 390–398.
6. Prasad A K, Koseff J R. (1989). Reynolds number and end-wall effects on a lid-driven cavity flow. Physics of Fluids, 1(2), 208–218.
7. Aidun C K, Triantafillopoulos N G, Benson J D. (1991). Global stability of a lid-driven cavity with through flow: flow visualization studies. Physics of Fluids, 3(9), 2081–2091.
8. Gürcan F. (2003). Effect of the Reynolds number on streamline bifurcations in a double-lid-driven cavity with free surfaces. Computer & Fluids, 32(9), 1283–1298.
9. Erturk E, Gokcol O. (2007). Fine grid numerical solutions of triangular cavity flow. The European Physical Journal Applied Physics, 38(1), 97–105.
10. Agarwal R K. (1981). A third-order-accurate upwind scheme for Navier-Stokes solutions at high Reynolds numbers. AIAA Paper No. 81-0112, 15 p.
11. Anderson D, Tannehill J C, Pletcher R H. (1984). Computational fluid mechanics and heat transfer. Hemisphere Publishing Corporation, Taylor and Francis Publication, New York, 803 p.

Journal of Hydraulic Structures
***J. Hydraul. Struct.*, 2018; 4(1):19-35**
DOI: 10.22055/JHS.2018.25309.1070



OPEN ACCESS

Wave Evolution in Water Bodies using Turbulent MPS Simulation

Hanifeh Imanian[1]
Morteza Kolahdoozan[2]
Amir Reza Zarrati[3]

Abstract

Moving Particle Semi-implicit (MPS) which is a meshless and full Lagrangian method is employed to simulate nonlinear hydrodynamic behavior in a wide variety of engineering application including free surface water waves. In the present study, a numerical particle-based model is developed by the authors using MPS method to simulate different wave problems in the coastal waters. In this model fluid and solid are treated as separate phases and governing equations of momentum and continuity are solved for them concurrently. For simulations of turbulent wavy flows, constant eddy viscosity, Prandtl's mixing length theory and k-ε models were considered. In addition, higher order of MPS operators was applied to suppress numerical oscillation in comparison with previous studies. The developed method was applied to some cases, including still water reservoir, solitary wave propagation in a tank, tsunami run-up on an inclined wall and wave generation due to the landslide. Evaluation of the developed model results, in compare with data cited in the literature showed enhancement in the accuracy of the developed numerical model especially in compare with existing inviscid models. Besides, the numerical tests results have shown that applying k-ε turbulence model, have equipped MPS model with a useful, powerful and reliable tool for simulating water free surface in wave motion, wave impact and the breaking process.

Keywords: numerical modeling, Lagrangian approach, Moving Particle Semi-implicit (MPS) method, turbulence modeling, wave evolution

Received: 18 March 2018; Accepted: 25 May 2018

[1] Assistant professor, Department of Civil Engineering, Engineering Faculty, Alzahra University, Tehran, Iran, h.imanian@alzahra.ac.ir (**Corresponding author**)
[2] Associate professor, Department of Civil and Environmental Engineering, Amirkabir University of Technology, Tehran, Iran, mklhdzan@aut.ac.ir
[3] Professor, Department of Civil and Environmental Engineering, Amirkabir University of Technology, Tehran, Iran, zarrati@aut.ac.ir

CC BY

1. Introduction

Owing to commercial and economical role in coastal areas, studying waves have significant hydraulic importance especially in marine environments and estuaries. Hydrodynamic simulation of wave mechanics is however difficult due to complexity of their boundary conditions which are incorporated with an arbitrary moving surface. Despite the great advances in numerical modeling, it is still difficult to simulate free surfaces or solid- fluid interactions like wave impact to coastal structures.

Recently, Lagrangian approaches are applied in free surface modeling [1]. According to this approach, the study area is divided into a number of particles and the governing equations of flow are discretized and solved for each particle [2]. In particle-based methods no mesh generation is required and therefore free surface can be predicted by tracking fluid particle positions in each time step. This means no additional equation is necessary to be solved for free surface prediction. Since no mesh is necessary, the numerical dispersion errors, which are related to mesh generation, are eliminated.

The first ideas in this way were proposed by Monaghan in the area of astrophysical hydrodynamic problems with the method called Smooth Particle Hydrodynamics (SPH) [2]. This method was later generalized to fluid mechanic problems. One of the latest particle based methods is Moving Particle Semi-implicit (MPS) which was originally introduced by Koshizuka and Oka [3].

MPS method is applied for modeling a number of hydraulic phenomena such as dam break (Koshizuka et al.), breaking waves (Koshizuka et al.; Gotoh and Sakai and Gotoh et al.), jet breakup (Shibata et al.) and flow over spillways (Shakibaeinia and Jin) [4, 5]. Moreover, Gotoh et al. and Gotoh and Sakai developed a multi- phase MPS model for simulating gas- liquid and solid- liquid problems, sediment transport and floating bodies [1]. Ataie-Ashtiani and Farhadi compared different kernel functions and introduced a formulation for increasing the stability of the MPS model [6]. Zhang et al. proposed a new Laplacian model and used MPS method in simulating heat transfer problems [7]. Shibata and Koshizuka applied a 3D model to simulate behavior of rushing water into the ships and predicted the impact pressure on the deck [8]. Fayyaz added several variables such as surface tension to the multi- phase MPS model to improve its stability and accuracy [9]. Kondo et al. introducing an artificial pressure, suppressed pressure oscillation which is usually observed in MPS modeling [10].

Khayyer and Gotoh worked on conservation of momentum and introduced new formula for calculating pressure gradient and allowed a slight compressibility to suppress its fluctuations [5]. Later on, Khayyer and Gotoh proposed a higher order Laplacian formulation for stabilization and enhancement of pressure calculation [11]. Shakibaeinia and Jin replaced incompressibility in the original MPS model with a weakly incompressible model, by particle recycling strategy for boundary condition [12]. Tanaka and Masunaga tried to obtain a smooth pressure variation both in time and space and eliminate its oscillation [13]. Slamming problems such as liquid- liquid and solid- liquid collision were simulated by Lee et al. using MPS method [14]. To suppress the unphysical pressure oscillation, Kondo and Koshizuka proposed a new formulation for the source term of Poisson equation of pressure [15].

In practice, there are a large number of engineering problems belong to turbulent flow, and it is necessary to extend the original MPS method to the turbulent flow simulation. From the turbulent point of view, an incompressible SPH theory was combined with Large Eddy Simulation (LES) model by Gotoh et al, to investigate wave interaction with partially immersed breakwater [16]. Shao and Gotoh used a 2D Sub-Particle Scale (SPS) turbulence model based on

eddy viscosity assumption to simulate wave breaking on the beach by SPH method [17]. Two-equation k-ε turbulence model was chosen by Shao to couple with SPH scheme for simulating wave breaking on a slope [18]. To investigate the properties of the plunging waves, Shao and Ji combined numerical method of SPH with LES and used Smagorinsky model to simulate turbulence stresses [19]. Violeau and Issa reviewed turbulent models adapted to the SPH method from simplest model of mixing length to more sophisticated ones such as EARMS or LES [20].

In contrast with SPH, MPS method is usually used for modeling inviscid free surface flows and attempts to apply turbulence effects in these models has been very limited [21, 22, 23]. In the governing equations of Large Eddy Simulation, only Reynolds stress is a new term. So compared with the RANS, the governing equations of LES is easier to handle in MPS method. Gotoh et al. 2001 demonstrate advantage of simulation of free surface flow by LES simulation in MPS [24]. Fayyaz and Kolahdoozan tried to add the viscous effects of flow by means of constant eddy viscosity to their multi-phase MPS model [25]. Shirazpoor developed their multi-phase MPS method using Prandtl's mixing length theory and k-ε model in dam break problem [26, 27]. Pan et al. introduced an area-time average method to reduce the pressure fluctuation in MPS in their MPS-LES model and applied it to a 2D sloshing simulation [28]. Mosaffa and Tang et al. defined a refinement algorithm based on the particle splitting and increased the resolution of the whole simulation region in MPS multi-resolution model [29, 30]. Ikari et al. developed an erosion sub-model in their MPS model for analysis of large deformations of soil, due to wave induced erosion in sea cliffs. The model was further enhanced by utilizing sub-particle-scale suspended sediment load sub-model together with advection-diffusion equation by [31]. Harada et al. developed a DEM-MPS coupled method for reproduction of swash beach sediment transport processes in a gravel beach and investigated the formation/deformation processes of step series on the riverbeds in mountain [32, 33]. Gotoh and Khayyer provided an up-to-date comprehensive review on latest advancements related to particle methods with applications in coastal and ocean engineering [34]. They also highlighted future perspectives for further enhancement of applicability and reliability of particle methods for coastal and ocean engineering.

In this study, a particle-based numerical model is presented using MPS method to simulate different wave problems. The authors have developed their own code to simulate viscous fluid flow in the coastal waters. They have applied governing equations on fluid particles rather than mesh and solved them by MPS method to predict hydrodynamic parameters of solution domain. The effect of turbulence is calculated using three turbulence closures including constant eddy viscosity; Prandtl's mixing length and k-ε. Herein, results obtained for a number of wave problems from different turbulence closures combined with the developed MPS model are compared with experimental data or analytical solutions cited in the literature. It was found that considering turbulence effects improves the stability, accuracy and capability of the MPS model.

2. Governing Equations

Governing equations of viscous fluid flow include continuity and momentum equations can be represented as follows:

$$1/\rho \, D\rho/Dt + \nabla \mathbf{u} = 0 \quad (1)$$

$$D\mathbf{u}/Dt = -1/\rho \, \nabla p + \nu_t \nabla^2 \mathbf{u} + g \quad (2)$$

where $\boldsymbol{u}$= velocity vector, t= time, ρ= fluid density, P= pressure, ν_t= fluid eddy-viscosity and g= gravitational acceleration.

The pressure term in the momentum equations can be considered as an independent variable

which contains both the static and dynamic parts. Thus, by solving Poisson equation, the pressure term can be calculated for all particles. Poisson equation rewrites as follows [3]:

$$\nabla^2 P = {}^{\Delta\rho}/_{\Delta t^2} \tag{3}$$

In the MPS method, free surface is predicted automatically when all particles position were specified.

2.1. Model Discretization

In the MPS method the equations of continuity and momentum are converted to interaction equations of particles using different operators. All interactions between particles are limited to a specific distance known as efficient radius. The weighting of different neighboring particles within the efficient radius on the desired particle is calculated based on Kernel functions. In the present study following basic interaction model is used as the Kernel function [5]:

$$w(r) = \begin{cases} {}^{r_e}/_{r} - 1 & 0 < {}^{r}/_{r_e} \le 1 \\ 0 & 1 < {}^{r}/_{r_e} \end{cases} \tag{4}$$

where r= distance between two particles i and j, r_e= efficient radius and w= Kernel function.

This function is effective for saving computational time and memory and is efficient for avoiding clustering of particles and improves numerical stability [17].

The particle number density, actually a weighted average, can be defined in the following form by using the kernel function [3]:

$$\langle n \rangle_i = \sum_{j \neq i} w(|r_j - r_i|) \tag{5}$$

where n_i is the density of particle i in location r_i.

Since the fluid density is proportional to the particle number density [3], the continuity equation is satisfied if the particle number density is constant in incompressible fluids [6]. This constant value is denoted by n^0 and is called standard density. For n^0 we use particle number density in the initial state.

A gradient vector is evaluated between two neighboring particles. The gradient operator is modeled using the weight function and conserve linear and angular momentum. It can be expressed as [5]:

$$\langle \nabla \phi \rangle_i = {}^{d}/_{n^0} \sum_{j \neq i} \left[(\phi_i + \phi_j) - 2\hat{\phi}_i \Big/ |r_j - r_i|^2 (r_j - r_i) w(|r_j - r_i|) \right] \tag{6}$$

where ϕ= a physical quantity, d= number of dimension (for two dimensions is replaced with 2), r_i = location vector for particle i, and ϕ' = minimum amount of ϕ belonging to the neighboring particles in the efficient radius:

$$\phi_i' = \min(\phi_j) \quad \text{for} \quad \{w(|r_j - r_i|) \neq 0\} \tag{7}$$

The presented Laplacian model has a conservative form and can be written as [3]:

$$\langle \nabla^2 \phi \rangle_i = {}^{2d}/_{n^0 \lambda} \sum_{j \neq i} [(\phi_j - \phi_i) w(|r_j - r_i|)] \tag{8}$$

In the above equations, λ is a coefficient defined as:

$$\lambda = \int w(r) r^2 dv \Big/ \int w(r) dv \tag{9}$$

2.2. Turbulence Closures

Since the flow in this study is viscous and turbulent, Prandtl's mixing length theory and k-ε models are used in addition to constant eddy viscosity to consider shear stresses in the flow

domain.

According to Prandtl's mixing length model [35,36] which is widely used in estuaries and coastal waters [37] eddy viscosity ν_t can be written as:

$$\nu_{t,i} = \kappa u_{*i} z_i \left(1 - {}^{z_i}/_{H}\right) \quad (10)$$

where, $\nu_{t,i}$= turbulent eddy viscosity for particle i, κ= von Karman's constant, u_{*_i}= shear velocity for particle i, z_i= vertical distance of particle i from the bed and H= total water depth.

According to k-ε turbulent model [38] eddy viscosity ν_t can be written as:

$$\nu_{t,i} = C_\mu \, {}^{k_i^2}/_{\varepsilon_i} \quad (11)$$

where k_i= turbulence kinetic energy for particle i, ε_i= energy dissipation rate for particle i and C_μ is a constant= 0.09.

Lagrangian form of convection equation for turbulence kinetic energy, k can be written as [20, 38]:

$${}^{Dk}/_{Dt} = P_k - \varepsilon + \nabla\left[\left(\nu + {}^{\nu_t}/_{\sigma_k}\right)\nabla k\right] \quad (12)$$

where σ_k is a constant =1.0.

This equation is analogous to the convection-diffusion equation where the production rate of kinetic energy P_k is similar to the source term, while energy dissipation ε is similar to the sink term P. In the MPS method the convection equation for k reads as:

$${}^{\Delta k}/_{\Delta t} = P_{k_i} - \varepsilon_i + {}^{2d\nu_{k,i}}/_{n^0\lambda} \sum_{j\neq i}\left[\left(k_j - k_i\right) w\left(|r_j - r_i|\right)\right] \quad (13)$$

where:

$$\nu_{k,i} = \nu + {}^{\nu_{t,i}}/_{\sigma_k} \quad (14)$$

in vector form, the source term P is [20]:

$$P = \nu_t S^2 \quad (15)$$

However, for preventing any overestimation of k in cases with high rates of strain, the non-isotropic turbulence should be limited. Therefore, a linear strain variation rate is considered for high deformations and the source term of particle i is limited as follows [20]:

$$P_{k_i} = \min\left(\sqrt{C_\mu}, C_\mu S_i \, {}^{k_i}/_{\varepsilon_i}\right) k_i S_i \quad (16)$$

For calculating the scalar mean rate of strain S one can write [18]:

$$S = \left[2\left({}^{\partial u}/_{\partial x}\right)^2 + 2\left({}^{\partial v}/_{\partial y}\right)^2 + \left({}^{\partial u}/_{\partial y} + {}^{\partial v}/_{\partial x}\right)^2\right]^{1/2} \quad (17)$$

The energy dissipation rate ε can be written as [18, 38]:

$${}^{D\varepsilon}/_{Dt} = \nabla\left[\left(\nu + {}^{\nu_t}/_{\sigma_\varepsilon}\right)\nabla\varepsilon\right] + {}^{\varepsilon}/_{k}\left(C_{\varepsilon,1}P_k - C_{\varepsilon,2}\varepsilon\right) \quad (18)$$

where σ_ε, $C_{\varepsilon,1}$ and $C_{\varepsilon,2}$ are empirical constants= 1.3, 1.44 and 1.92 respectively.

The MPS form of Equation (18) is as follows:

$${}^{\Delta\varepsilon}/_{\Delta t} = {}^{2d\nu_{\varepsilon,i}}/_{n^0\lambda} \sum_{j\neq i}\left[\left(\varepsilon_j - \varepsilon_i\right) w\left(|r_j - r_i|\right)\right] + {}^{\varepsilon_i}/_{k_i}\left(C_{\varepsilon,1}P_{k_i} - C_{\varepsilon,2}\varepsilon_i\right) \quad (19)$$

where:

$$\nu_{\varepsilon,i} = \nu + {}^{\nu_{t,i}}/_{\sigma_\varepsilon} \quad (20)$$

In the current study, a two-dimensional vertical model was developed considering the turbulence effect of the flow in the formulation, though the proposed method can be extended to three dimensions.

3. Solution Procedure

The governing equations of flow were solved semi-implicitly. To speed up the convergence the Projection method was deployed in which discretization of Navier-Stokes equations were completed in two half time steps. In the first half time step (prediction step) governing equations were solved in the presence of viscosity and gravity terms without enforcing incompressibility, while the pressure were disregarded. In the second half time step (correction step), the results obtained in the previous time step were modified in the presence of pressure gradient. In other words, the pressure term was used to update the particles velocity calculated from the prediction step [15, 17]. In mathematical expression, the Navier-Stokes equations for the first half time step can be written as:

$$\mathrm{D}\mathbf{u}/_{\mathrm{Dt}} = \nu_t \nabla^2 \mathbf{u} + g \tag{21}$$

To solve this equation, primarily, eddy viscosity should be computed.

In Prandtl's mixing length model, the eddy viscosity was computed based on velocity and position of particles according to Equation (10).

In k-ε model, in each time step, the solution algorithm followed Equation (11) to (20).

After solving Equation (21) explicitly, velocity components variations ($\Delta\mathbf{u}$) of all particles were obtained. Then, modified velocity and positions were calculated for each particle as follows:

$$\mathbf{u}^{t+1/2} = \Delta\mathbf{u}^{t+1/2} + \mathbf{u}^{t} \tag{22}$$

$$r^{t+1/2} = \mathbf{u}^{t+1/2}\Delta t + r^{t} \tag{23}$$

where $\boldsymbol{u}^t$, r^t, $\boldsymbol{u}^{t+1/2}$, $r^{t+1/2}$ = current and intermediate particle velocity and position, respectively.

In the prediction step, mass conservation is not satisfied. It means the particle number density $n_i^{t+1/2}$ that are calculated at the end of first half time step deviates from the constant n^0. Therefore, a second corrective process is required to adjust the particle number densities to initial constant values prior to the time step. In the second half time step, the intermediate particle velocity $\boldsymbol{u}^{t+1/2}$ is updated implicitly through solving the Poisson pressure Equation.

To calculate particles pressure, Poisson pressure Equation was then solved with the following discretized representation [11]:

$$\langle \nabla^2 P_i^{t+1} \rangle = \rho/_{\Delta t^2} \, n_i^{t+1/2} - n^0/_{n^0} \tag{24}$$

where Δt= calculation time step and t denoted the step of calculation.

Since explicit calculation of Poisson pressure equation leads to model instability, it is recommended to solve it in full implicit form as a linear equations system. One of solving methods for this linear system is Cholesky solution [39].

Finally, given the amount of particles velocity components and position at time t+1/2 and pressure value, the second time step of Projection method was enforced. In this stage, pressure was included in the momentum equations in the following form:

$$\rho\, \mathrm{D}\mathbf{u}/_{\mathrm{Dt}} = -\nabla p \tag{25}$$

This equation was solved implicitly and new velocity components and particle positions in the next time step were calculated as follows:

$$\mathbf{u}^{t+1} = \Delta\mathbf{u} + \mathbf{u}^{t+1/2} \tag{26}$$

$$r^{t+1} = \mathbf{u}^{t+1}\Delta t + r^{t+1/2} \tag{27}$$

The solution algorithm is illustrated in Figure 1.

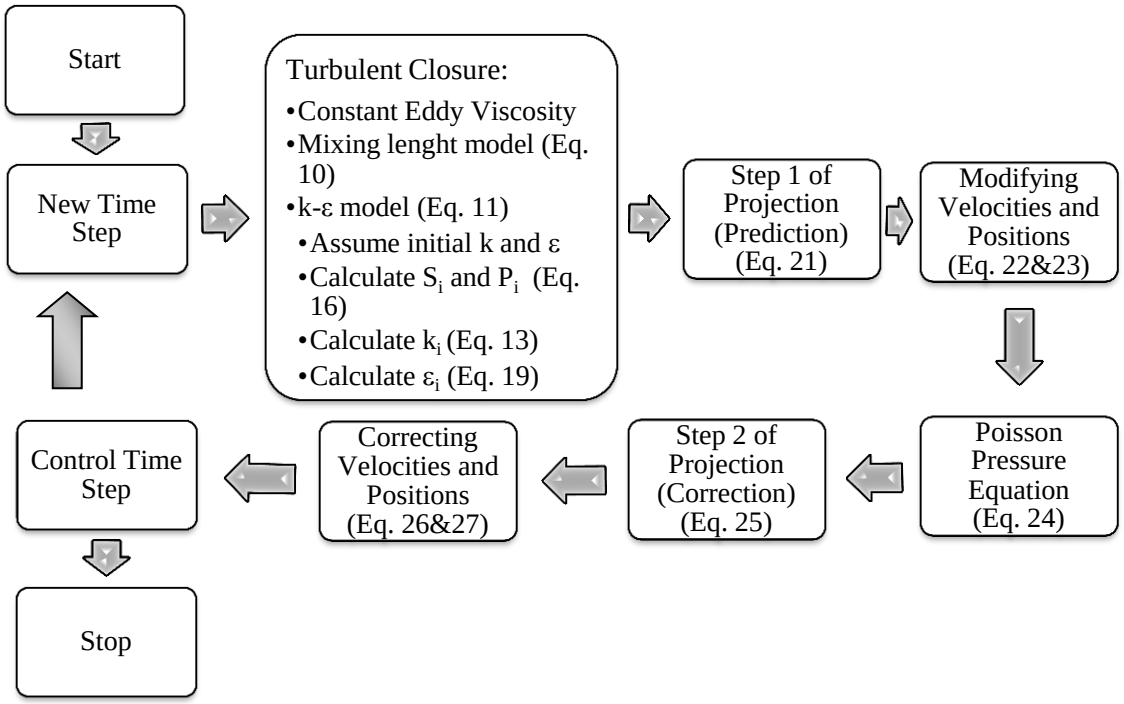


Figure 1. Solution algorithm of the present MPS model

4. Boundary Conditions

4.1. Free Surface

Free surface was defined as the location at which particles density is less than a certain value. Following condition is defined for free surface particle recognition [39]:

$$n_i < \beta n^0 \quad (28)$$

where β = threshold coefficient which is define 0.97 [1, 6, 9].

The standard or zero pressure value would be assigned in each time step to particles in this location and no additional computations were necessary.

4.2. Bed Boundary

Along solid boundary, particles position in the impermeable channel bed and walls were invariable and liquid particles were not able to penetrate into this solid layer. In all time steps, the governing equations were solved for near solid boundary particles to repulse the inner fluid particles accumulating in the vicinity of wall.

To model the no-slip condition in the vicinity of solid boundary, each particle near the boundary was checked for not to penetrate inside the solid boundary [9, 17].

5. Results and Discussion

5.1. Still Water reservoir

A 0.2 m-long reservoir containing still water with 0.2 m depth was modeled by 2601

particles. Time step is equal to 0.003 s.

In Figure 2 pressure history for a point in the middle of reservoir on the bed is represented. The Standard MPS method suffers from some spurious pressure fluctuation. A comparison between pressures calculated by present model using up-to-date formulation for the pressure gradient [5, 11] and standard MPS models shows improvements in pressure calculation and reduction of pressure fluctuations, particularly near the solid boundaries.

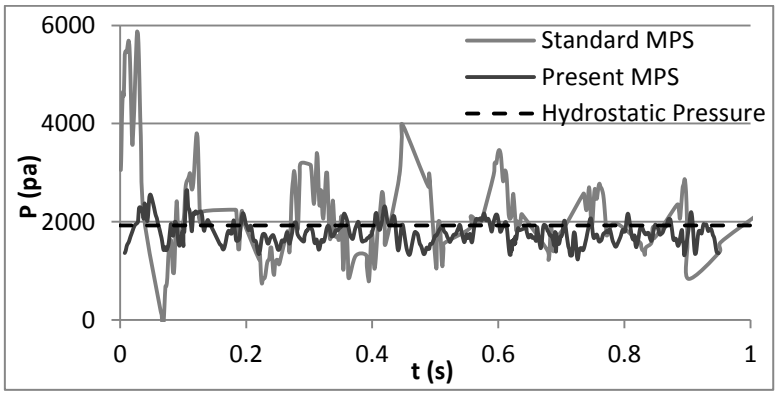


Figure 2. Computed pressure history on the bed (x= 0.1 m)

To represent the stability of computed pressure values, the pressure field in the middle of reservoir obtained from developed MPS model using no turbulence closures, is compared with hydrostatic values in Figure 3. It can be seen that pressure values are predicted near to hydrostatic line. It can be concluded that the numerical model is stable and predict pressure domain without fluctuation.

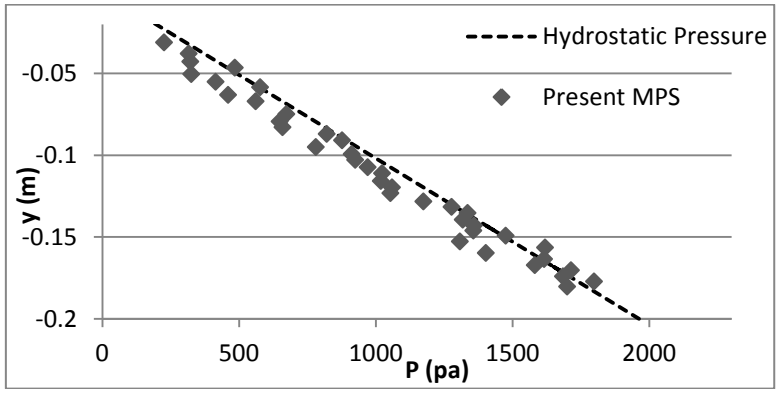


Figure 3. Comparison of computed pressure by present MPS model with hydrostatic values (x=0.1 m, t=0.2 s)

5.2. Solitary wave motion in a tank

Despite predominance of applying advanced pressure gradient formulation within static of fluid has been proven in the previous example; to evaluate the performance of the these new operators in the field of waves dynamic and their effects on the improvement of numerical calculations, they are applied in another test case.

In this test, wave motion in a tank with vertical walls was studied. The Wave tank was 3 m long with 0.5 m water depth. Solitary waves with different heights of 0.15 to 0.3 m were

generated at the left side of the tank and were propagated to the right. After collision of waves to the upright wall, run-up occurred.

Waves were generated similar to Monaghan and Kos experiments with the following equation [40]:

$$\eta = {H}\Big/{\mathrm{Cosh}^2\left(x\sqrt{\frac{3H}{4h^3}}\right)} \quad (29)$$

where η = free surface elevation, H= wave height, h= water depth and x= distance parallel to wave motion.

The wave profile equation was considered as the initial condition. According to solitary wave theory the vertical velocity is zero. The horizontal velocity profile U was introduced as follows [40]:

$$U = {\eta}/{h}\sqrt{gh} \quad (30)$$

In order to select basic variables such as time step and particle distance, the Courant number criterion was applied which can be written as:

$$Cr = {\Delta t\, V_{max}}/{r_0} \quad (31)$$

where r_0= initial distance between particles, Δt= time step, V_{max}= maximum flow velocity and $0 < Cr \leq 1$ is the Courant number. Shakibaeinia and Jin used $Cr = 0.25$, Ataie-Ashtiani and Farhadi employed $Cr = 0.2$, while Fayyaz and Kolahdoozan and Shobeyri and Afshar set $Cr = 0.1$ to have a stable solution [6, 12, 25, 41]. Factor 0.1 ensures that the particle moves only a fraction of the particle spacing in a time step.

Using Courant number maximum acceptable time step is gained according to particle size. To keep calculation stability an appropriate time step should be chosen. In this test case, particle diameter is equal to 0.035 m; the flow domain was modeled with 1600 particles in average and time step of 0.003 s, which satisfy considered Courant number.

In this test, turbulent models were not included in the model and the fluid was considered non-viscous. In Figure 4 non-dimensional values of run-up calculated by the MPS model were compared with experimental data of Camfield and Street, the results of MAC model of Chan and Street and SPH model of Monaghan and Kos [40].

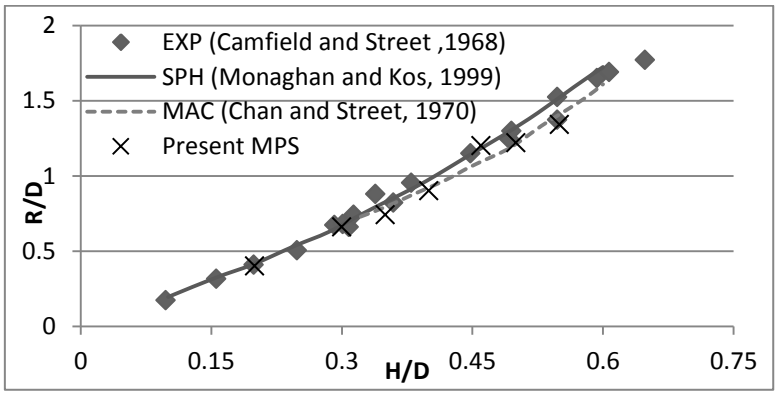


Figure 4. Comparison of present MPS model results with experimental data, MAC model and SPH model

Maximum computational errors were 4.5% and 4.1% for SPH and the present MPS methods respectively. In addition, MAC model has 4.3% error in comparison with laboratory results. It can be seen that the results of the developed model are closer to the experimental data in

comparison with the previous models.

From Figure 4 according to the present MPS model results, the following relationship is suggested to express the variation of wave run-up with water depth and wave height:

$$R/h = 2.862(H/h)^{1.230} \quad (32)$$

where *R*= wave run-up.

Water surface level and pressure predicted by the developed model for H/h equals to 0.4 are shown in Figure 5. Pressure field is presented in three time steps: A) before wave collision to the right wall, when a high pressure zone is formed at the end of the channel due to wave impact effect, B) highest run-up time when pressure field is decreased due to steady condition at maximum run-up and C) after collision when backwash happens and wave moves in the channel in a reverse direction.

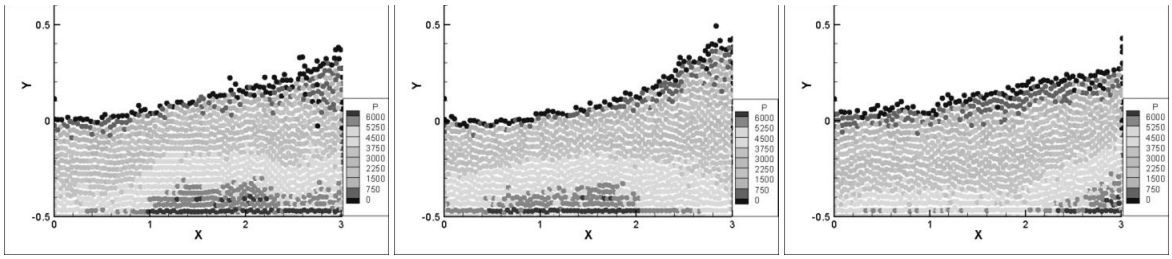


Figure 5. Computed water surface and pressure field (H/h=0.4)

Moreover, predicted velocity domain in two time step, before and after run-up, are displayed in Figure 6.

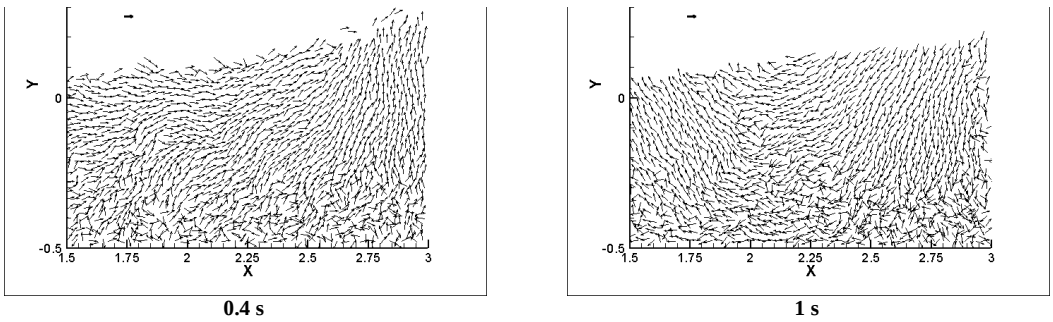


Figure 6. Computed velocity field (H/h=0.4)

It should be noted that except near the bed, velocity vectors are parallel to each other that shows rising wave front to the vertical wall before run-up and descending wave forehead after run-up.

5.3. Tsunami run-up on a slope

In this test the tsunami motion toward a slope was investigated. Initial wave profile was generated by Equation (29). Vertical velocity was assumed equals to zero and horizontal velocity was calculated from Equation (30).

In this case a 3 m long channel was considered. The slope angle of the beach was assumed 45^{o} and a wave height of 0.2 m was considered for modeling purposes. Water depth 'h' varied in

the range of 0.5 to 1 m. Wave was generated at the left side of the channel, propagated to the right and ran-up on the inclined beach (Figure 7).

Particle diameter is equal to 0.033 m; the flow domain was modeled with 2500 particles in average and time step of 0.003 s.

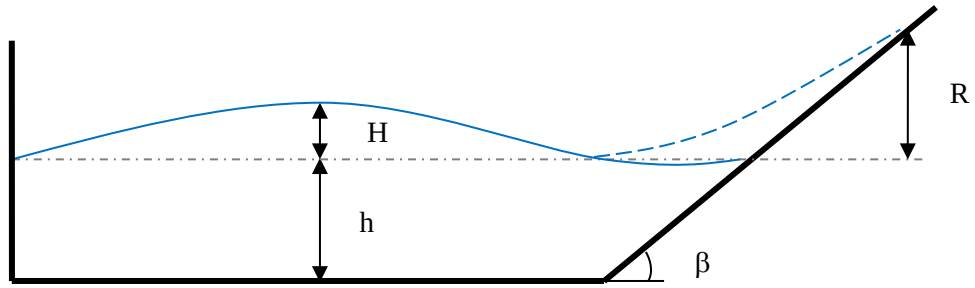


Figure 7. Tsunami run-up on a slope

Wave run-up on a slope can be estimated from empirical equations given in the literature. One of the recent relationships for long wave run-up on an impermeable smooth slope is presented by Muller, which considers wavelength as [42]:

$$R/h = 1.25\left(\pi/2\beta\right)^{0.2}\left(H/h\right)^{1.25}\left(H/L\right)^{-0.15} \quad (33)$$

where *L*= wavelength.

In theory solitary wave is infinitely long and it is not worth from engineering viewpoint. For practical purposes, its wavelength can be defined where 95% of area under wave profile is contained within this distance [43]:

$$L = 2.12h\sqrt{h/H} \quad (34)$$

In Figure 8 the calculated run-up by the developed model are compared with Equation (33). It can be seen that results of the k-ε model are closer to the results of the empirical equation.

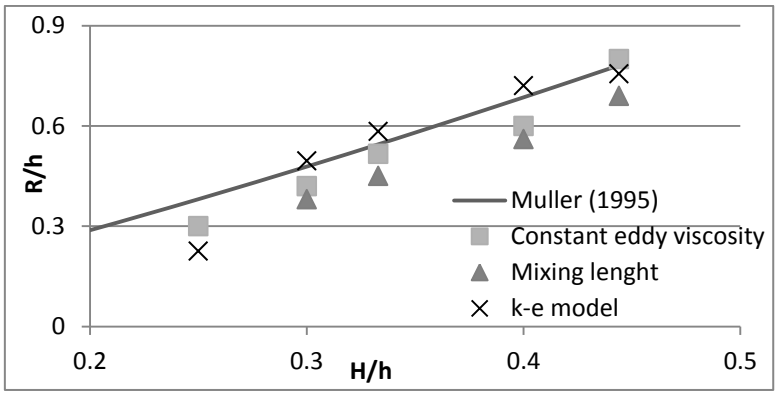


Figure 8. Comparison of present MPS model results with empirical relationships

Furthermore, run-up error analysis is carried out for various turbulence models. In constant eddy viscosity error is 5.5%, while in mixing length and k-ε model this value is 10% and 3%, respectively. This shows the superiority of the k-ε model.

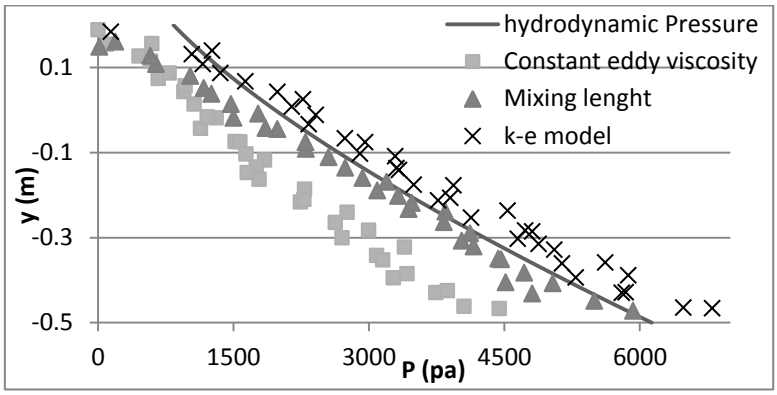


Figure 9. Comparison of computed pressure (H/h=0.4, x=3 m, t=0.5 s) by different turbulence closures with analytical pressure

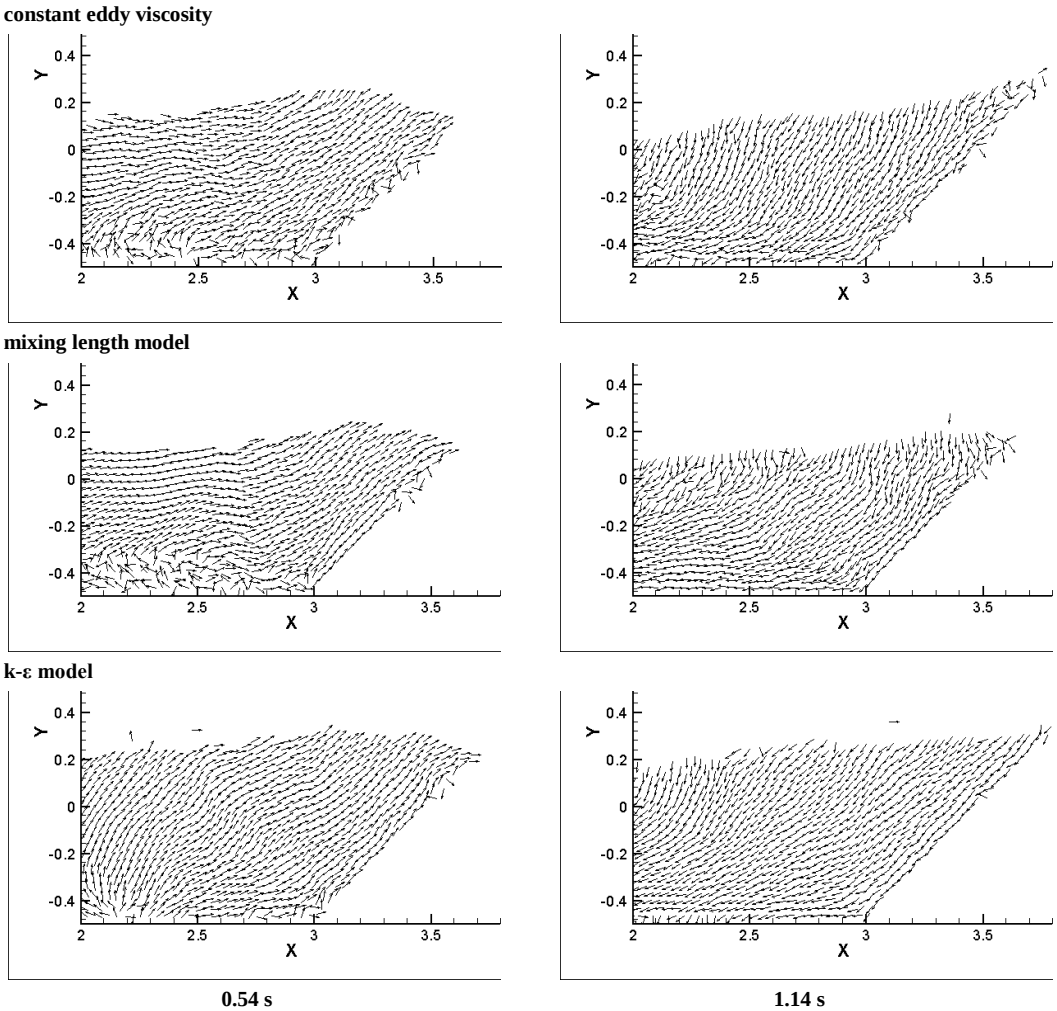


Figure 10. Computed velocity field (H/h=0.4)

In Figure 9, computed pressure field in the toe of the slope on the channel invert at time 0.5 s (before complete wave run-up on the slope) is compared with analytical values of water waves as [43]:

$$P = \rho g(\eta K_p - z) \quad (35)$$

where $P =$ pressure and $K_p =$ dynamic pressure coefficient.

From Figure 9 it can be concluded that constant eddy viscosity model underestimated pressure values in average by 45%, while mixing length model estimated it by 21%. k-ε model prediction has 4% mean-error which shows a better agreement with the analytical results. Computed velocity field using various turbulent models before and after run-up, are demonstrated in Figure 10.

Parallel velocity vectors show the progressive wave fronts toward the inclined wall before run-up. After run up however velocity vectors show properly the returning wave. Among turbulent models, k-ε velocity predictions are smoother and without fluctuations. This is more evident in the vicinity of the solid boundaries of bed and wall.

5.4. Landslide-generated water wave

To simulate landslide-generated waves, a rigid wedge, triangular in cross section (0.5×0.5 m) sliding into water along an inclined plane of 45° was considered [44,45]. Water depth was assumed 0.4 m and the bottom of the wedge was initially just above the initial free water surface (Figure 11).

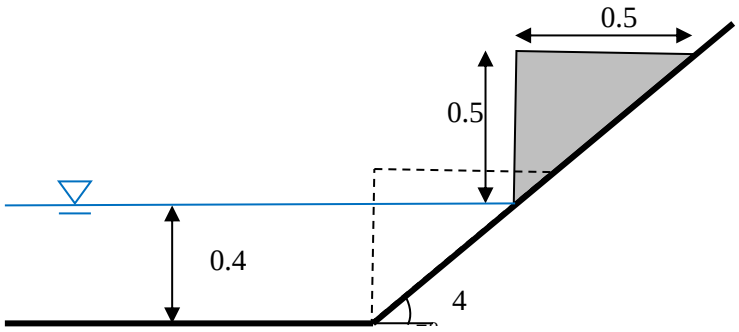


Figure 11. Rigid wedge sliding on the slope into water

Motion of the wedge in time was determined based on the following equation:

$$\text{vertical displacement} = 0.87 * t^2 + 0.2321 * t - 0.0048 \quad (36)$$

To model this case a channel with 0.4 m height and 6 m length was considered. The total numbers of 2444 particles was considered in the computational domain. Time step was selected equal to 0.003 second and initial wave profile was produced by Equation (29). Vertical velocity was assumed equals to zero and horizontal velocity was calculated from Equation (30).

Generated wave and water level variation at various times and for different turbulence models are compared with experimental measurements of Heinrich in Figure 12. From this comparison it can be seen that predicted water surface elevations by k-ε turbulence model are more accurate.

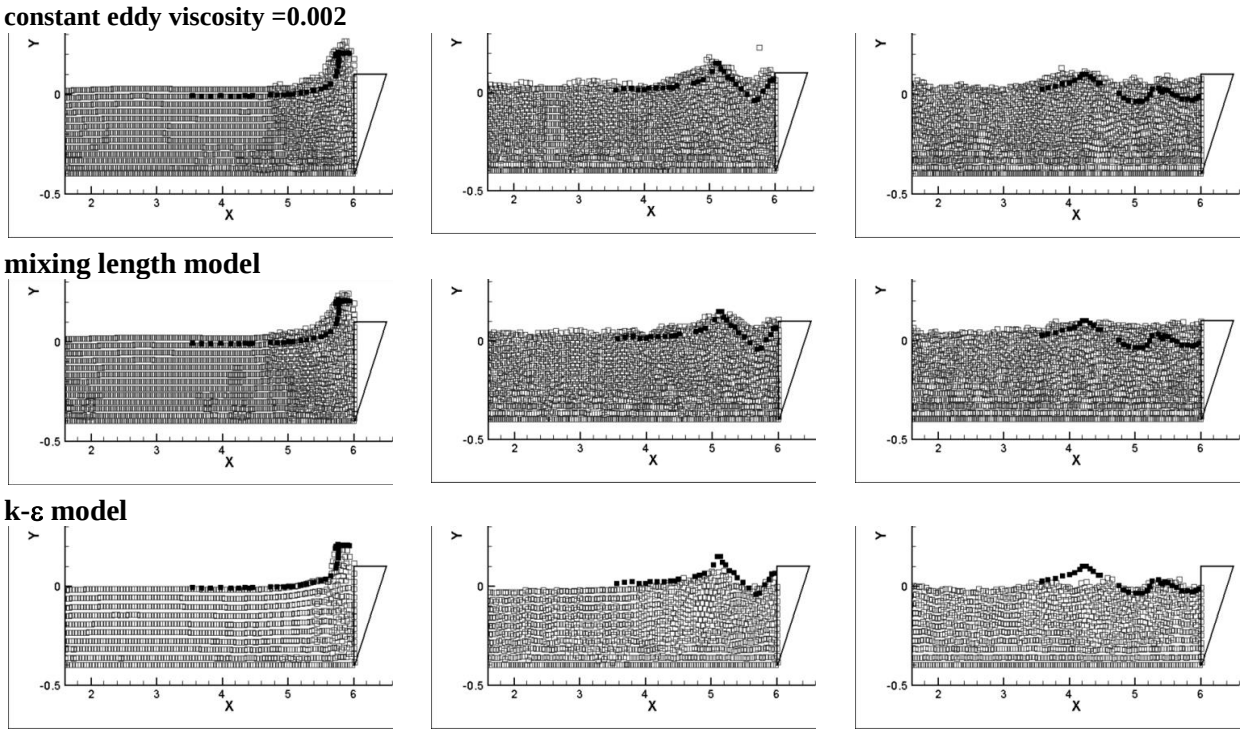


Figure 12. Comparison of computed water surface with experimental data (black dots)

Errors in water surface calculation for various turbulent models are presented in Table 1. It can be seen that k-ε model accuracy was considerably more than the other two models.

Table 1. Water surface error analysis for different modeling alternative

Time (s)	constant eddy viscosity	mixing length	k-ε
0.6	4%	4.3%	1.6%
1	5%	4.9%	3.5%
1.5	6.8%	6.7%	4.3%

Figure 13 shows the pressure and velocity field in the water body after 1 second using k-ε model. As can be seen in Figure 13, velocity vectors behind the wave front are downward while the velocity vectors in front of its forehead are upward showing the advancing wave to the end of the channel. .In addition, a relatively high pressure zone due to impact is observed prior to wave crest, due to wave progress.

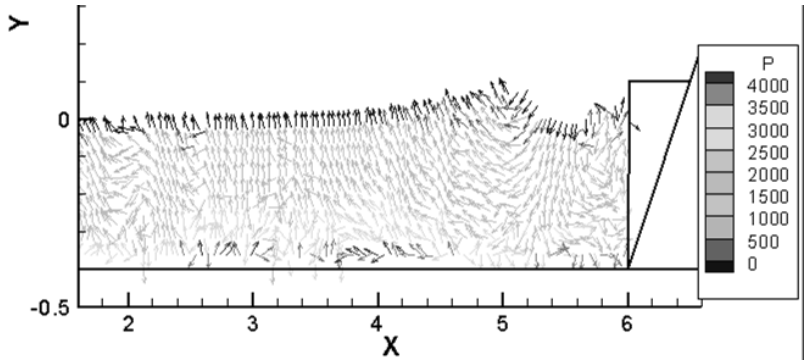


Figure 13. Computed velocity and pressure field after 1 s using k-ε model

6. Conclusion

In this article, a novel particle-based numerical model is developed using Moving Particle Semi-implicit (MPS) to simulate nonlinear hydrodynamic behavior of free surface water waves. In contrast with previous MPS models, with the aim of simulating turbulent nature of wave flows, the developed model has equipped with three turbulence models including constant eddy viscosity, Prandtl's mixing length theory and k-ε model. In addition, higher order of MPS operators was applied to suppress numerical oscillation in comparison with previous studies. The effect of applying various turbulence models on the MPS method in wave evolution is studied. To investigate the accuracy of the developed model, some wave problems such as wave propagation, wave run-up and landslide generated waves are solved numerically. Comparison of obtained results and data cited in the literature shows the ability of developed model in simulating water surface and pressure distribution in such complicated situation of wave motion. The stability and accuracy of MPS in modeling wave problems can be increased by implementing more complicated turbulence models such as k-ε instead of common constant eddy viscosity. This can be seen clearly in tsunami run-up and landslide simulations. Moreover, pressure field which is calculated implicitly and is predicted more precisely. Therefore, the model is capable to simulate complex and turbulent flows such as wave impacts, as it shown in tsunami test-case. In other word, in complicated intensive hydraulic gradient problems such as near shore, or in real case studies in which the effect of viscosity should be considered, the MPS model applying advanced turbulent models such as k-ε is more accurate than previous numerical models.

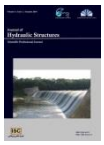
7. References

1. Gotoh, H., Sakai, T. (2006), Key issues in the particle method for computation of wave breaking, Coast. Eng., 53, 171-179.
2. Monaghan, J.J. (1994), Simulating free surface floes with SPH, J. Comput. Phys. 110, 399-406.
3. Koshizuka, S., Nobe, A., Oka, Y. (1998), Numerical analysis of breaking waves using the moving particle semi-implicit method, Int. J. Numeri. Meth. Fl., 26, 751-769.
4. Shakibaeinia, A., Jin Y.C. (2009), Lagrangian modeling of flow over spillways using the moving particle semi- implicit methods, Proceeding of 33rd IAHR Congress, Vancouver, Canada, 1809-1816.
5. Khayyer A., Gotoh, H. (2009), Modified moving particle semi-implicit methods for the prediction of 2D wave impact pressure, Coast. Eng., 56, 419-440.

6. Ataei-Ashtiani, B., Farhadi, L. (2006), A stable moving –particle semi-implicit method for free surface flows, Fluid Dyn. Res., 38, 241-256.
7. Zhang, S., Morita, K. Fukuda, K. and Shirakawa, N. (2006, An improved MPS method for numerical simulations of convective heat transfer problems, Int. J. Numeri. Meth. Fl., 51, 31-47.
8. Shibata, K., Koshizuka, S. (2007), Numerical analysis of shipping water impact on a deck using a particle method. Ocean Eng., 34,585-593.
9. Fayyaz, M. (2008), Numerical modeling of interaction between waves and coastal structures, M.S. thesis, Department of Civil and Environmental Engineering, Amirkabir University, Tehran, Iran.
10. Kondo, M., Suto, K., Sakai, M. and Koshizuka, S. (2008), Incompressible free surface flow analysis using moving particle semi-implicit method, Joint International Workshop: Nuclear Technology and Society- Needs for Next Generation, Berkeley, California, USA.
11. Khayyer A., Gotoh, H. (2010), A higher order Laplacian model for enhancement and stabilization of pressure calculation by the MPS method, App. Ocean Res., 32, 124-131.
12. Shakibaeinia, A., Jin Y.C. (2010), A weakly compressible MPS method for modeling of open-boundary free-surface flow, Int. J. Numeri. Meth. Fl., 63, 1208-1232.
13. Tanaka, M., Masunaga, T. (2010), Stabilization and smoothing of pressure in MPS method by quasi-compressibility, J. Comput. Phys., 229, 4279-4290.
14. Lee, B.H., Park, J.C., Kim, M.H., Jung, S.J., Ryu, M.C. and Kim, Y.S. (2010), Numerical simulation of impact loads using a particle method, Ocean Eng., 37, 164-173.
15. Kondo, M., Koshizuka, S. (2011), Improvement of stability in moving particle semi-implicit method, Int. J. Numeri. Meth. Fl., 65(6), 638-654.
16. Gotoh, H., Shao, S.D. and Memita, T. (2004), SPH-LES model for numerical investigation of wave interaction with partially immersed breakwater, Coast. Eng. J., 46(1), 39-63.
17. Shao, S.D., Gotoh, H. (2005), Turbulence particle models for tracking free surfaces, J. Hydraul. Res., 43(3), 276-289.
18. Shao, S.D. (2006), Simulation of breaking wave by SPH method coupled with k-ε model, J. Hydraul. Res., 44(3), 338-349.
19. Shao, S.D., Ji, C. (2006), SPH computation of plunging waves using a 2D sub-particle scale (SPS) turbulence model, Int. J. Numeri. Meth. Fluid, 51, 913-936.
20. Violeau, D., Issa, R. (2007), Numerical modeling of complex turbulent free-surface flows whit the SPH method: and overview, Int. J. Numeri. Meth. Fl., 53, 277-304.
21. Koshizuka, S., Oka, Y. (1996), Moving particle semi-implicit method for fragmentation of incompressible fluid, Nucl. Sci. Eng., 123(3), 421-34.
22. Suzuki, Y., Koshizuka, S. and Oka, Y. (2007), Hamiltonian moving-particle semi-implicit (HMPS) method for incompressible fluid flows, Comput. Meth. Appl. Mech. Eng., 196, 2876-2894.
23. Ataei-Ashtiani, B., Shobeyri, G. and Farhadi, L. (2008), Modified incompressible SPH method for simulating free surface problems, Fluid Dyn. Res., 40, 637-661.
24. Gotoh, H., Shibahara, T. and Sakai, T. (2001), Sub-particle-scale turbulence model for the MPS method- Lagrangian flow model for hydraulic engineering, Comput. Fluid Dyn. J., 9(4), 339-347.
25. Fayyaz, M., Kolahdoozan, M. (2010), Development of 3D MP-MPS model for flow pattern prediction during the intensive hydraulic gradient, J. Hydraul., 4(4), 33-50.
26. Shirazpoor, S. (2010), Numerical modeling of fluid flows in the vicinity of floating breakwater, M.S. thesis, Department of Civil and Environmental Engineering, Amirkabir

University, Tehran, Iran.
27. Kolahdoozan, M., Ahadi, M., Shirazpoor, S. (2014), Effect of turbulence closure models on the accuracy of moving particle semi-implicit method for the viscous free surface flow, Scientia Iranica Transaction A-civil Engineering, 21(4), 1217-1230.
28. Pan, X., Zhang, H. and Sun, X. (2012), Numerical simulation of sloshing with large deforming free surface by MPS-LES method, China Ocean Eng., 26(4), 653-668.
29. Mosaffa, M. (2014), Variable Resolution in WC-MPS Method for Fluid Flow Problems, MS thesis, University of Regina, Canada.
30. Tang, Z., et al. (2016), Numerical simulation of 3D violent free-surface flows by multi-resolution MPS method, J. Ocean Eng. Mar. Energy, 2, 355–364.
31. Ikari, H., et al. (2015), MPS-based Simulation of Scouring Due to Submerged Vertical Jet with Sub-Particle-Scale Suspended Sediment Model, J. of Japan Society of Civil Eng., Ser. B2 (Coastal Eng.) 71, 19-24.
32. Harada, E., et al. (2017), Numerical simulation for sediment transport using MPS-DEM coupling model, Advances in Water Resources, in press.
33. Harada, E., et al. (2018), Numerical Investigation of the Morphological, Dynamics of a Step and Pool Riverbed Using DEM-MPS.", Journal of Hydraulic Engineering, 144(1)
34. Gotoh, H., Khayyer, A. (2018), On the state-of-the-art of particle methods for coastal and ocean engineering, Coastal Eng. J., in press.
35. Schlichting, H. (1960), Boundary layer theory, McGraw-Hill Book Company, USA, 647.
36. Henderson, F.M. (1966), Open channel flow, Macmillan Publishing Co., Inc. New York, USA.
37. Kolahdoozan, M. (1999), Numerical modelling of geomorphological processes in estuarine waters, Ph.D. thesis, Department of Civil and Environmental Engineering, University of Bradford, Bradford, U.K.
38. Rodi, W. (1980), Turbulent models and their application in hydraulics- a state of the art review, Book Publication of IAHR, Delft, Netherlands.
39. Datta, B.N. (1995), Numerical linear algebra and applications, Brooks/Cole Publishing Company, USA.
40. Monaghan, J.J., Kos, A. (1999), Solitary waves on a cretan beach, J. of Waterw. Port Coast. Ocean Eng., 125(3), 145-154.
41. Shobeyri, G., Afshar, M.H. (2010), Simulating free surface problems using Discrete Least Squares Meshless method, Computers & Fluids, 39, 461–470.
42. Gedik, N., Irtem, E. and Kabdasli, S. (2005), Laboratory investigation on tsunami run-up, Ocean Eng., 32, 513-528.
43. Dean, R.G., Dalrymple, R.A. (1991), Water wave mechanics for engineers and scientists, Advanced Series on Ocean Engineering, World Scientific, Singapore.
44. Qiu, L.C. (2008), Two-dimensional SPH simulation of landslide-generated water wave, J. Hydraul. Eng., 134(5), 668-671.
45. Heinrich, P. (1992), Nonlinear water waves generated by submarine and aerial landslide, J. Waterw. Port Coast. Ocean Eng., 118(3), 249-266.

Journal of Hydraulic Structures
***J. Hydraul. Struct.*, 2018; 4(1): 36-54**
DOI: 10.22055/JHS.2018.24985.1075



OPEN ACCESS

Ocean Currents Modeling along the Iranian Coastline of the Oman Sea and the Northern Indian Ocean

Morteza Jedari Attari[1]
S. Abbas Haghshenas[2]
Arash Bakhtiari[3]
Mohammad Hossein Nemati[4]

Abstract

The Makran Coast (Iranian Coastline of the Oman Sea on the Northern Indian Ocean) plays an important role in country's future navigation and trade due to its accessibility. In 2014, the Iranian Makran coastline was selected by the PMO to be studied as the Phase 6 in the series of Monitoring and Modelling Studies of Iranian Coasts with all disciplines being in investigated including currents. All previously measured current data (in 2006, 2007 and 2008) along the Makran coastline showed an oscillating (reversing) alongshore currents with no detectable dominant frequency. The oscillation period of these currents varies approximately from 3 days to a week. The most significant objective of this study was to simulate the oscillating behaviour of the Makran coastal currents. In this regard, the global oceanic current pattern over the Northern Indian Ocean was simulated using a 3-dimensional non-structured model and comparisons with the data from several global resources have been made. The model was calibrated using the available vertical current profile data along the coastline.

Keywords: Ocean Currents, Circulation Patterns, Numerical Modelling, Oman Sea

Received: 18 February 2018; Accepted: 08 May 2018

1. Introduction

The southeast coast of Iran bordering the western Makran region is exposed to the Indian Ocean (see Figure 1) and is directly affected by the climate and hydrodynamic processes of this ocean [1]. Measurements of currents by the Port and Maritime Organization (PMO) [2] in 2006-7 around Chabahar and by the Iranian Fishery Organization (IFO) [3] in 2008 at Zarabad, have

[1]Visiting Researcher, Institute of Geophysics – University of Tehran, Iran.
[2] Institute of Geophysics – University of Tehran, Iran, Email: sahaghshenas@ut.ac.ir (**Corresponding author**)
[3] 3)Project engineer, Middle East Water and Environment Co., Tehran, Iran.
[4] 4)Iranian Ports and Maritime Organization, Tehran, Iran.

CC BY

shown the presence of oscillating ocean currents along this coastline. These currents reverse every 3 days to a week. They are typically strong through the water column with the near-bed current velocity reaching up to 0.5 m/s at 20~30 m depth.



Figure1. Study area

The Indian Ocean (especially at the northern hemisphere) is under effects of two distinct climate conditions. In the winter monsoon, strong winds blow from the North-West and head towards South when they reach to Somalian Coastline. In the summer monsoon, the direction totally reverses and winds blow from the South-West heading straight towards Makran Coastline [4]. Consequently the major ocean currents of the northern Indian Ocean such as Somali Current gradually develop and strengthen and eventually disappear twice a year trying to adjust themselves with the wind.

Even though oceanic currents (in the Indian Ocean) have been investigated by several researchers, the influence of global oceanic currents on Makran coastal currents has not been probed so far. Figure 2 was illustrated by NASA [5] using an assimilative model representing the North Indian Ocean currents. As it appears in the figure, except for the two East-West elongated regions which are indicated by blue boxes, the rest of the ocean carries strong and dynamic currents.

In analogy to the mentioned fact, Lopez et.al [6] were focusing in the Bay of Bengal and developed a global model for the Northern Indian Ocean setting the open boundary at S20 Tropic. Their model's grid size was 0.5 degree and 38 vertical layers was applied in their model which adequately was able to simulate the Bay of Bengal currents.

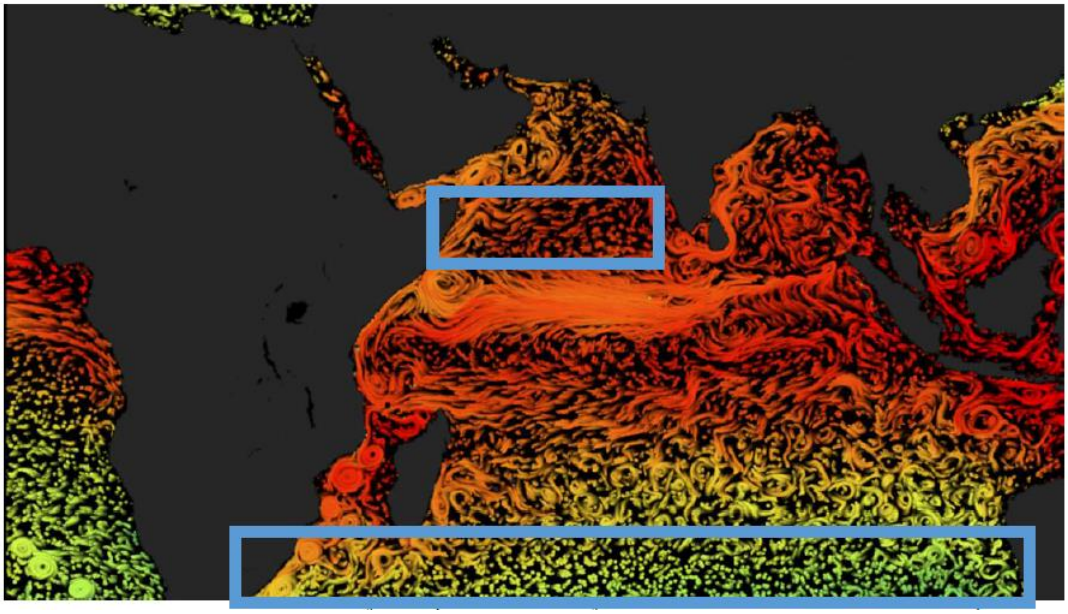


Figure2. The North Indian Ocean Currents

According to Aneesh [7] (based on a modelling results), the accuracy of model results, significantly enhances by considering the water level variations at the southern boundary at S30 Tropic along with density variations in a 3D model. In another attempt by Kurian & Vinayachandran [8], in a model with a same domain and a grid size of 0.25 degree, in spite of setting the open boundary at 30S Tropic as a closed wall, the model results did not affected at the Indian Coasts. Kawamiya and Oschlies [9] also obtained the desirable results with a similar domain. L'Hégaret [10] applied a semi-local HYCOM model to the similar domain and compared the results to the observed ARGO data [11] inside the domain which showed a good consistency. It is noted that he used the data from the global HYCOM model [12] as the initial and open boundary condition.

According to the literature review, it is concluded that, it is necessary to adopt a 3-dimensional baroclinic model in order to simulate the oceanic currents along the coastlines of the Oman Sea including the Makran Coasts.

2. Measured data

Figure 3 shows all the data locations which were gathered and extracted for calibration and verification purpose in this study. An invaluable data set recorded during the first phase of the monitoring projects (by PMO) [2] includes current profile measurements in 25 m depth at a location outside Chabahar Bay. Measurements at this location cover the period from September 2006 until early June 2007 immediately after the Cyclone Gonu event. The oscillating ocean currents have been captured in this data set. The deployed current profiler device (i.e. bottom-mounted AWAC) also recorded water temperature near the seabed. A number of tide gauges deployed inside and outside of Chabahar Bay measured the water level. The location of the current profiler AW2 is E60.65 N25.26 and Tis tide gauge (TG1) located at E60.594 N25.35. Figure 4 illustrates the current rose of recorded data by AW2.

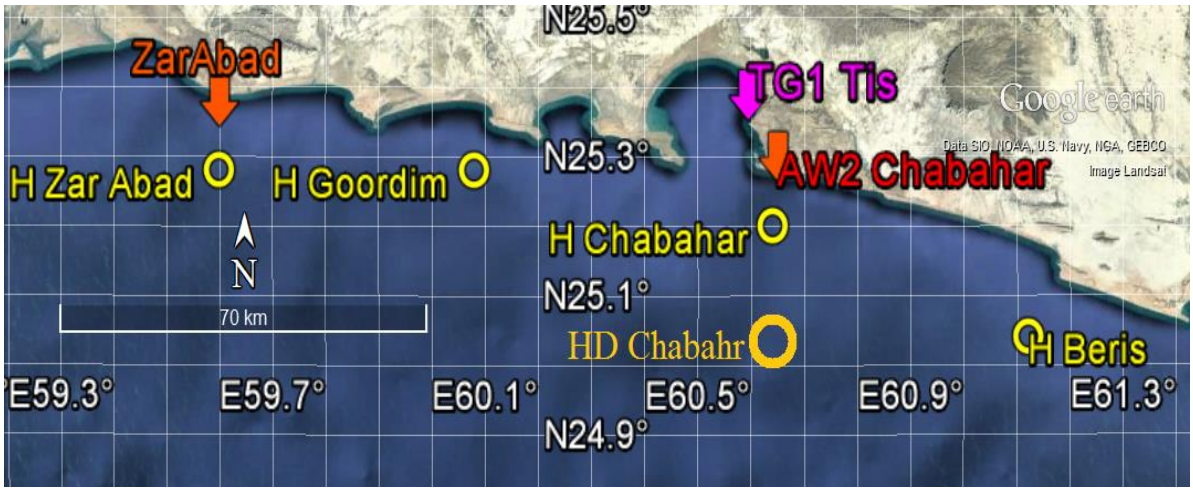


Figure3. Locations of the data collection stations

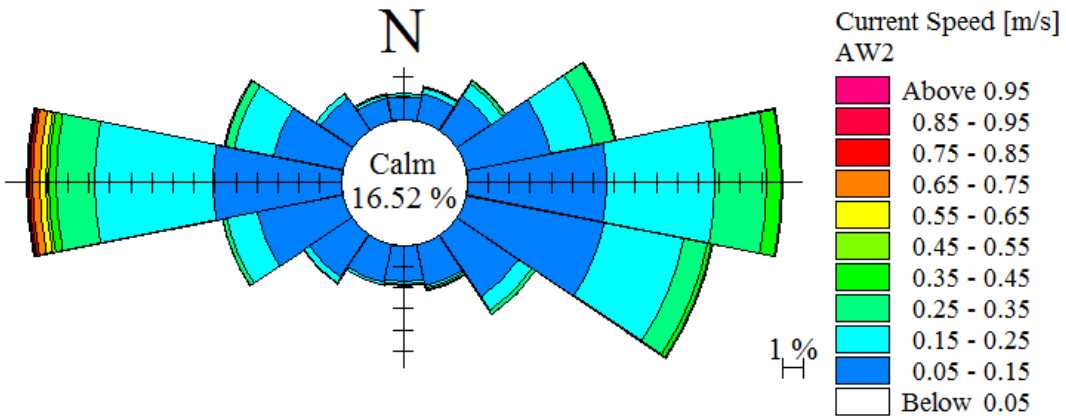


Figure4. AW2 data current rose

In 2008 another bottom mounted AWAC (in 19 m depth) was deployed at ZarAbad vicinity (E59.6 N25.28) by IFO [3]. Similar patterns of current direction in this 4-month-long data (July to October) indicated that the mentioned pattern of oscillating currents dominates the Makran coastline.

In addition to the measured current data which fall in the shallower edge of the continental shelf, daily surface current, water level, and temperature data from global HYCOM [12] assimilative global model developed by the USACE in collaboration of NASA, NOAA and several universities worldwide, were also collected for the last three months of 2006 to be used for evaluating the model performance in the deeper areas. The data is available at 1/12 degree spatial resolution.

3. Methodology

Due to importance of geostrophic currents and the relatively deep water conditions in the Makran area, a 3-dimensional hydrodynamic model had to be used for proper simulation of oceanic currents.

MIKE3 by DHI software has been adopted in order to investigate the currents and sea level variations. The ability of this model in resolving geostrophic processes was investigated through applying the model to a well-known experiment described by Tartinville, et al. [13]. The domain is a 20 m deep and 30 km × 30 km open sea region. The latitude was chosen as 52° N and hence the Coriolis parameter is set to 1.15×10^{-4} s^{-1}. The horizontal grid resolution is 1 km and 20 vertical levels were used. In the centre of the domain, a 10 m deep, 3 km radius cylinder of relatively freshwater is placed in the upper layer. Simulations are performed for 144 hours without any bottom or surface stress. They approved that IFREMER and Delft3D models' results are in consistency with the observed values. Comparing the model results with the data and other already approved 3-dimentional hydrodynamic model results showed that MIKE3 is acceptably capable of resolving 3D geostrophic oceanic currents (Figure 5).

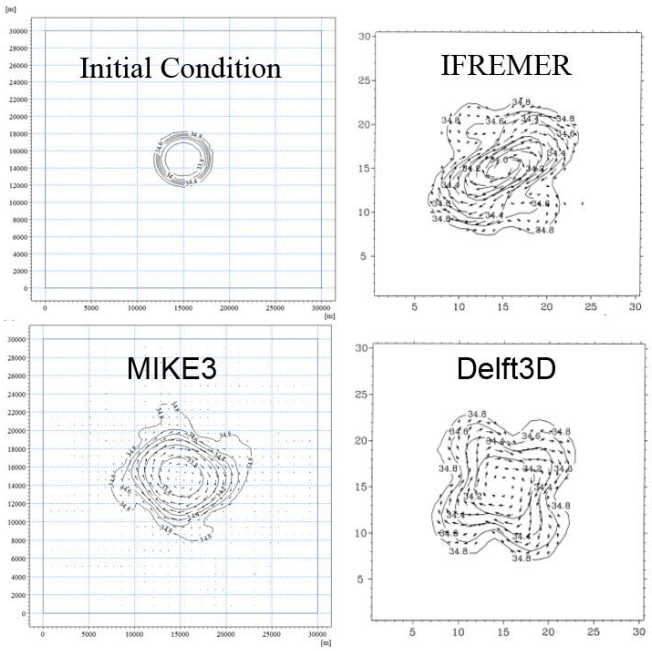


Figure5. Sea surface salinity and velocities through the center of the central eddy at the beginning and end of the experiment. Top left panel: Initial condition, Top right panel: IFREMER Model, Bottom right panel: Delft3D model, Bottom left panel: MIKE3 model

4. Numerical modeling

Simulations started from the beginning of 2006 to allow model warm up and convergence of the temperature field. The last four months of 2006 was selected for the model calibration period. Required initial and boundary conditions data for currents, water level, and temperature fields were obtained from publicly available sources such as Global Ocean Physical Reanalysis System (C-GLORS) [14]. The wind and pressure field data obtained from European Centre for Medium-Range Weather Forecasts (ECMWF) which then implemented in WRF model in order to increase the accuracy by adding meso-scale equations [15]. The global wind field have a coarse resolution of 0.25 degree and a time step of 6 hours, the wind field provided [6] for this simulation has 0.1 degree spatial resolution and the time step of 1 hour. Considering the

temperature variations in the model implies the need for air temperature, short and long wave radiation data as well. Also, sea surface change data was obtained from CCAR [16].

Finding the most appropriate model configuration that can properly simulate large scale oceanic processes was a matter of trial and error. Applying various domains showed that obtaining reasonable results requires adopting a domain far larger than the study area boundaries. The mesh size, number and form of vertical layers also play a significant role in the validity of the model results. Eddy permitting grid resolution of 0.3 degree was selected for the ambient oceanic domain while the grid size decreases to 0.01 degree (≈1 km) near the Makran area. Figure 6 shows the final selected model domain which extends to the southern hemisphere. The bathymetry data was obtained from ETOPO1 [17] which is combined to the existing local hydrography data provided by PMO.

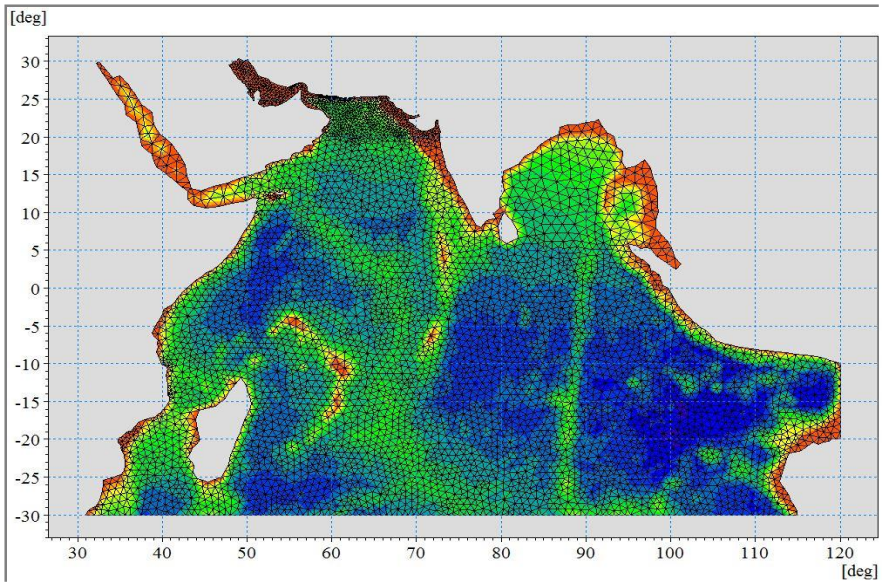


Figure6. Computational domain

In the middle of the Indian Ocean, water depth reaches to approximately 5000 m. Therefore a combined vertical layer grid was used. 10 sigma layers at the surface followed by 47 Cartesian layers in the deep ocean. This configuration ensures well utilizing the sigma layer ability in accurate water level change calculations as well as avoiding the deficiency of sigma layer in resolving the large depth differences and steep slopes where its supposedly almost horizontal interfaces has to place almost vertical at ocean edges and around underwater mounts which results in fatal numerical divergences.

Computational time step of 120 s revealed to be small enough which below that, no changes appeared in the results. Although as a deep ocean model, the global current field is not sensitive to bed roughness, comparisons on the results and data from current profilers in the shallower edge of the continental shelf (AW2 and ZarAbad) showed that model results are more consistent when the parameter was set 0.002 m.

Table 1 presents a summary of distinguishing features of some model calibration versions. It is noted that except for cc_N20_01 and cc_N10_03 which the southern boundary was placed at N20 and N10 Tropics, respectively, the rest of the models has a Southern boundary at S30 Tropic and an Eastern boundary at E120 Mercator. In order to avoid repeating the similar characteristics of calibration models, only the changed parameter is mentioned in front of each

model version, i.e., if a feature mentioned for a model at above row is not mentioned in the next row implies that the feature is duplicated from above and no changes have been made in that regard.

Three Groups of models with the large domain appear in Table 1. Models titled cc_S30_03's major feature is having closed boundary while to others, i.e., cc_S30_12s and cc_S30_14s use C-GLORS current and temperature data along with CCAR data for surface elevation at the open boundary. cc_S30_12s group uses the standard mesh (sea Figure 6) while the latter group uses a mesh which its grid size in the vicinity of Makran area is divided in half.

Small and medium domains are not capable of reproducing the real patterns in the currents of Makran. The reason is that, the open boundary in those models is too close to the area of being concerned and because there was no accurate data available to apply at the boundary, we had to set it as a close boundary or use 1-month averaged 3-D current data from C-GLORS which obviously is not appropriate for that purpose. Never the less C-GLORS 1-month averaged current and temperature field data was used for the initial condition of the model which because of considering an 8-month warm up period, the results were not affected. In the larger domain however, most of the oceanic gyers which affect the Makran Coastline are reproduced within the domain and the effect of far located open boundaries conditions fades out.

The numerical scheme for resolving the vertical eddy viscosity plays a significant role in the model performance. Trying k-epsilon turbulence scheme resulted in intensified stratification which separates a thin film of warmer water layer at the surface dragged intensely by the wind force while the rest of the vertical column remains detached from the governing forces and as a consequence colder than recorded temperature and mostly stagnant. On the other hand, log-low formulation represents milder stratification in the simulations, resulting in better consistency both for current direction at the surface and temperature at the bottom layer. It should be noted that, wind friction parameter significantly affects the results.

Table1. Model Calibration Versions Characteristics.

Model	Features
cc_N20_01	Small Domain & Open Boundary Condition (OBC) = closed boundary & Vertical Eddy Viscosity (VEV) = log-law & Wind Friction (WF) = 0.0026 & Initial Water Level Condition (IWLC)= uniform zero & Initial Current Filed (ICF) = stationary & Vertical Temperature Dispersion (VTD) = 0 & Horizontal Temperature Dispersion (HTD) = 0, & No Evaporation
cc_N10_03	Medium Domain
cc_S30_03	Large Domain
cc_S30_03_01	With Computed Evaporation
cc_S30_03_02	VEV = k-epsilon
cc_S30_03_03	WF = varying linear (0.0012~0.0024)
cc_S30_03_04	WF = varying linear (0.0017~0.0024)
cc_S30_12	OBC = S30: level CCAR and free currents, E120: level CCAR and currents from C-GLORS & VEV = log-law & WF = 0.0026 & IWLC = CCAR & ICF = C-GLORS
cc_S30_12_01	VEV = k-epsilon
cc_S30_12_02	WF = 0.0022
cc_S30_12_03	WF = 0.0019
cc_S30_12_04	VEV = log-law & WF = 0.0030
cc_S30_12_05	WF = 0.0040
cc_S30_12_06	VEV = k-epsilon & WF = 0.0026 & VTD = 1
cc_S30_12_07	HTD = 1

cc_S30_14	fine mesh & VEV = log-law & WF = 0.0026 & VTD = 0 & HTD = 0
cc_S30_14_01	VEV = k-epsilon & WF = 0.00245 & VTD = 1 & HTD = 1
cc_S30_14_02	VTD = 1.5
cc_S30_14_03	VTD = 3
cc_S30_14_04	VTD = 4.5

Three variables have been investigated in an analytical analysis in order to detect the most appropriate model setting. Summaries of comparisons with HYCOM data at four points located at 100 m depth and one point at 600 m depth (sea Figure 3) for surface u-velocity component, v-velocity component and temperature appear in Figure 7, 8 and 9 respectively.

Same approach has been adopted in order to investigate the ability of the model in simulation of recorded data by AW2. Figure 10 represents summaries for correlation coefficient (CC) and root mean square of errors (RMSE) for three mentioned variables. It is noted that the temperature recorded by AW2 stands for sea bottom temperature (in contrary to HYCOM data which belong to surface).

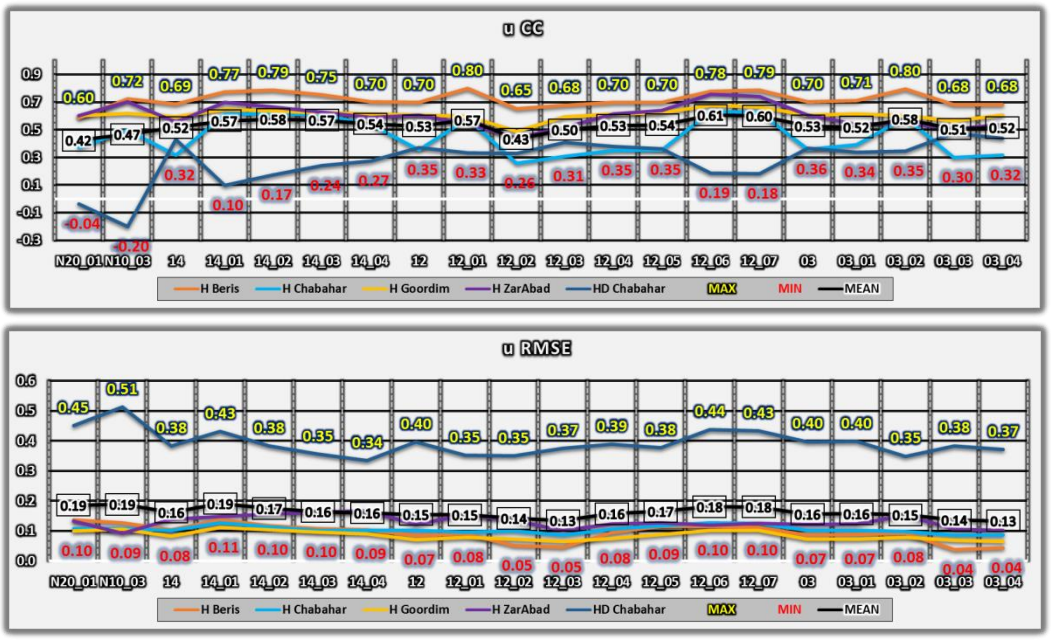


Figure7. Correlation coefficient and RMSE of surface u-velocity component for model results and HYCOM data

Another major role playing variable on this decision is, the water level variation. Using a closed boundary at the lateral openings of the model seems that does not affect the current or temperature filed while it has a significant influence on water level variation. The comparisons on model results and the surge filtered from the tide gauge at Tis (TG1) showed that applying CCAR 7-day averaged sea surface data at the model boundary extremely enhance the model accuracy. The data from the tide gauge (Tis) was filtered applying a Fast Fourier transform and the surge was obtained. The model results at the location of the tide gauge extracted and compared to the data which is shown in Figure 11. The model accurately simulates the arising surge due to Cyclone Gonu. It is noted that the results from cc_S30_03 were shifted 0.2 m

upward in order to fit the data while the results from cc_S30_12_04 are already in consistency with the observed levels.

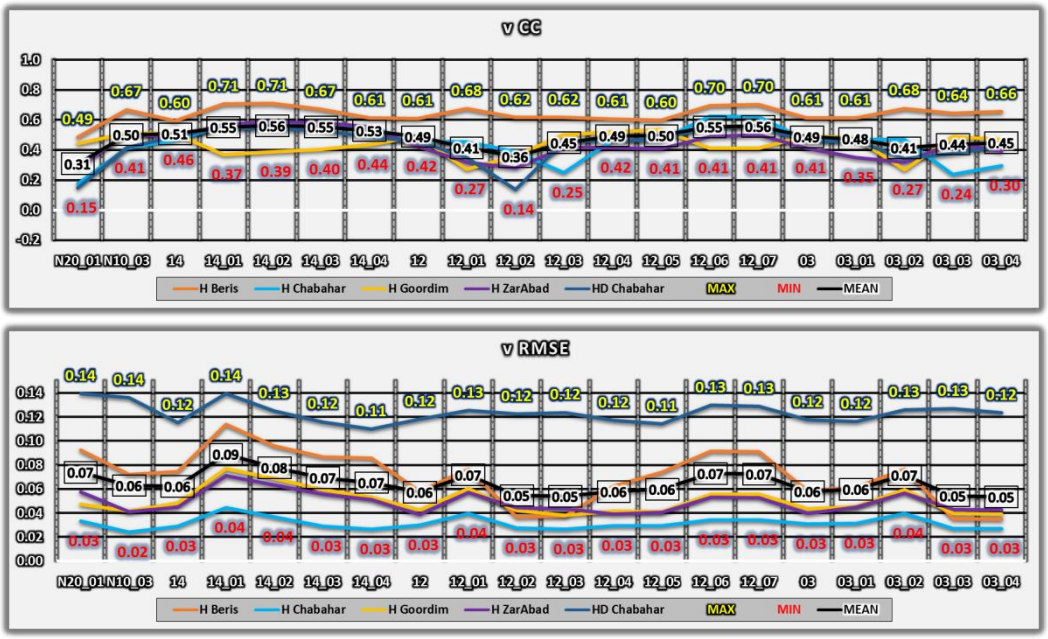


Figure 8. Correlation coefficient and RMSE of surface v-velocity component for model results and HYCOM data

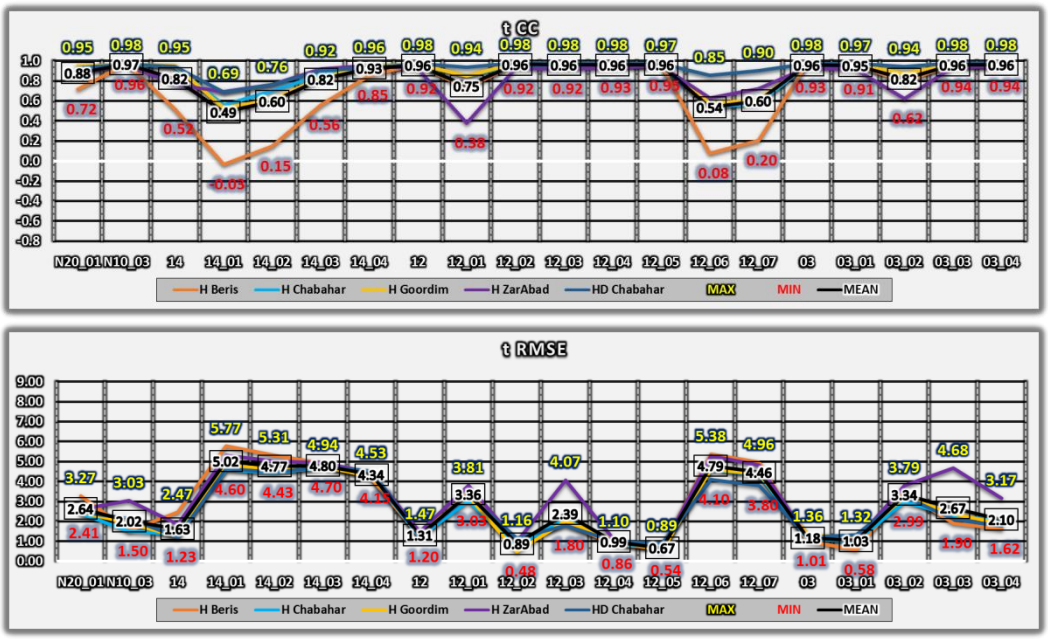


Figure 9. Correlation coefficient and RMSE of surface temperature for model results and HYCOM data

Analytical analysis revealed that using cc_S30_12_04 provides the best results. It is also revealed that decreasing the grid size in spite of having a devastating effect on computational time/cost does not improve the model results.

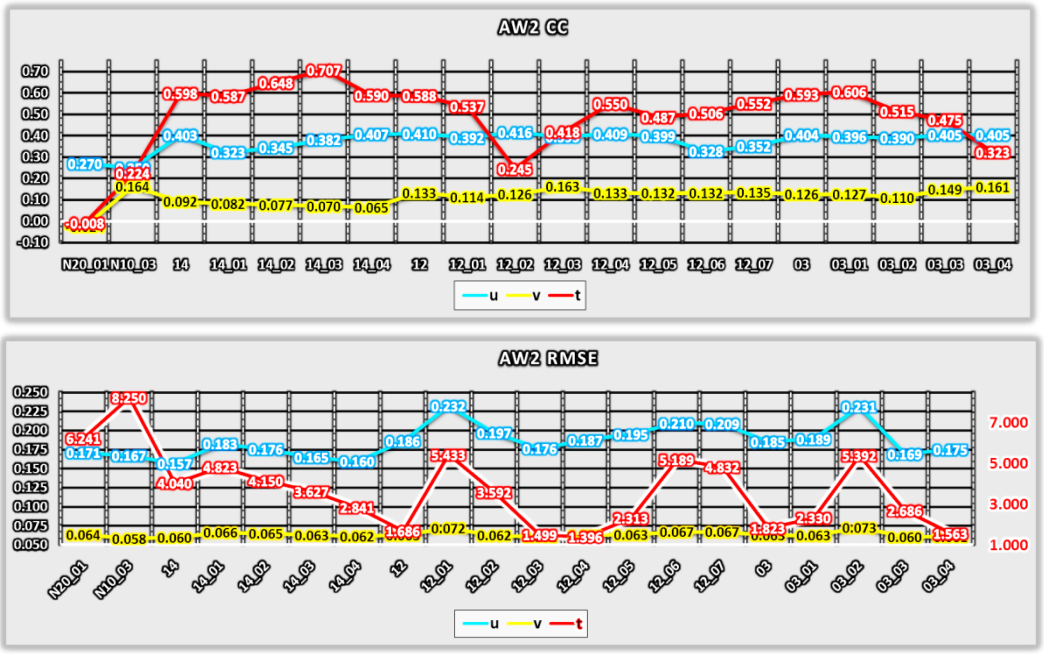


Figure 10. Correlation coefficient and RMSE of surface temperature for model results and HYCOM data

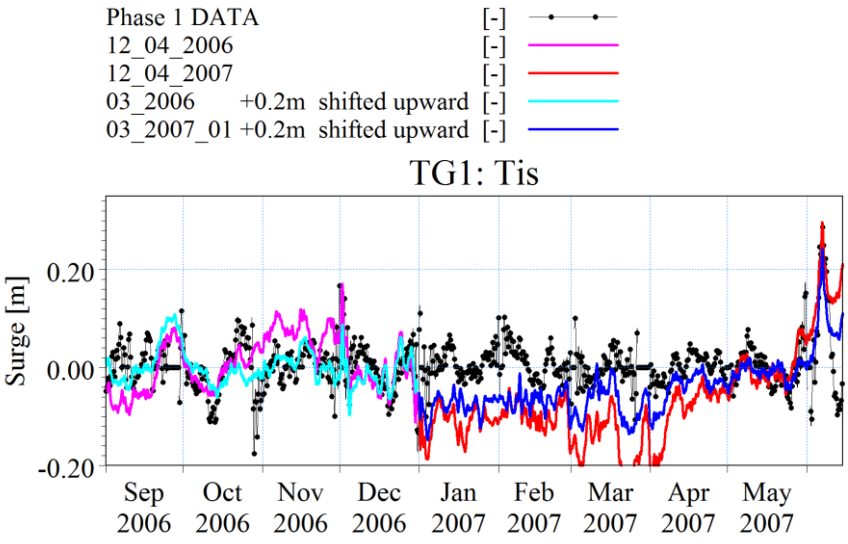


Figure 11. Comparisons on computed sea level change and filtered surge from Tis tide gauge

5. Results and discussion

Current speed and direction, sea surface elevation and temperature are the main outputs of the model which were compared to the collected data. An example comparison between the AW2 current profiler data and model results is presented in Figure 12. The figure provides comparison between surface currents and indicates that the model can reasonably reproduce the ocean current regime in Makran area. The oscillating nature of ocean currents is well reproduced. Current speeds are also reasonably simulated (a perfect match is not expected due to the extremely complex nature of the problem). The bottom panel in Figure 12 depicts the simulated temperature fluctuations near the seabed showing good consistency with the measured data.

Cyclone Gonu was an extreme event that took place in early June 2007. This event was recorded by the AW2 sensor. Figure 13 depicts comparisons between a selected section of the recorded data (black dots) and model results, demonstrating a great performance by the model in reproducing ocean currents along the Makran coastline. At the beginning of 2007 simulations were continued in two versions using two different temperature fields. The red line shows the results with the temperature field taken from the end of 2006 simulation, i.e., the simulation continued without any changes. The blue line was produced by a simulation whose initial temperature field was replaced with the data from C-GLORS (with other parameters such as velocity and water surface levels from the end of 2006).

As it appears in Figure 13, importing the temperature field from end of simulation at 2006 and using C-GLORS data, does not show a significant difference in the results of the model for 2007. This implies that the model's calculated temperature field in 2006 (by the end of one year simulation) is in a good consistency with the observed data.

The simulation was extended for 2008 using the same setting. Figure 14 illustrates a comparison between model results and ZarAbad data. Same patterns both in data and model results appear in this figure which implies that the simulations are adequately and consistently representing the oscillating currents along the Makran Coastline.

The model performance in simulating the Makran currents can also be seen through comparison between current speed simulated by the model and recorded by AW2, in the middle and bottom layers (Figure 15). As it appear in Figure 15, the trends of current speed variations are similar at surface, middle and bottom layers, however the magnitude of current speed is smaller near the bottom, which is expected for a mostly wind induced current.

Cyclone Gonu which is the most significant and devastating detected phenomenon in the region, was well simulated and this ensured that the modelling has achieved its engineering purposes. Figure 16 represents a snapshot showing the currents induced by Cyclone Gonu landing at Makran Coasts on 7th of June 2007.

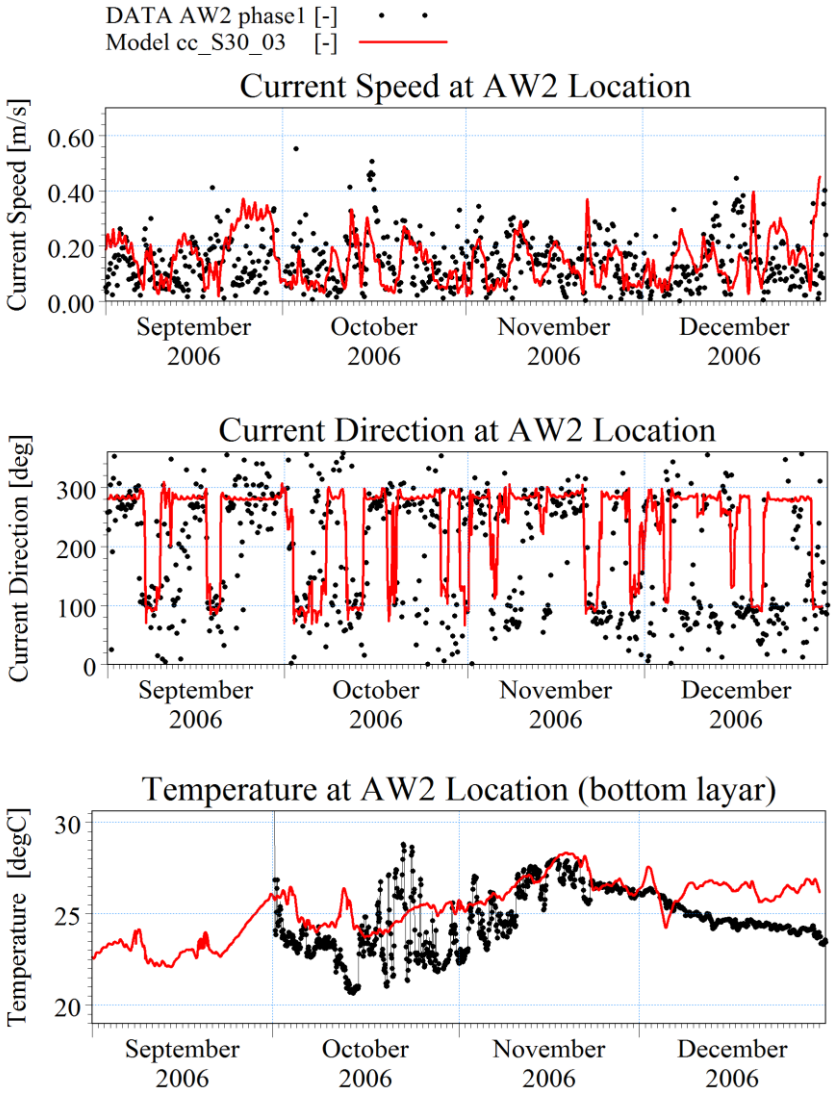


Figure 12. Comparisons between AW2 data (black) and model results (red).

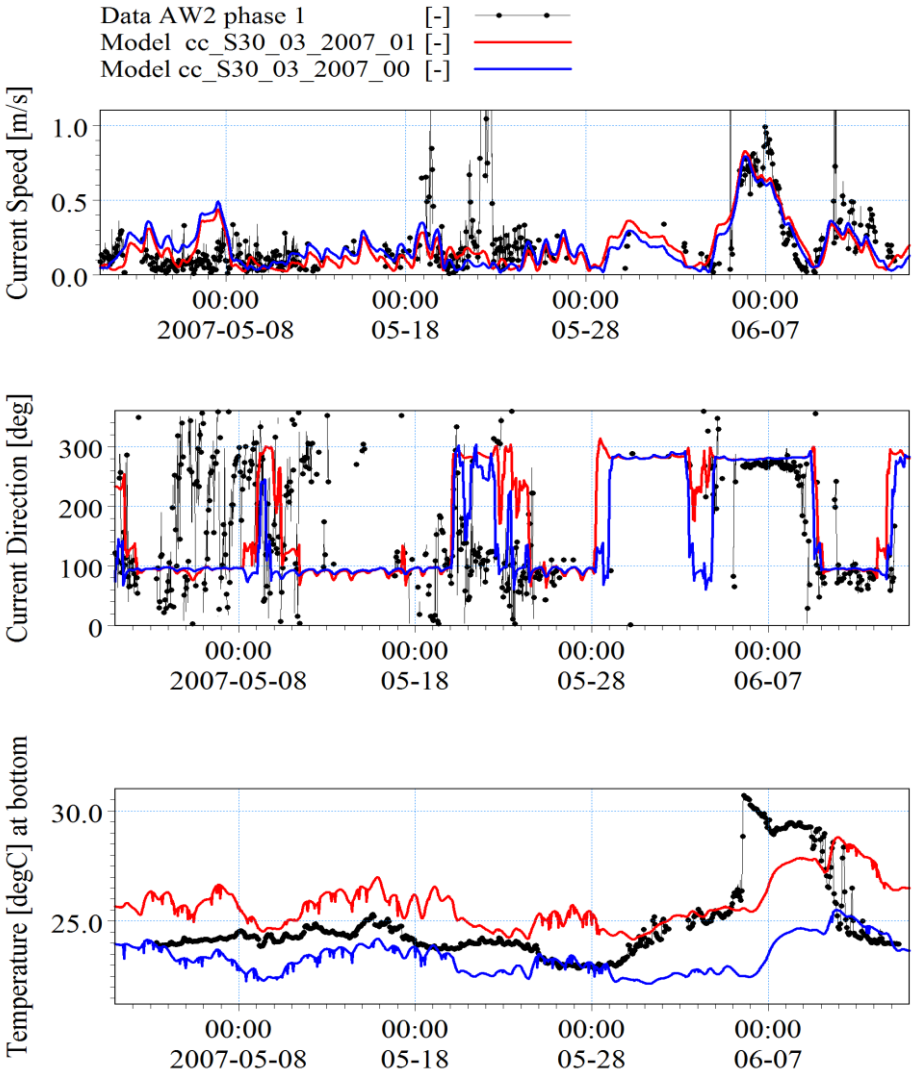


Figure 13. Comparisons between AW2 data (black) and model results (red) during cyclone Gonu.

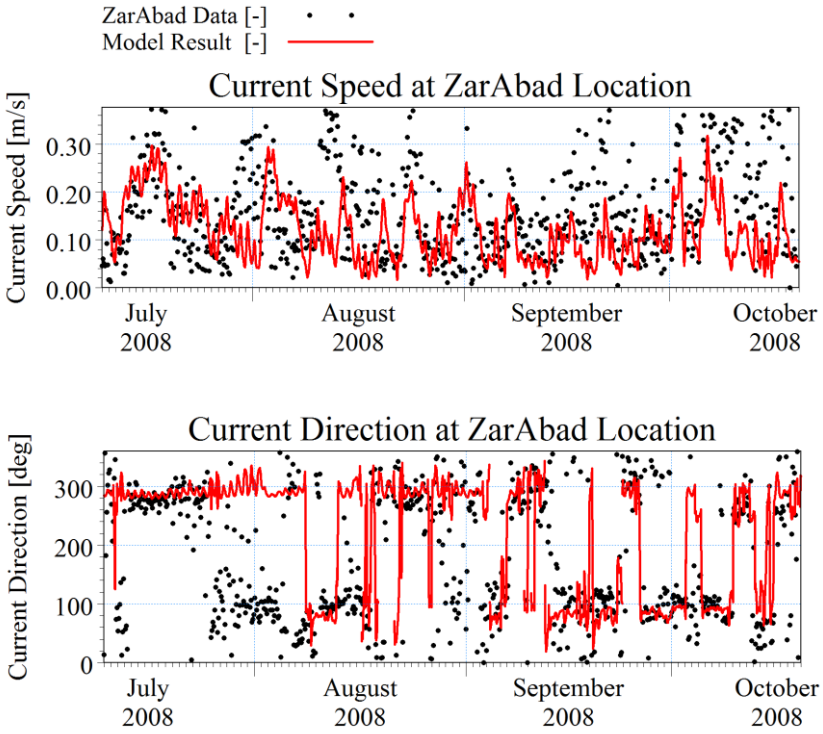


Figure 14. Comparisons between ZarAbad data (black) and model results (red).

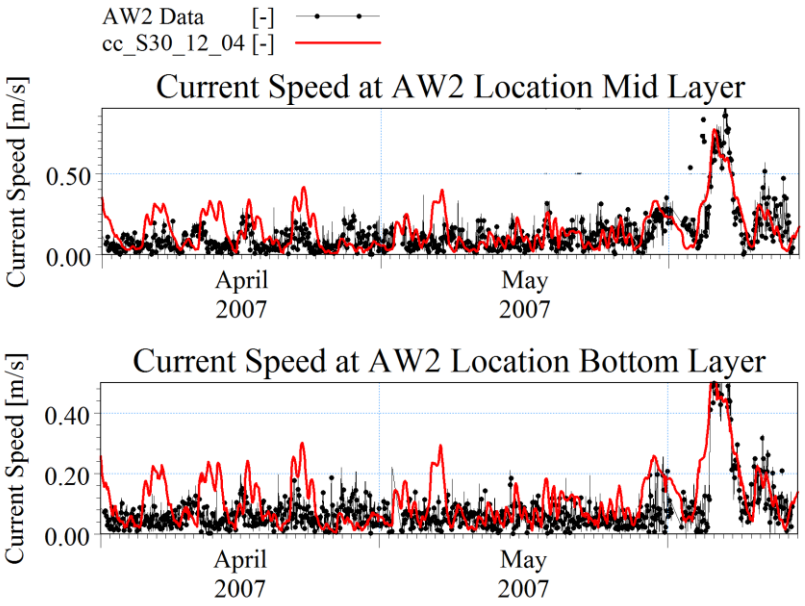


Figure 15. Comparisons on recorded (black) and simulated (red) current speed at AW2 in middle and bottom layers.

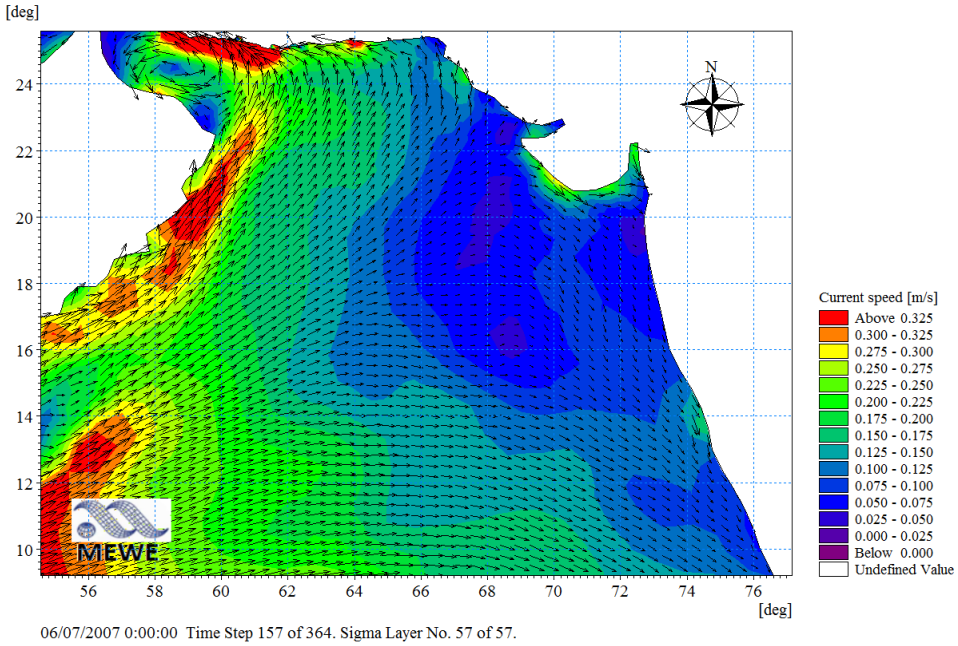


Figure 16. Currents induced by Cyclone Gonu on 7th of June 2007.

As a general ocean model, several criteria can be evaluated in order to validate to results including general current patterns, seasonal surface temperature filed and sea surface heights. Two monsoon seasons in the Northern Indian Ocean are characterized by the wind direction (Figure 17). While the trade wind below the Equator always blow towards the North-West, monsoon winds direction changes seasonally. Therefore two distinguished current pattern appear in this region.

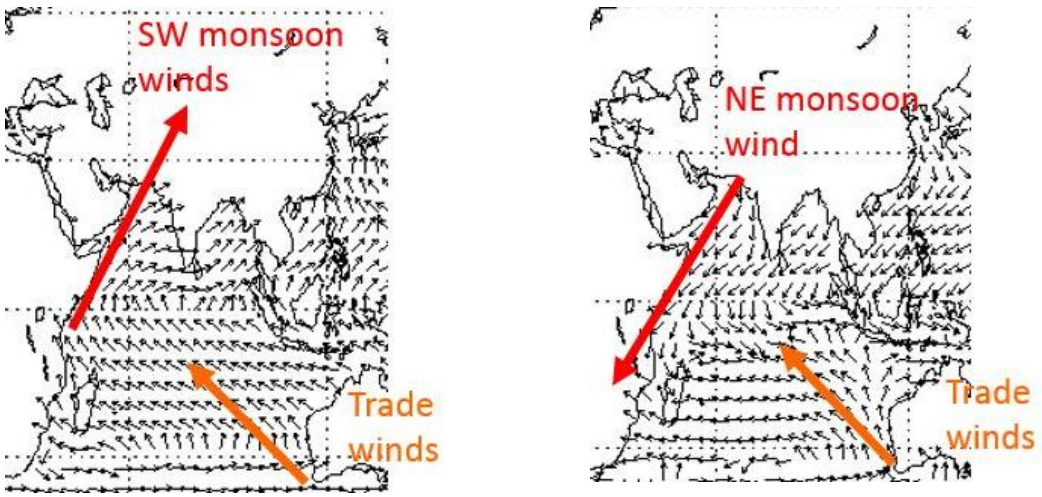


Figure 17. North Indian Ocean summer SW (left panel) and winter NE (right panel) monsoon winds

Figure 18 shows a comparison between currents simulated by the model in this research (green-dashed arrows) and satellite data analyzed by Shankar [4] (black-bold) arrows) for summer and winter monsoons. Nearest general current to the Makran Coasts is West Indian Coastal Currents (WICC) which in summer heads towards South-East and in winter towards

North-West. Somali Current (SC) adjusts it direction to the wind and subsequently is northward during summers and southward during winters. Winter Monsoon Current (WMC) passes through the South of India towards the West in winters. During summers, it is called SMC which its direction is eastward.

Geostrophic currents are oceanic flow in which the pressure gradient force is balanced by the Coriolis Effect. The direction of geostrophic flow is parallel to the isobars. Sea Surface Height (SSH) variations across the ocean are developed by variations in the air pressure, wind stress (surge) and variations in water density. SSH is a representative for pressure gradient in the ocean which forms isobars. Figure 19 illustrates SSH of the Northern Indian Ocean during winter extracted from ERDDAP [18] data in comparison with simulation results. Even though, subtle discrepancies are seen in the figure, the general SSH pattern seems to be well reproduced in the model.

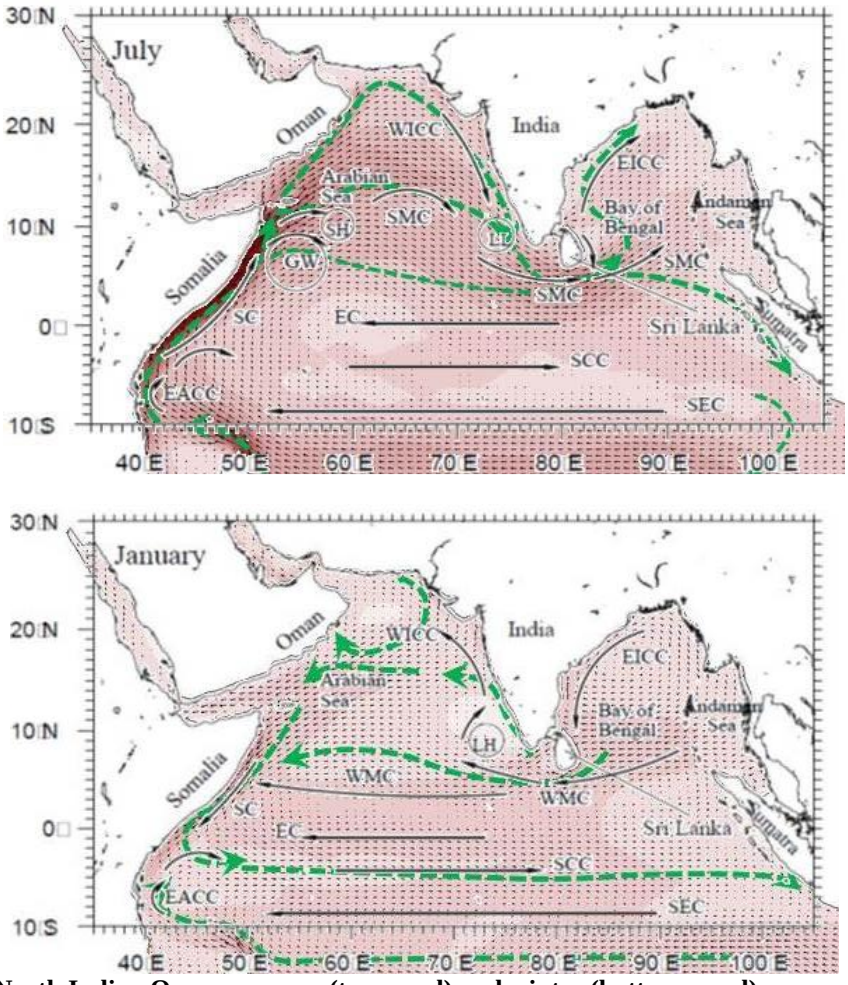


Figure 18. North Indian Ocean summer (top panel) and winter (bottom panel) monsoon currents.

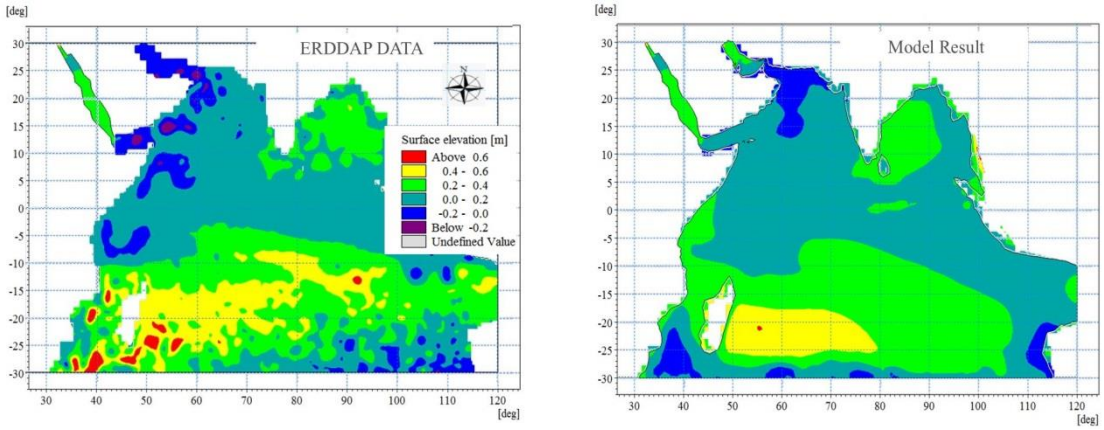


Figure 19. North Indian Ocean SSH; ERDDAP data (left panel) and model results (right panel)

Great Whirl (GW) which appears in Figure 18, an eddy which transports the water from Somali coasts towards east (offshore) reaches to its most developed stage in August. This causes coastal upwelling and appears as an abrupt drop in Sea Surface Temperature (SST) at its location. Figure 20 illustrates a comparison between Modis Satellite data analyzed by Savtchenko [19] and model results. Dashed circles locate the decreased SST caused by GW.

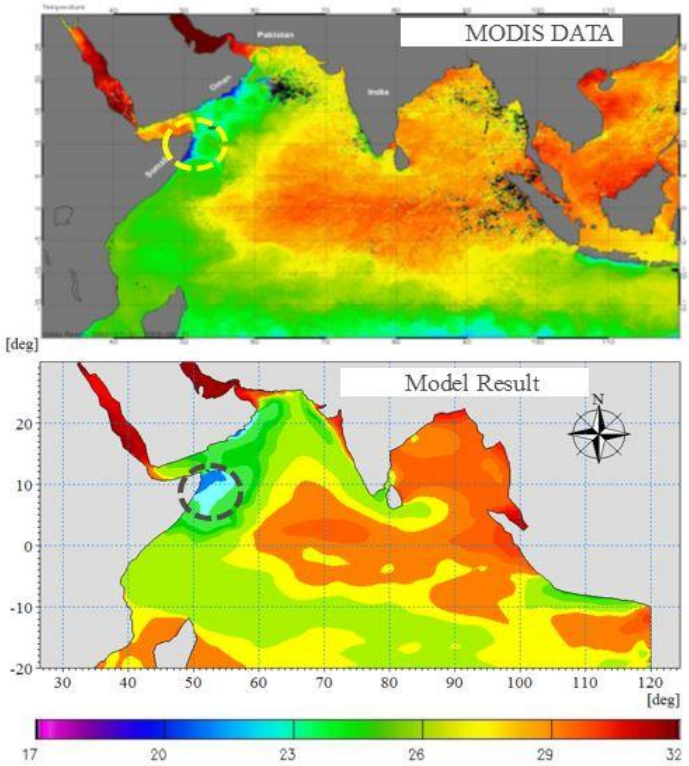


Figure 20. North Indian Ocean SST during summer monsoon; Modis Satellite data (top panel) and model results (bottom panel)

6. Conclusion

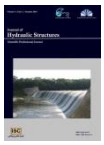
This paper presents the results of a 3D modelling effort for simulating the hydrodynamics of Makran ocean currents as well as their corresponding water level variations. Currents and sea levels in the Oman Sea are impacted by Indian Ocean. The data used for model calibration and verification were recorded in approximately 25 m and 19 m depth which fall in the shallower edge of the continental shelf just before the beginning of the transition zone to coastal currents. Moreover the capability of the model in reproducing the Northern Indian Ocean currents, SSH and SST was evaluated through comparisons with available data and literature.

7. References

1. Dibajnia, M., M. Jedari Attari, A. Bakhtiari, M.H. Nemati, S.A. Haghshenas (2016) Modelling of ocean currents and surge along the Iranian Makran coastline on the Oman Sea, *Proceedings of 12th ICOPMAS,* Tehran, Iran. pp. 51-52.
2. Jahad Water and Energy Research Company (JWERC) (2008) Study reports of "Monitoring and Modelling Studies of Parts of Sistan, Balouchestan and Boushehr Provinces", *Ports and Maritime Organization (PMO)*.
3. Darya Negar Pars Company (DNP) (2008) Study reports of "Waves and Currents data measurements in the vicinity of ZarAbad", *Iranian Fishery Organization (IFO)*.
4. Shankar, D. (2001) The monsoon currents in the north Indian Ocean. *Elsevier*
5. NASA (2011) Flat Map Ocean Current Flows with Sea Surface Temperatures (SST). *NASA/Goddard Space Flight Center Scientific Visualization Studio.* http://svs.gsfc.nasa.gov/goto?3821.
6. Lopez, Joseph, and Lakshmi Kantha (2000) "A Data-Assimilative Numerical Model of the Northern Indian Ocean." *American Meteorological Society.*
7. Aneesh, C.S. (2006) "Data Assimilation Experiments using an Indian Ocean General Circulation Model." *World Scientific*
8. Kurian, J., and P. N. Vinayachandran (20070 "Mechanisms of formation of the Arabian Sea mini warm pool in a high resolution *Ocean General Circulation Model.*" J. Geophys. Res. doi:10.1029/2006JC003631
9. Kawamiya, Michio, and Andreas Oschlies. 2003. "An eddy-permitting, coupled ecosystem-circulation model of the Arabian Sea: comparison with observations." *Journal of Marine Systems* 38: 221-257.
10. L'Hégaret. 2015. "Mesoscale variability in the Arabian Sea from HYCOM model results and observations: impact on the Persian Gulf Water path." *Ocean Sci. Discuss.*
11. Argo data management (2013) "Argo user's manual." (Ifremer). doi:10.13155/26387.
12. U.S. Navy HYCOM (2015) Real-time 1/12° Global HYCOM Nowcast/Forecast System. Prod. HYCOM Consortium for Data-Assimilative Ocean Modeling. *Naval Research Laboratory*. http://www7320.nrlssc.navy.mil/GLBhycom1-12/skill.html.
13. Tartinville, B., E. Deleersnijder, P. Lazure, R. Proctor, K. Ruddick and R. Uittenbogaard. (1998) A coastal ocean model intercomparison study for a three-dimensional idealized test case, *Applied Mathematical Modelling,* pp. 165-182.
14. CMCC (2014). The CMCC Global Ocean Physical Reanalysis System *C-GLORS.*
15. Ghader, S., D. Yazgi, S.A. Haghshenas, A. Razavi Arab, M. Jedari Attari, A. Bakhtiari and H. Zinsazboroujerdi (2016). Hindcasting tropical storm events in the Oman sea. *Journal of Coastal Research.* 75. 1087-1091.

16. CCAR (2013) Reconstructed Sea Level Version 1. *Prod. Boulder University of Colorado.* http://podaac.jpl.nasa.gov/dataset/RECON_SEA_LEVEL_OST_L4_V1.
17. Amante, & Eakins. (2009). ETOPO1 1 Arc-Minute Global Relief Model: Procedures, Data Sources and Analysis. *NOAA Technical Memorandum* NESDIS NGDC 24. National Geophysical Data Center, NOAA. doi:10.7289/V5C8276M
18. ERDDAP (2017) Easier access to scientific data, https://coastwatch.pfeg.noaa.gov/erddap/index.html
19. Savtchenko (2004) An assessment of the Indian Ocean, Monsoon, and Somali Current using NASA's AIRS, MODIS, and QuikSCAT data, http://disc.sci.gsfc.nasa.gov/

Journal of Hydraulic Structures
***J. Hydraul. Struct.*, 2018; 4(1): 55-74**
DOI: 10.22055/JHS.2018.25552.1071



OPEN ACCESS

Study of Streamlines under the Influence of Displacement of Submerged Vanes in Channel Width, and at the Upstream Area of a Cylindrical Bridge Pier in a 180 Degree Sharp Bend

Chonoor Abdi Chooplou[1]
Mohammad Vaghefi[2]
Seyyed Hamed Meraji[3]

Abstract

In this paper, submerged vanes were placed at the upstream area of a bridge pier located at the 90 degree angle. Then, using the laboratory equipment, a study of flow pattern was conducted throughout the bend, specifically around the pier and submerged vanes. ADV velocimeter was incorporated in order to help measure 3D velocity components. Submerged vanes were installed at distances of 40 and 60% of the channel width from the inner bank at the upstream area of the bridge; while the distance between the vanes and the pier (5 times the pier diameter) and the distance between the vanes themselves (3 times the pier diameter) were held constant during the experiments. The results demonstrated that moving the submerged vanes towards the outer bank created a vortex at a distance of 5 times the pier diameter from the center of the pier in upstream direction at a distance of 33% of the channel width from the inner bank at a height of 6.9 cm, equal to 30 times the flow depth from the bed.

Keywords: Flow Pattern, Bridge Pier, Submerged Vanes, Velocity Contours, 180 Degree Sharp Bend

Received: 17 April 2018; Accepted: 27 May 2018

1. Introduction

Flow pattern around bridge piers is highly complicated, and such complexity is intensified due to formation of scour holes around the pier. Development of this hole around the piers results in depletion underneath the foundations, thus destruction of the bridge. Collision of the

[1] M.Sc. Student of Hydraulic Structures, Civil Engineering Department, Persian Gulf University, Bushehr, Iran. *chonoorabdi@yahoo.com*
[2] Associate Professor of Hydraulic Structures, Civil Engineering Department, Persian Gulf University, Bushehr, Iran. *vaghefi@pgu.ac.ir* (**Corresponding Author**)
[3] Assistant Professor of Hydraulic Structures, Civil Engineering Department, Persian Gulf University, Bushehr, Iran. *H.meraji@pgu.ac.ir*

CC BY

flow with the pier forms a horseshoe vortex, and separation of the flow from the pier entails formation of vortices called rising vortices.

This paper has attempted to investigate a 10% displacement of submerged vanes in channel width in proportion to the central line of the channel at the upstream side of the bridge pier, and its effect on flow pattern around the cylindrical bridge pier located at the 180 degree sharp bend apex. Among research efforts carried out to this aim, the following can be mentioned: Ye et al. [1] examined velocity distribution in an organized bend with a trapezoidal section. Considering the properties of their physical model, they concluded that the maximum velocity occurred by the inlet inner wall, then the velocity distribution at depth inclined towards steadiness, and the maximum velocity moved towards the external bend at the 60 degree angle. Marelius and Sinha [2] determined the optimum angle for flow collision with the plane, and carried out a numerical and experimental analysis of flow pattern around a plane in a straight path with mobile bed. Johnson et al. [3] conducted experiments, and investigated the role of submerged vanes in prevention of scour at the marginal bridge piers through an experimental model. They observed that such vanes resulted in augmentation of flow velocity at the center of the channel, and a drop in flow velocity and shear stress at the bank. Blanckaert and Graf [4] conducted an investigation of flow parameters including velocities on an erodible bed in three directions in a bended flume as wide as 0.4 m, with a central angle of 120 degrees, and an average curvature radius of 2 m. Their results indicated that the amount of turbulence shear stresses of $\rho\overline{u'w'}$and $\rho\overline{u'v'}$ in the vicinity of the outer bank was smaller than that in a straight channel. They also demonstrated that the turbulence shear stress of $\rho\overline{v'w'}$ denoted circulation of the cross sectional cells. Soon-Keat et al [5] examined the flow pattern around a long plane in wide rivers with mobile bed. Rodergruez and Garcia [6] employed an acoustic velocimeter, and investigated the secondary flow, flow turbulence characteristics, and flow transverse variations in a straight channel. Blecher and Fox [7] used a PIV device and examined the effect of roughness on turbulence flow variations with regards to large-scale structures. In addition to velocity constriction depth, they observed the presence of a middle zone near the center of the channel. Naji Abhari et al. [8] analyzed variations in velocity components, streamlines, bed shear stress, and the secondary flow in a channel with a 90 degree bend. Their study indicated that local asymmetry of velocity components in the bended channel is a result of the secondary flow. Kumar et al. [9] investigated flow pattern around a bridge pier with a collar under mobile bed conditions and reported their observation of the effect of the collar on horseshoe vortices around the pier and its effect on scouring. Ataie et al. [10] studied the flow pattern around vertical, paired cylindrical piers in a straight channel. They conducted the experiment under mobile bed and rigid bed conditions. Their research indicated that velocity and shear stress in the zone between the pier intensified, and the pier affected horseshoe vortices in a longer range. Das et al. [11] studied flow pattern in a laboratory flume by using ADV. The pier employed in their experiment was paired and installed on vanes parallel to the flow. They calculated flow hydraulic parameters, and then depicted the generated horseshoe vortices by drawing the streamlines. Tang and Knight [12] investigated flow pattern and scour around a bridge pier by using CFD modeling, and then analyzed their observations by computing parameters such as bed shear stress and streamlines. Vaghefi et al. [13] conducted experiments in a 1-meter-wide laboratory flume with a 180 degree sharp bend and a central curvature radius of 2, and studied velocity fluctuations, and then the distribution of kinetic energy turbulence by using ADV velocimeter. The results of their study indicated that the maximum kinetic energy turbulence occurred at the 85 degree section, and the minimum at the 20 degree section. Also, the maximum longitudinal and transverse velocity fluctuations occurred at the 70 degree section near the inner wall. Vaghefi et al. [14] examined

flow pattern and shear stress calculation in a 180 degree sharp bend by using ADV in an experimental study. Haji Azizi et al. [15] carried out a numerical investigation of the flow around a bridge pier in the vicinity of submerged vanes by using fluent software program. Their work concluded a desirable correspondence between experimental and numerical results. Ben Mohammad Khajeh et al. [16] experimentally studied the effect of inclination of a cylindrical bridge pier installed at the apex of a 180 degree sharp bend on scour pattern. Their work demonstrated that the maximum and minimum scouring occurred in the scour hole around the pier in the case of inclination towards the outer and the inner banks respectively equal to 1.05 and 0.70 times the flow depth at the upstream straight path. Karimi et al. [17] investigated the effect of inclination angle of the bridge pier on scour process. To this aim, cylindrical piers of four different inclination angles were placed in a straight channel, and the experiments were conducted at four different flow rates under clear water conditions. The results of their study reported the minimum and maximum scour depths to have occurred from the 0 to 15 degree angles of the pier. Dee et al. (2017) studied bank erosion and protection by using a submerged vane placed at an optimum angle in a 180 degree laboratory channel bend. As is observed, a great number of studies have so far been carried out on empty bends, as well as on bridge piers in straight paths; however, the effect of submerged vanes on scour pattern around the bridge pier and the flow pattern around the pier in the bend has not been investigated. The present study experimentally examines the effect of a 10% displacement of submerged vanes through the channel width in proportion to the central line of the channel at the upstream area on the pattern of flow and scour around a cylindrical bridge pier located at the apex of a 180 degree sharp bend along by measuring 3D velocity.

2. Materials and Methods

The experiments have been conducted in a bended channel with a rectangular section, with a ratio of central line curvature radius to channel width (R/B) equal to 2 and a rectangular section with a 180 degree central angle in the advanced laboratory of hydraulic structures in Persian Gulf University. Width and height of the channel are respectively 100 and 70 cm. The upstream and downstream straight ends of the flume are respectively 6.5 and 5 meters long.

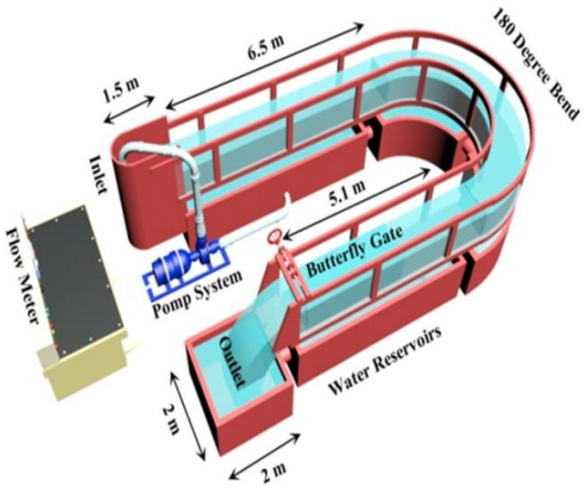


Figure 1. A view of the laboratory flume (Vaghefi et al. 2016)

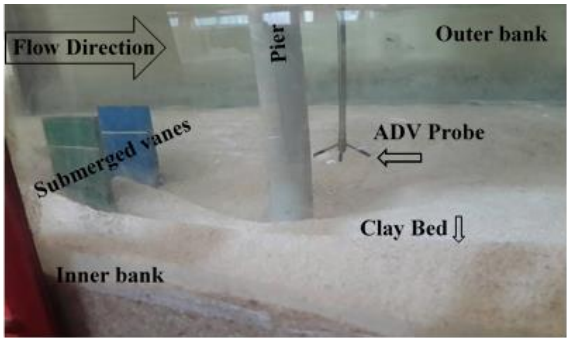
Figure (1) presents a view of the laboratory flume. The bed is covered with grained sediments

with an average diameter of 1.5mm, and 1.14 mm standard deviation as deep as 30 cm. The inlet discharge is 70 liters, which is held constant during the experiment. The water level is also constant, equal to 18 cm (y) at the upstream straight path before entering the bend. This is set by the butterfly valve at the end of the downstream straight path.

The scour experiments were conducted under clear water and incipient motion conditions. The Froude number is 0.29, and the Reynolds number is approximately 51480 during the experiments. In scour experiments, a laser distance meter was used for recording and consolidating the bed.

In flow pattern experiments, an air compressor and then a fiberglass paste were used for freezing and consolidating the bed. Calculation of each of these factors requires possession of velocity values at different points of the flow zone under study. Hence, the flow meshing in this work was assumed from 0 to 180 degree sections of the bend with 50 points at 1.5 degree intervals in length, and 50 points at approximately 2 cm intervals in width. The height of the mesh was collected at 10 points in height, including 2, 4, 6, and 8 cm beneath the base level, and 1, 3, 6, and 10 cm above the base level. Finally, the measurement was conducted at 4 and 1 cm distances from the water surface by using a side-looking velocity probe. Vectrino 3D velocimeter was employed to measure velocity components.

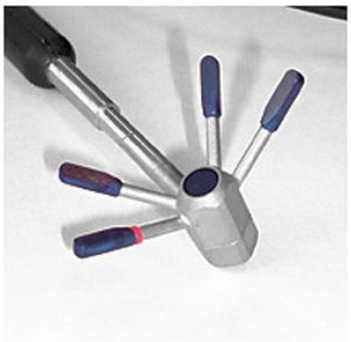
Figure (2) depicts the position of the velocimeter in the 180 degree bend with its two different probes. Two experiments were carried out by installing submerged vanes at a distance of 5 times the pier diameter, at two positions of 40 (PFV) and 60% of the channel width from the inner bank (PSV). The mentioned submerged vanes are rectangular, made of plexiglass, 1 cm thick, and 7.5 cm long, placed at the 25 degree horizontal angle. The bridge pier is made of PVC as thick as 5 cm, placed at the 90 degree position to the beginning of the bend.



(a)



(b)



(c)

Figure 2. a) the position of Vectrino velocimeter in the 180 degree sharp bend, and a view of b)

down-looking, and c) side-looking probes

3. Results and Observations

Figures (3) through (6) provide drawings of streamlines at different cross sections in PFV and PSV experiments. Along the channel, where the effect of the longitudinal pressure gradient is reduced, the centrifugal force governs the field, and the secondary flow is observed as a single circular cell at the cross section, which is known as the main secondary flow or the primary secondary flow.

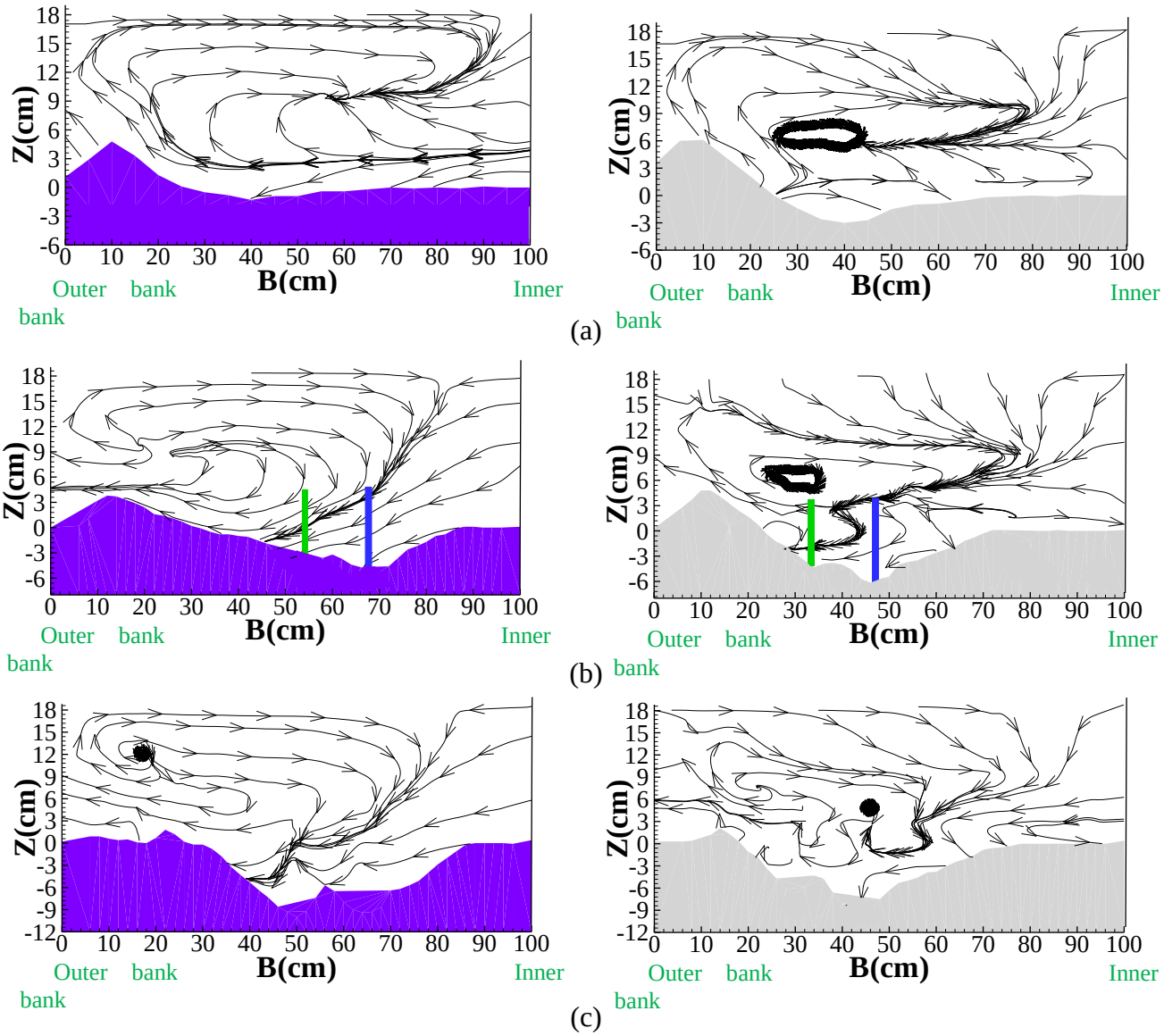


Figure 3. A view of the flow pattern in a) 75, b) 81.5, and c) 814.5 degree cross sections of the bend. (PFV experiment on the right, and PSV experiment on the left)

Figure (3) shows the flow pattern at the upstream area of submerged vanes at the location of the vanes in the experiments. It can be observed that the streamlines show the secondary flow in both experiments at the 75 degree angle, equal to 10 times the pier diameter in upstream direction (Figure (3-a)).

By advancing through the bend in downstream direction and approaching the submerged vanes, the effect of submerged vanes on flow begins to be manifested, so that in both experiments, flow separation in upstream direction occurs at the 81.5 degree angle at a distance equal to 7 times the pier diameter. As is observed, with increase in the distance between submerged vanes and the inner bank, the vortices gradually shrink, which is the cause of reduction in scour at this section ((Figure (3-b)). Figure (3-c) shows the cross section in the 84.5 degree position.

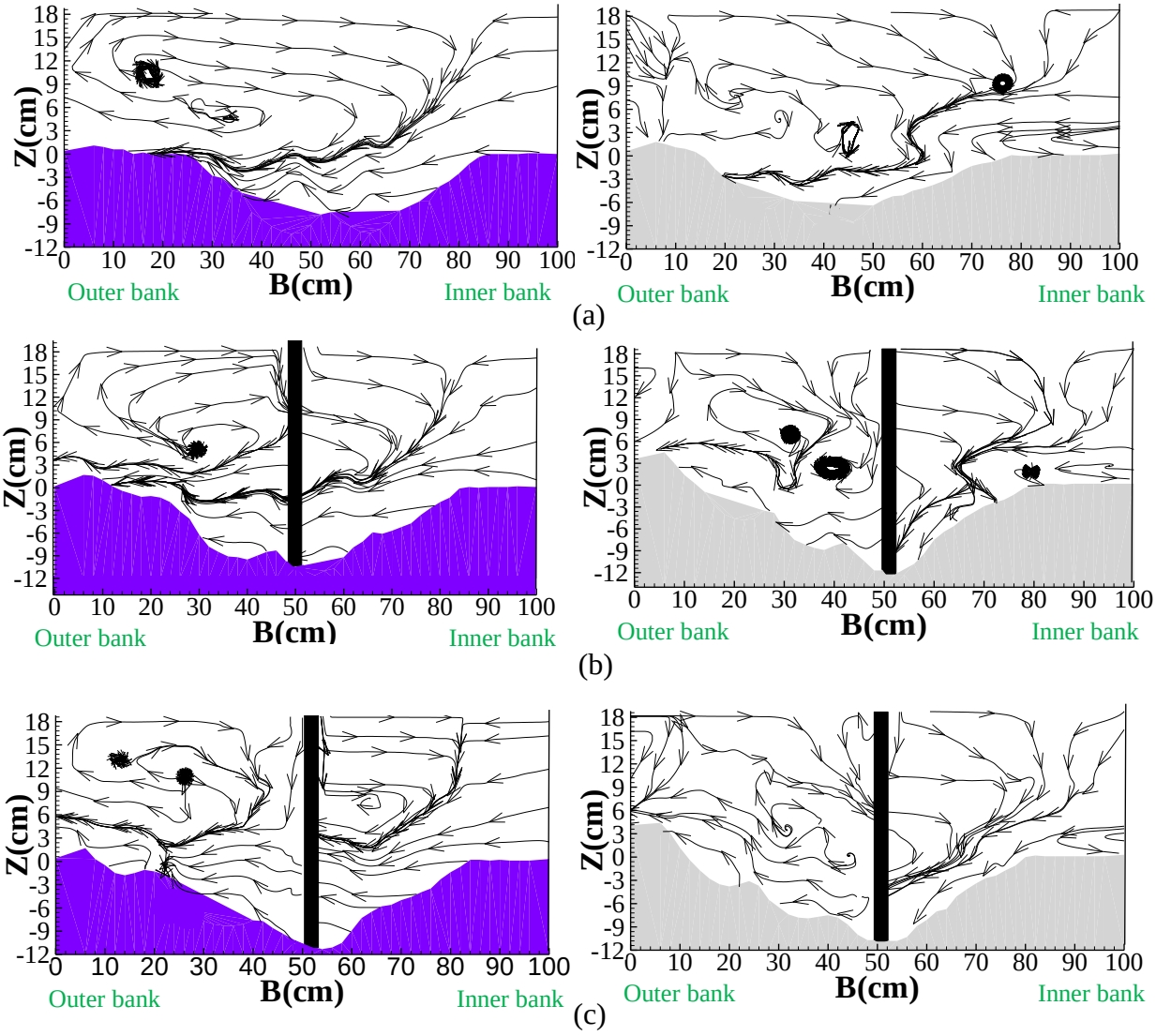


Figure 4. A view of the flow pattern at a) 86, b) 89, and c) 90.5 degree cross sections in the bend. (PFV experiment on the right, and PSV experiment on the left)

According to the figure, it can be observed that when the submerged vanes are located at a distance of 40% of the channel width from the inner bank, the central vortex is inclined towards the outer bank, because the presence of sediment piles at the inner bank at this section, reduction of pressure gradient near the bed, and occurrence of the maximum kinetic energy near the outer bank incline the transverse flow towards the outer bank.

Figure (4) presents cross sections at the area around the pier. With a 10% displacement of submerged vanes in proportion to the central line of the channel, the inclination of the vortex towards the inner bank increases by 64% (Figure (4-a)). Generally, at the area around the pier, the flow pattern undergoes changes due to collision with the pier. Hence, the collision of the streamlines with bed surface increases.

This generates a flow upwards in the direction of the inner bank. In PFV experiment in Figure (4-b), the main secondary flow in the inner bend is observed as two vortices in two zones. The first zone represents 31% of the channel width from the inner bank and 7% of the flow depth from the bed, and the second zone represents 39% of the channel width from the inner bank and 3% of the flow depth from the bed. In PSV experiment, this is formed at a distance of 30% of the channel width from the inner bank at a depth of 5% of the flow depth from the bed. As is seen in Figure (4-c), the streamlines in the vicinity of the inner bank of the pier towards the channel bed push scour and bed materials out of the hole.

Figure (5) depicts the flow pattern at the cross sections at the downstream area of the pier location. The flow at the downstream area of the pier returns to the state before collision with the pier. Away from the pier area in downstream direction, turbulence resulting from the presence of the pier and submerged vanes gradually fades.

As is evident, due to presence of the secondary flows near the inner bank, a sediment pile is created, which is shown in Figure (5-a). There are two vortices in the middle and the inner bank in addition to the central vortex. Further ahead, it can be observed that the effect of the vortex at the inner bank is reduced, while the central vortex grows. Therefore, as seen in Figure (5-b), in PFV case, the vortex is transported towards the level closer to the bed, and in PSV case, the two vortices in the vicinity of the inner bank fade, and only one vortex remains at a distance of 66% of the channel width from the inner bank at a height of 7% of the flow depth from the bend. At the 96 degree angle from the beginning of the bend, equal to 4 times the pier diameter towards the downstream side of the center of the pier location, it can be observed that with a 10% displacement of the vanes in proportion to the central line of the channel, the flow separation boundary appears at a height of 9.3 cm, equal to 51% of the flow depth from the bed at a distance of 0 to 37% of the channel width from the outer bank, the fact which results in less sedimentation at the inner bank (Figure (5-c)).

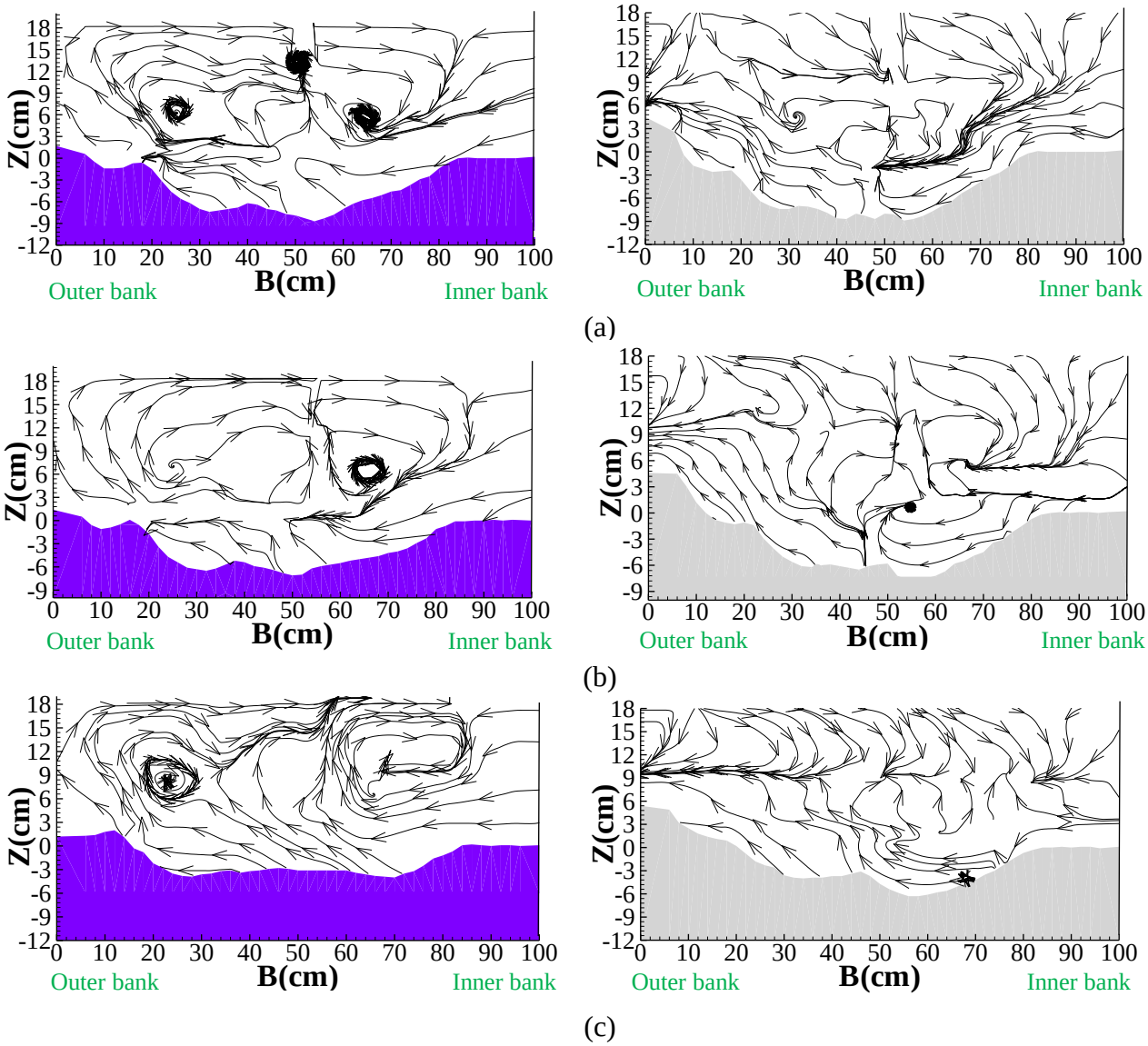


Figure 5. A view of the flow pattern at the a) 92, b) 93.5, and c) 96 degree cross sections of the bend. (PFV experiment on the right, and PSV experiment on the left)

Figure (6) represents cross sections at the end of the bend. In PFV case, such turbulence and vortices are still observed at a distance of 10 times the pier diameter in downstream direction (at the 100 degree angle from the beginning of the bend) in Figure (6-a). Whereas, in PSV experiment, turbulence occurs all the way to the end of the bend; thus, a small vortex is formed at the 140 degree angle in the middle of the channel (Figure (6-b)). As in Figure (6-c), in PSV experiment, the center of the main secondary flow occurs at a distance of 0 to 40% of the channel width from the inner bank at a height of 80% of the flow depth from the bed.

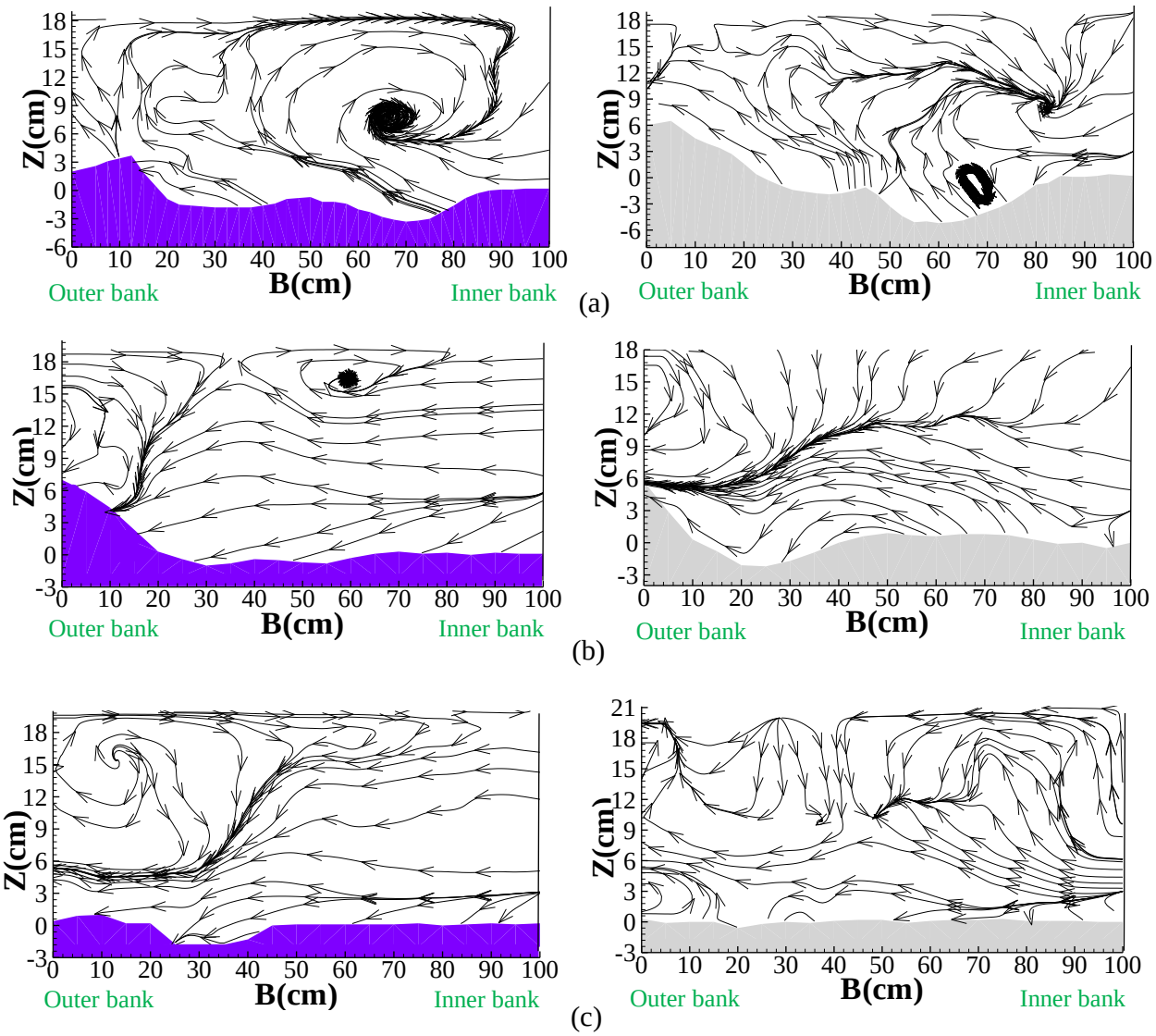


Figure 6. A view of the flow pattern at the a) 100, b) and c) 160 degree cross sections of the bend. (PFV experiment on the right, and PSV experiment on the left)

An instance of flow pattern in longitudinal sections near the inner bank in mid-channel is drawn in Figure (7). Since longitudinal sections are a result of vertical and tangential velocities, and the tangential velocity is greater than vertical velocity, the streamlines near the banks at the sections are almost parallel, with a large distance from the pier. Figure (7-a) and Figure (7-b) demonstrate longitudinal sections at the area of the central line of the bend and the inner bank. As is observed in Figure (7-b), the flow pattern in both experiments has changed under the influence of the pier, and a return flow is generated near the water surface at the downstream side of the pier, which is due to the effect of down flow after collision with the pier. Such a flow continues after collision with the pier, following a path parallel with the formed longitudinal streamlines. Such variations have occurred from the middle up to the surface of the flow, while

there is no trace of them at the levels beneath.

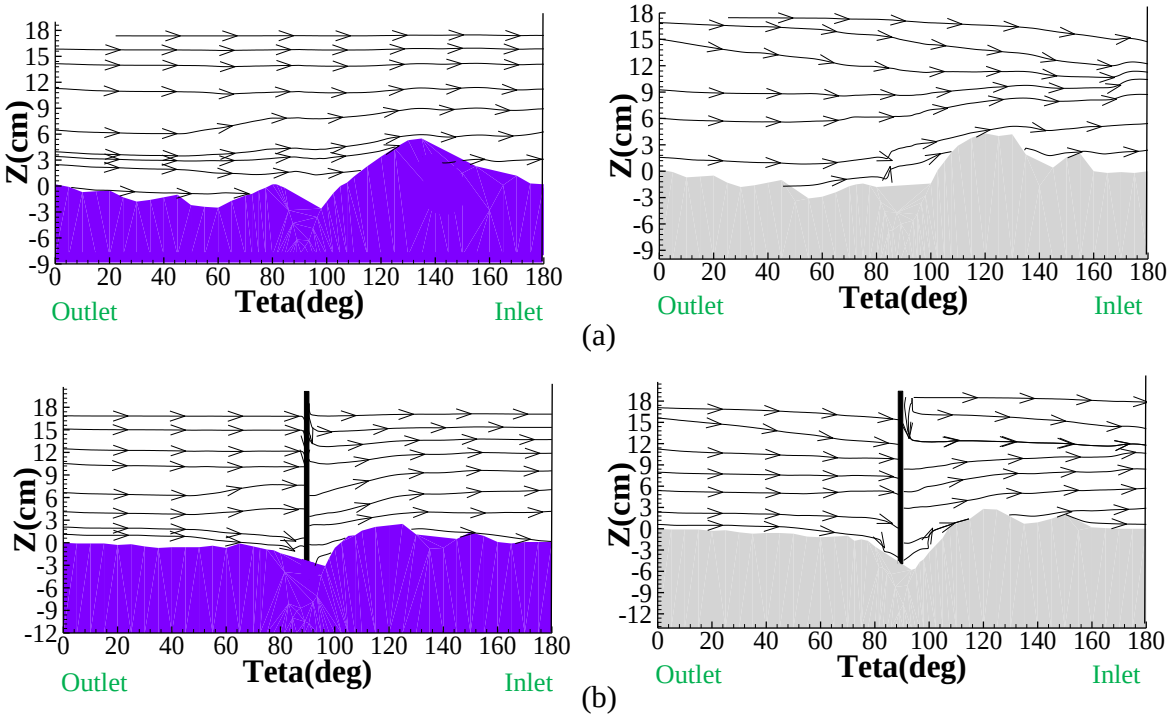


Figure 7. A view of the flow pattern at different longitudinal sections of the 180 degree bend, at a distance of a) 30, and b) 50% of the channel width from the inner bank. (PFV experiment on the right, and PSV experiment on the left)

Figure (8) shows the path where the maximum velocity occurs at levels equal to 55.5% of the flow depth from the bed and 5% of the flow depth from water surface in PFV and PSV experiments. The maximum resultant velocity is obtained through the following relation:

$$V_R = \sqrt{{V_r}^2 + {U_\theta}^2 + {W_z}^2} \quad \textbf{(1)}$$

In the relation above, V_r, U_θ, and W_z respectively denote radial, tangential, and vertical velocity components. The common feature of all the figures lies at the entrance of the bend, where the path to occurrence of the maximum resultant velocity is extended from the bend entrance towards the inner bank. This is due to the fact that due to entrance of the flow into the bend, and because of the pressure gradient resulting from the centripetal force, the maximum velocity occurs at the beginning sections towards the inner bank and accelerates water particles.

This is so while it is accompanied by a positive longitudinal gradient at the outer bank, and the velocity of the fluid is reduced in this area. The maximum velocity lasts up to the 55 degree section, and then it is gradually inclined towards the outer wall. Near the bed in PFV experiment, the path to the maximum velocity falls at the 89 degree angle near the inner bank, and then it is inclined towards the outer bank afterwards.

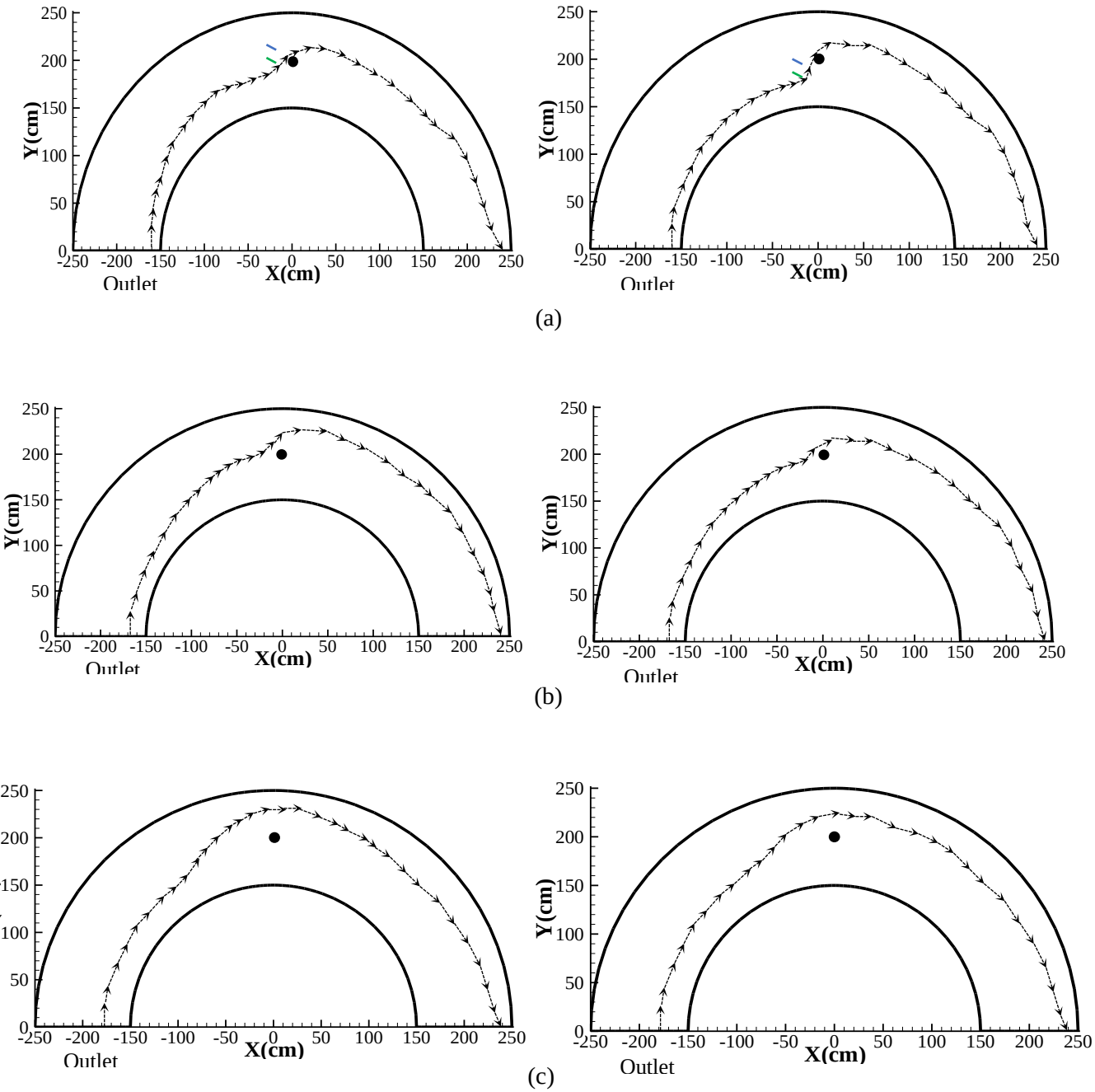


Figure 8. The path to formation of the maximum resultant velocity at the levels equal to a) 5, and b) 55% of the flow depth from the bed, and c) 5% of the flow depth from water surface (PFV experiment on the right, and PSV experiment on the left)

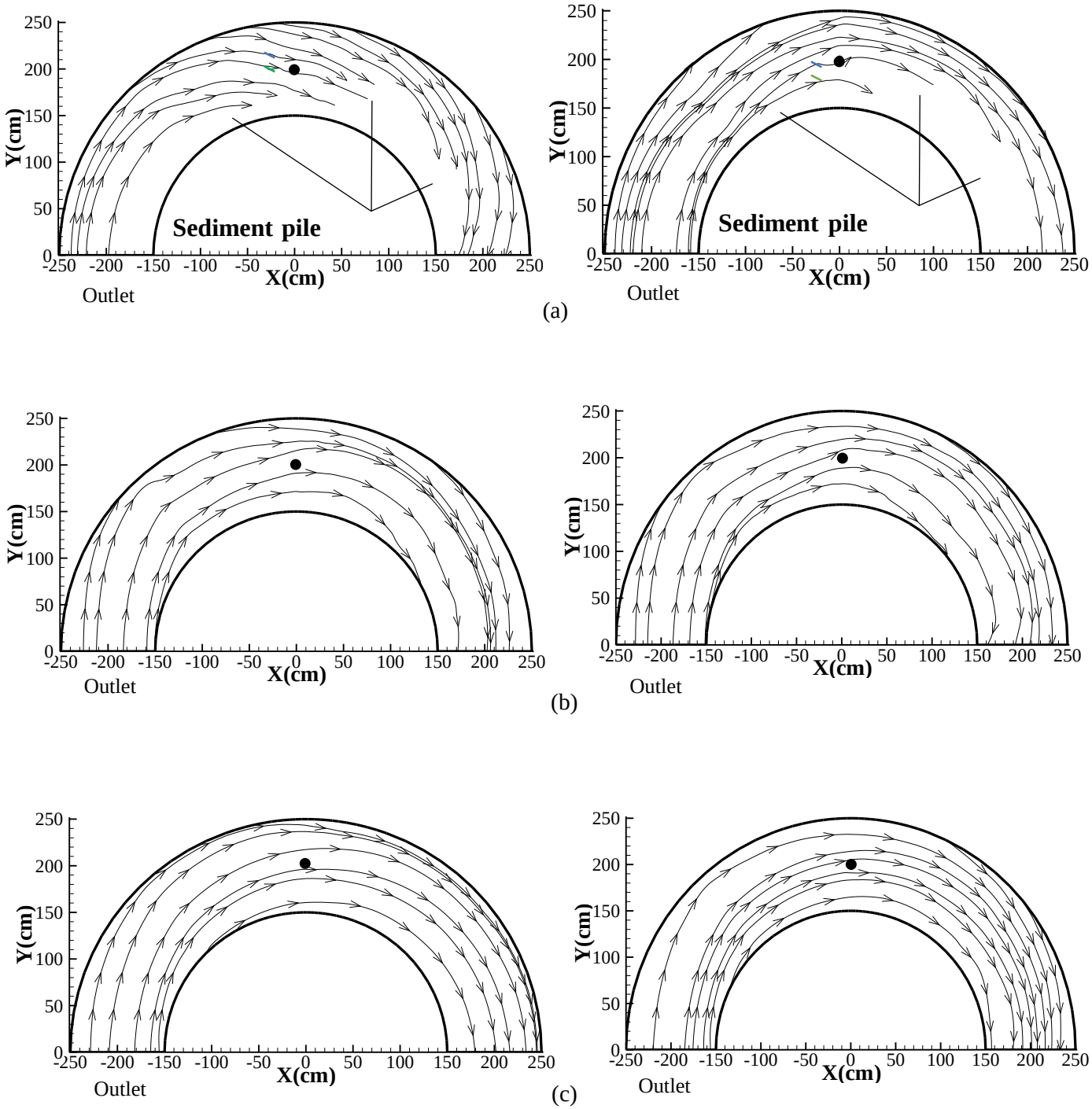


Figure 9. The diagram on velocity lines at levels equal to a) 5, and b) 55% of the flow depth at the beginning of the bend from the bed, and c) 5% of the flow depth at the beginning of the bend from the flow surface. (PFV experiment on the right, and PSV experiment on the left)

Whereas, when the submerged vanes are placed at a distance of 60% of the channel width from the inner bank, the maximum velocity covers a smaller distance in the vicinity of the inner bank, so that it is inclined towards the outer bank at the 86 degree angle. In fact, by transporting the submerged vanes to the area near the outer bank, the streamlines fall at a distance equal to 2 times the pier diameter at the outer bank (Figure (8-a)). The maximum velocity at the level of 55% of the flow depth from the bed in PFV and PSV experiments respectively occurs up to approximately 84.5 and 78.5 degree sections from the beginning of the bend in the vicinity of the inner bank. At the downstream sections, it inclines towards the outer wall of the channel (Figure (8-b)). Approaching the water surface, the maximum velocity line follows a milder path than that at 5% of the flow depth from the bed. Also, at 5% of the flow depth from the bed, due to augmentation of the transverse flow strength, the maximum flow velocity inclines towards the outer bank to the end of the bend after crossing the central line of the bend. The resultant velocity path falls near the pier, so that it crosses a distance of 40% of the channel width from the inner bank in PFV, and 50% in PSV (Figure (8-c)). At all the three levels, and all the experiments, the maximum velocity lines occur at the end of the bend (the 180 degree angle) at a distance of 95% of the channel width from the inner bank. The streamlines are presented in Figure (9) at levels equal to 5 and 55% of the flow depth at the beginning of the bend from the bed, and 5% of the flow depth at the beginning of the bend from the flow surface in PFV and PSV experiments. As it is observed, the path streamlines take at a level equal to 5% of the flow depth from the bed is inclined towards the inner bank, so that the stream lines in the case of placing the submerged vanes at a distance of 60% of channel width from the inner bank incline further towards the inner bank. The streamlines incline towards the inner bank upon approaching the location of the vanes and bridge pier, and cause formation of the sediment pile at this area. Thus, the maximum sedimentation occurs at the 120 degree angle in PFV, and at the 130 degree angle in PFV experiments (Figure (9-a)). At the level equal to 55% of the flow depth from the bed, the inclination of the streamlines towards the inner bank is reduced, and, as is observed, the lines are almost parallel to the central line of the channel (Figure (9-b)). Approaching the flow surface, at a distance equal to 5% of flow depth from the water surface, the average deviation of the streamlines towards the outer bank is observed, the reason of which is the centrifugal force overcoming the other forces on the surface of the flow. And since the mentioned vanes are submerged, there is no obstacle against the flow at the water surface, the upstream flows do not overcome the mainstream, no vortex is formed on water surface, and little difference is observed in streamlines between two installation cases of the submerged vanes (Figure (9-c)).

The streamlines at levels equal to 20 and 30% of the flow depth at the beginning of the bend, lower than the base level, are presented in Figure (10). In this figure, due to presence of sediments around the scour hole at all points, no streamlines exist (white areas of levels higher than those of 20 and 30% of the flow depth at the beginning of the bend are lower than the bed). Little return flow is observed at the downstream side of the pier, and the flow is directed towards the inner bank. This is due to deviation of the flow because of submerged vanes, the pier, and the flow present at the bend. The same flow pushes the sediments out of the scour hole towards the inner bank.

A comparison between Figure (9) and (10) indicates that the horizontal angle of the streamlines at levels lower than the bed in Figure (10) is larger than that in Figure (9). It can be observed in the figure that no vortex is formed due to the fact that the flow pours down into the scour hole.

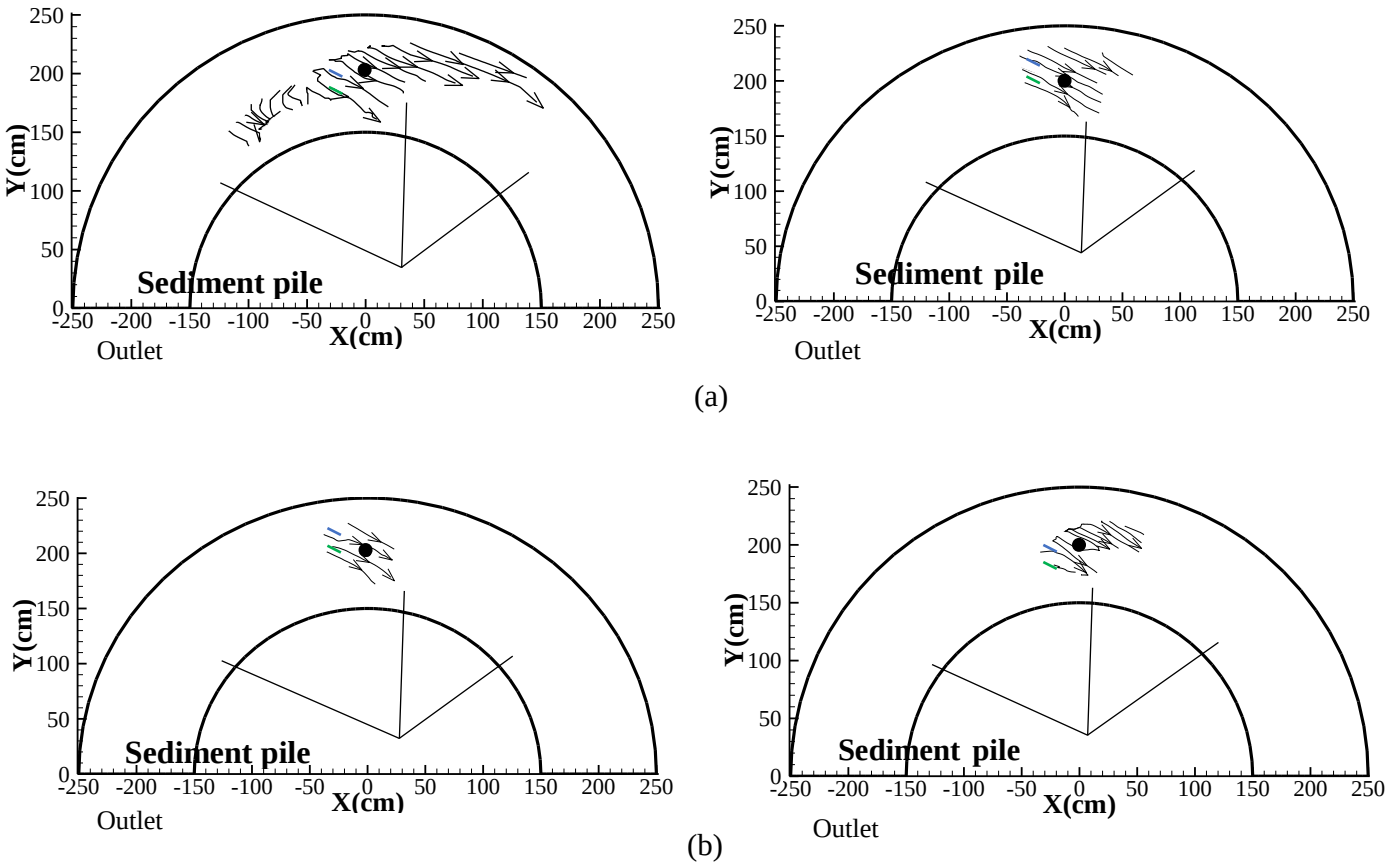


Figure 10. The diagram on streamlines at levels equal to a) 20, and b) 30% of the flow depth at the beginning of the bend, lower than the bed. (PFV experiment on the right, and PSV experiment on the left)

Figure (11) presents the tangential velocity contour at plan sections at the level of 5 and 95% of the flow depth at the beginning of the bend from the bed. As in Figure (11-a), the maximum positive tangential velocity in PFV experiment occurs at a distance of 85% and the position of 28 times the pier diameter in the direction of the downstream area of the pier location. Also, in PFV experiment, it occurs at a distance of 58% of the channel width from the inner bank and the position of 3 times the pier diameter in the direction of the downstream area of the pier location. Further, the maximum negative tangential velocities occur at distances of 6 and 20% of the channel width respectively, and the maximum positive tangential velocity in PFV experiment is 8.5% higher than that in PSV experiment. It is observed at the beginning of the bend that the maximum tangential velocity occurs in the vicinity of the inner bank at the water surface, the fact which is due to augmentation of pressure gradient near the inner bank. In general, the maximum tangential velocity distances away from the inner bank, and due to section constriction and higher longitudinal pressure gradient at the surface, the maximum tangential velocity is generated around the pier. Also, by distancing away from the pier in downstream direction, the maximum tangential velocity at the second half of the bend is created near the inner and outer banks. It can be observed that with increase in the distance between the submerged vanes and the

inner bank at this section, the maximum positive tangential velocity increases by 14% (Figure (11-b)).

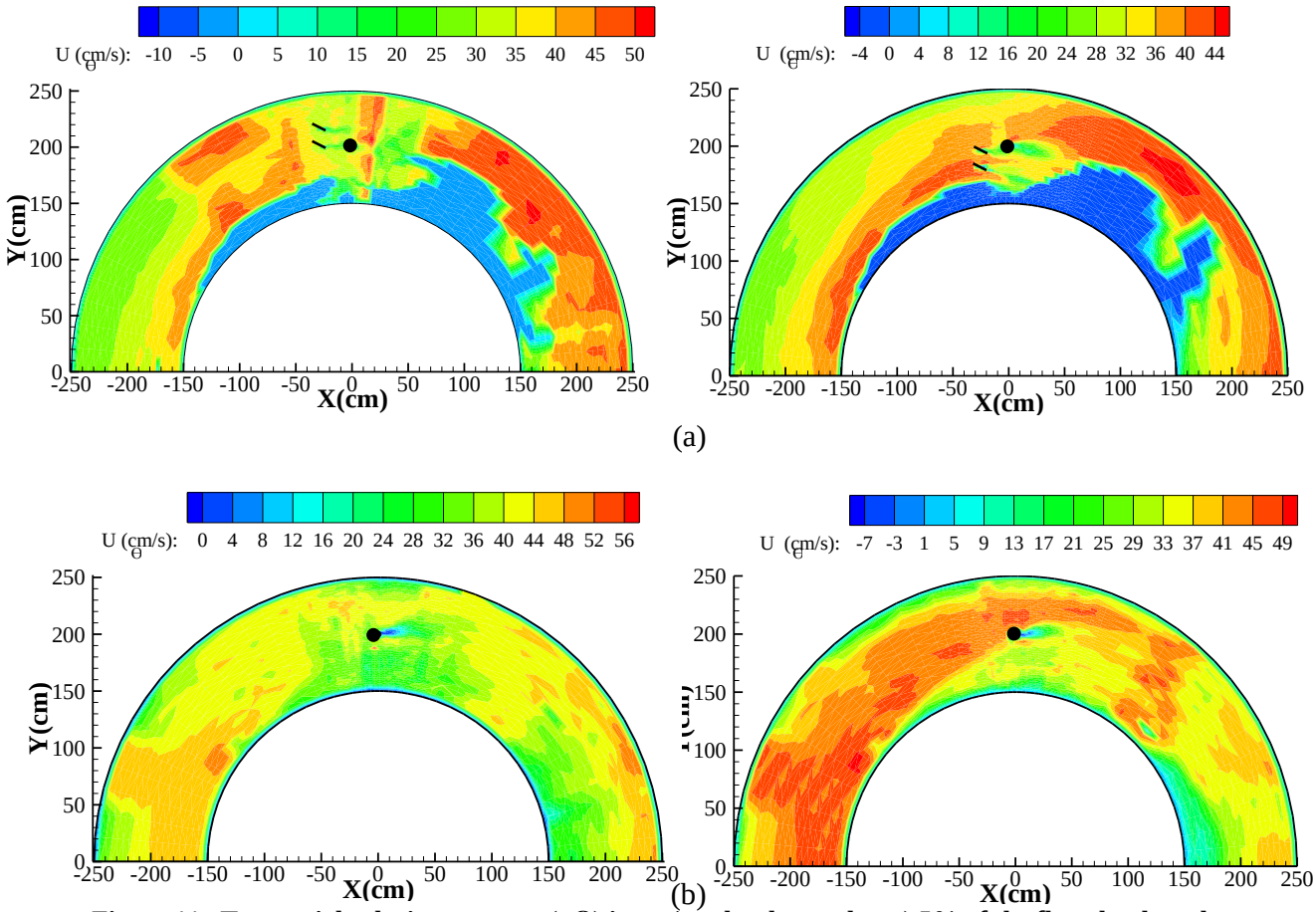


Figure 11. Tangential velocity contours (uΘ) in cm/s at levels equal to a) 5% of the flow depth at the beginning of the bend from the bed, and b) 5% of the flow depth at the beginning of the bend from the water surface (PFV experiment on the right, and PSV experiment on the left)

The radial velocity contour at plan sections at levels of 5 and 95% of the flow depth at the beginning of the bend from the bed is presented in Figure (12). According to Figure (12), at the plan sections, the negative values of the radial velocity (towards the inner bank) can be noted. Creation of obstacles on the path of the flow generates negative pressure gradient at the downstream area of the obstacle. Due to employment of submerged vanes at the upstream area of the pier located at the vane perpendicular to the flow, the fluid particles enter the zone of negative pressure gradient after collision with submerged vanes. After collision with the bridge pier, a change is observed in the process of water particle movement. In other words, a high pressure zone is created at the upstream area of submerged vanes. This leads to interference of high pressure and low pressure zones on the sides of submerged vanes, the result of which is sediment transport from the bed towards the hole around the pier and the downstream area. By increasing the distance between the submerged vanes and the inner bank, the maximum positive radial velocity at this level reduces by 7%, and the maximum negative radial velocity increases by 52%. It can be observed that in PFV experiment, the maximum positive radial velocity

(towards the outer bank) occurs at the level of 5% of the flow depth from the bed at a distance of 46% of the channel width from the inner bank, and a distance equal to 4 times the pier diameter in upstream direction. Whereas in PSV experiment, it occurs at a distance of 16% of the channel width from the inner bank at a position equal to 2 times the pier diameter in downstream direction (Figure (12-a)). As is observed in Figure (12-b), in every position of the submerged vanes at the upstream area of the pier, the flow is negative near the walls of the channel. In PSV experiment, the maximum positive radial velocity (towards the outer bank) occurs at a distance of 30% of the channel width from the inner bank, at a position equal to 41 times the pier diameter in upstream direction from the pier location.

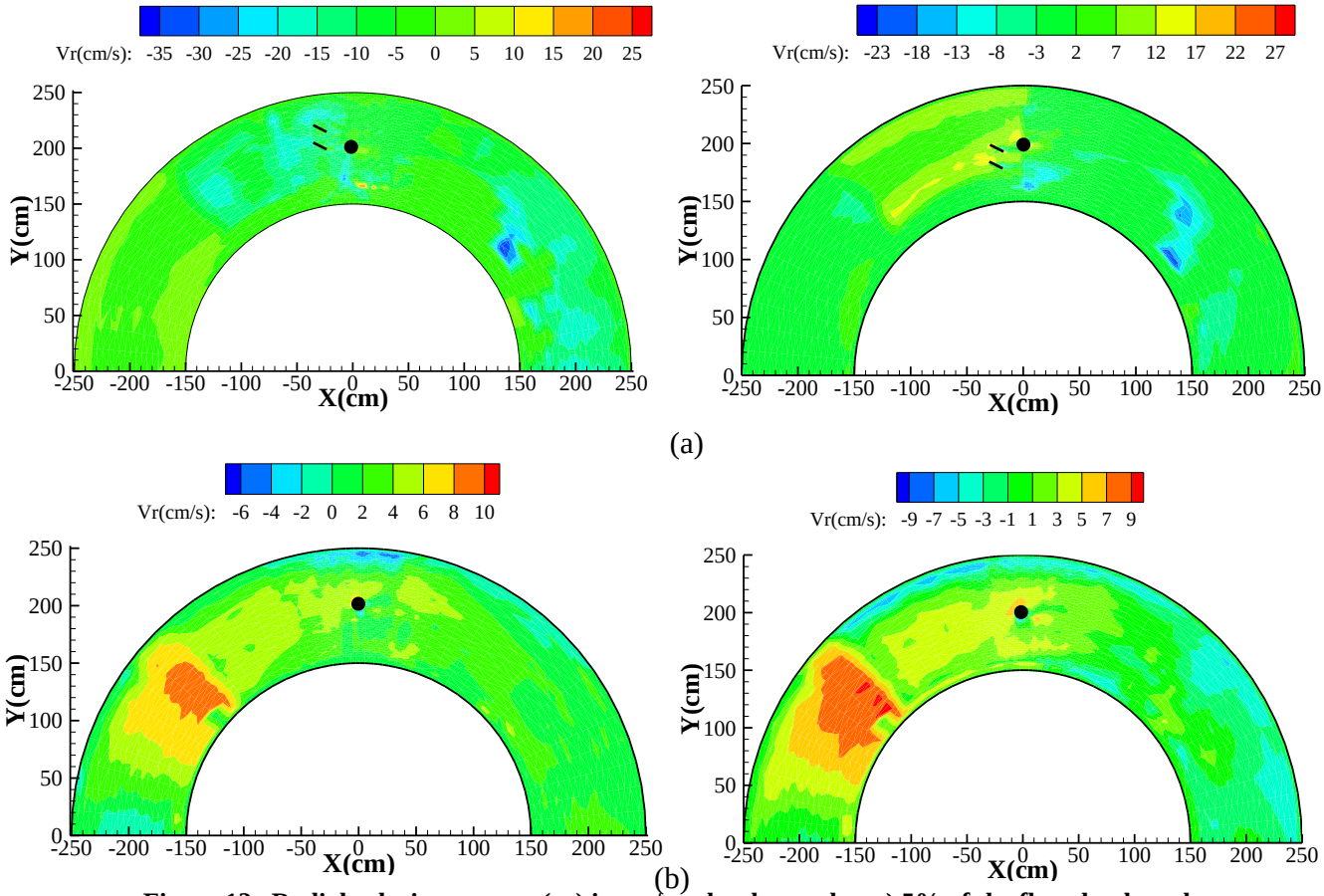


Figure 12. Radial velocity contour (vr) in cm/s at levels equal to a) 5% of the flow depth at the beginning of the bend from the bed, and b) 5% of the flow depth at the beginning of the bend from the surface (PFV experiment on the right, and PSV experiment on the left)

Figure (13) depicts an instance of vertical velocity contours in plan sections at the level near the bed and the level of 55% of the depth from the bed. As in Figure (13), before collision of the flow with the vanes and the pier, the vertical velocities are small, but at the upstream area of the pier, the vertical flow is negative, which creates a down flow leading to formation of vortices. The maximum positive (towards the water surface) and negative (towards the bed) vertical velocities at the level of 5% of the flow depth at the beginning of the bend from the bed occurs at distances of 30 and 50% of the channel width from the inner bank in PFV experiment, and 36

and 66% of the channel width from the inner bank in PSV experiment, respectively. It can be concluded that by increasing the distance between the submerged vanes and the inner bank, the range of vertical velocities at the level of 5% of the flow depth from the bed and near the bridge pier is reduced, and the area under the influence of velocity variation is further restricted (Figure (13-a)). Whereas, at the level of 55% of the flow depth at the beginning of the bend, such values occur respectively at distances of 25 and 95%, equal to 4 and -4 cm/s in PFV experiment, and at distances of 15 and 50% of the channel width from the inner bank, equal to 3.95 and -2.53 cm/s in PSV experiment (Figure (13-b)).

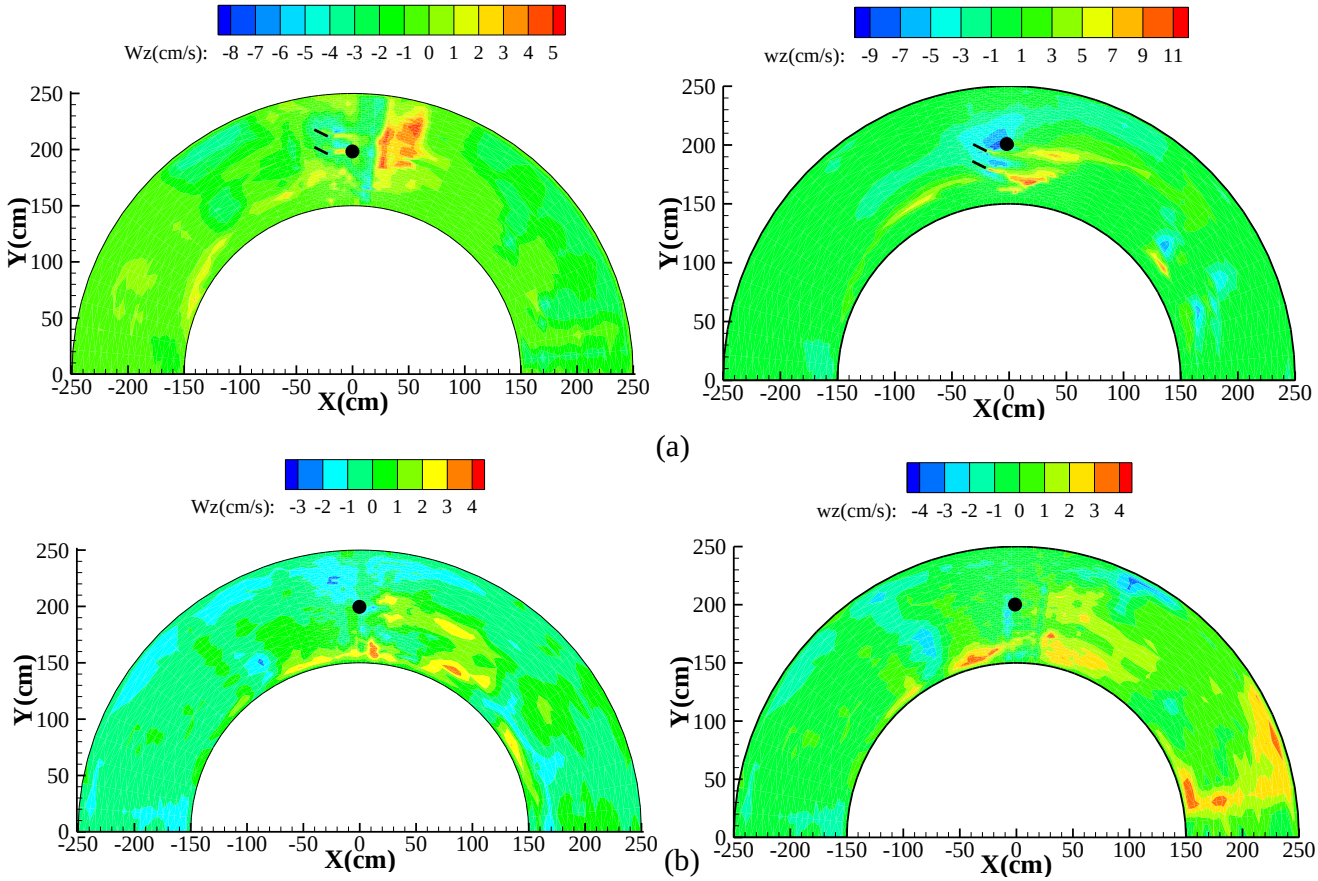


Figure 13. vertical velocity contour (WZ) in cm/s at levels equal to a) 5, and b) 55% of the flow depth at the beginning of the bend from the bed (PFV experiment on the right, and PSV experiment on the left)

4. Conclusions

In PFV experiment, the vortices are present as far as 10 times the pier diameter in downstream direction, and the changes created by the presence of submerged vanes fade upon reaching this section; while, in PSV experiment, they occur to the end of the turbulence bend. Approaching the location of submerged vanes, the streamlines incline towards the inner bank and create a sediment pile in this area, so that the maximum sedimentation occur at the 120 degree angle in PFV experiment, and at the 130 degree angle in PFV experiment. The maximum velocity at the level of 5% of the flow depth from the bed in PFV experiment occur from the proximity of the inner wall down to approximately 89 degree sections from the beginning of the

bend, and then inclines towards the outer wall of the channel at the downstream sections of the bend. The maximum velocity at the level of 5% of the flow depth from the bed in PSV experiment occurs from the vicinity of the inner wall down to approximately 86 degree sections from the beginning of the bend, and then inclines towards the outer wall of the channel at the downstream sections of the bend.

The maximum positive tangential velocity at the level of 5% of the flow depth at the beginning of the bend above the base level in PFV experiment is 8.5% higher than that in PFV experiment. In PFV experiment, it occurs at a distance of 85% and the position of 28 times the pier diameter in downstream direction from the location of the pier; whereas, in PFV experiment, it occurs at a distance of 58% of the channel width from the inner bank and the position of 3 times the pier diameter in downstream direction from the location of the pier.

By changing the position of the submerged vanes in channel width from the distance of 40% of the channel width to the distance of 60% from the inner bank, positive and negative radial velocities at the level of 10% of flow depth, lower than the bed, respectively increase by 33 and decrease by 92%.

In PFV experiment, the maximum vertical velocity occurs at a distance of 26% of the channel width from the inner bank and at a level of 20% of the flow depth at the beginning of the bend, lower than the base level. In PSV experiment, the maximum vertical velocity occurs at a distance of 50% of the channel width from the inner bank and at a level of 20% of the flow depth at the beginning of the bend, lower than the base level.

5. List of symbols

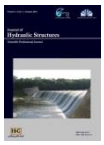
B	=	Channel width (cm)
R	=	Central Radius of the Bend (cm)
Teta	=	Angles from the beginning to the end of the bend (deg)
d_{50}	=	The Average Diameter of Sediment Particels (mm)
U	=	Flow Velocity (cm/s)
UC	=	Flow Velocity Under Incipient Motion Conditions (cm/s)
y	=	Upstream Flow Depth (cm)
D	=	Pier Diameter (cm)
L_v	=	Length of Submerged Vanes (cm)
t_v	=	Thickness of Submerged Vanes (cm)
α	=	Horizontal Angle of Submerge Vanes (deg)
L_s	=	Height of Vanes on the Bed at the initiation of the scour experiment (cm)
z	=	distance from the bed (cm)
Lvb	=	Distance of submerged vanes from the inner bank (cm)
U_θ	=	Tangential velocity (cm/s)
V_r	=	Radial velocity (cm/s)
W_z	=	Vertical velocity (cm/s)
V_R	=	The maximum resultant velocity (cm/s)

Reference

1. Ye, J. and McCorquodale, J. A. (1998). "Simulation of curved open channel flows by 3D hydrodynamic model" Journal of Hydraulic Engineering, 124(7), 687-698.
2. Marelius, F. and Sinha, S.K. (1998). "Experimental Investigation of Flow past Submerged Vanes″ Journal of Hydraulic Engineering 124(5). 542 – 545.
3. Johnson, P.A., Hey R.D., Tessier, M. and Rosgen DL. (2001). "Use of vanes for control of scour at vertical wall abutments″ Journal of Hydraulic Engineering. ASCE 127(9), 772-778.
4. Blanckaert, K. and Graf, W. H. (2001). ″Mean flow and turbulence in open-channel bend″ Journal of Hydraulic Engineering, 127(10), 835-847.
5. Soon-Keat, T., Guoliang, Y.u., Siow-Yong, L. and Muk-Chen, O. (2005). "Flow structure and sediment motion around submerged vanes in open channel" Journal of waterway, port, coastal, and ocean engineering, 131(3), 132-136.
6. Rodríguez, J. F. and M. H. García. (2008). "Laboratory measurements of 3-D flow patterns and turbulence in straight open channel with rough bed″ Journal of Hydraulic Research, 46(4), 454-465.
7. Belcher, B. J. and J. F. Fox. (2009). "Laboratory measurements of 3-D flow patterns and turbulence in straight open channel with rough bed" Journal of Hydraulic Research, 47(5), 685-688.
8. Naji Abhari, M., Ghodsian, M., Vaghefi, M. and Panahpur, N. (2010). "Experimental and numerical simulation of flow in a 90 degree bend" Flow Measurment and Instrumentation, 21(3), 292-298.
9. Kumar, U. C., Kothyari, K, G. and Ranga, R. (2012) "Flow structure and scour around circular componend bride piers - A review" Journal of Hydro-enviroment Research, 6(4), 261-265.
10. Ataie-Ashtiani, B. and Aslani-Kordkandi, A. (2012). "Flow field around side-by-side piers with and without a scour hole" European Journal of Mechanincs B/Fluids, 36, 152-166.
11. Das, S., Das, R. and Mazumdar, A. (2013). "Circuation characteristics of horseshoe vortex in scour region around circular piers" Water Science and Engineering, 6(1), 69-77.
12. Tang, X. and Knight, D.W. (2014). "The lateral distribution of depth-averaged velocity in a channel flow bend" Journal of Hydro-environment Research, 10, 1-10.
13. Vaghefi, M., Akbari, M. and Fiouz, A.R. (2015). "Experimental Study of Turbulence Kinetic Energy and Velocity Fluctuation Distributions in a 180 Degree Sharp Bend", 10th International Congress on Civil Engineering, University of Tabriz, Tabriz, Iran.
14. Vaghefi, M., Akbari, M. and Fiouz, A. (2016). "An experimental study of mean and turbulent flow in a 180 degree sharp open channel bend: Secondary flow and bed shear stress" KSCE Journal of Civil Engineering, 20(4), 1582-1593.
15. Haji Azizi, S., Davood, F., Hadi, A. and Akram A. (2016) "Numerical Simulation of Flow Pattern around the Bridge Pier with Submerged Vanes" Journal of Hydraulic Structures, 2(2), 46-61.
16. Ben Mohammad Khajeh, SH., Vaghefi, M. and Mahmoudi, A. (2017). "The scour pattern around an inclined cylindrical pier in a sharp 180-degree bend: an experimental study" International Journal of River Basin Management, 15(2), 207-218.
17. Karimi, N., Heidarnejad, M. and Masjedi, A. (2017). "Scour depth at inclined bridge piers along a straight path: A laboratory study" Engineering Science and Technology, an International Journal, 20(4), 1302-1307.

18. Dey, L., Barbhuiya, A. K, and Biswas, P. (2017). "Experimental study on bank erosion and protection using submerged vane placed at an optimum angle in a 180° laboratory channel bend" Geomorphology, 283, 32-40.

Journal of Hydraulic Structures
***J. Hydraul. Struct.*, 2018; 4(1): 75-90**
DOI: 10.22055/JHS.2018.25596.1073



OPEN ACCESS

Frequency domain analysis of transient flow in pipelines; application of the genetic programming to reduce the linearization errors

Mohammad Mehdi Riyahi[1]
Mostafa Rahmanshahi[2]
Mohammad Hadi Ranginkman[3]

Abstract

The transient flow analyzing by the frequency domain method (FDM) is computationally much faster than the method of characteristic (MOC) in the time domain. The FDM needs no discretization in time and space, but requires the linearization of governing equations and boundary conditions. Hence, the FDM is only valid for small perturbations in which the system's hydraulics is almost linear. In this study, the linearization errors of the FDM applied to a reservoir-pipe-valve system (RPV) are discussed and by using the Genetic Programming (GP), some correction coefficients are defined to reduce them. By applying the correction coefficient at the opening size of the valve, the first frequency of the frequency domain method is modified. Moreover, the responses at higher-order frequencies are evaluated by some new correction factors obtained by the GP. Solving an illustrative example shows that the error of the system can be significantly reduced by using the applied correction factors.

Keywords: Frequency domain, Transient flow, Method of characteristics, Genetic programming

Received: 22 March 2018; Accepted: 08 May 2018

1. Introduction

In addition to the traditional solution for solving the transient flow governing equations in pipelines by using the numerical methods such as the method of characteristic [1], the characteristics wave method [2], the finite element method [3], and the finite differences method [1]; they can also be solved by the transfer matrix method [4] and the impedance method [5] in

[1] M.Sc. graduated, Department of Civil Engineering, Shahid Chamran University of Ahvaz, Ahvaz, Iran, *mo_riyahi@yahoo.com* **(Corresponding author)**
[2] Ph.D. graduated, Department of Water Science Engineering, Shahid Chamran University of Ahvaz, Ahvaz, Iran, *mostafarahmanshahi@gmail.com*
[3] Ph.D. graduated, Department of Civil Engineering, Shahid Chamran University of Ahvaz, Ahvaz, Iran, *ha.ranginkaman@gmail.com*

CC BY

the frequency domain. The numerical methods in time domain need for discretization of the problem into the time and space and this increases the time of computations. While, in the frequency domain method since there is no need for discretization, the speed transit flow analysis is much higher than the time-domain numerical methods. This problem becomes more serious when a system has a complex mesh or needs to be connected to an optimization model. Another advantage of the frequency domain analysis is that the output of the frequency response function (FRF) does not depend on the type of the system excitation [6]. By applying different types of the excitations to a piping system in the time domain, the pressure head signal will result in different shapes. However, if the Fourier transform of the pressure head signal is taken and divided by the Fourier transform of the applied excitation, the FRF is obtained, which does not depend on the type of excitation. Compared to the characteristics method, the linearization of governing equations and boundary conditions in the frequency domain method (FDM) leads to creating errors in the output of this method. Nowadays the frequency domain is used for analyzing the water hammer phenomena [7-9], leak detection [10-12], and blockage detection [13, 14] is spread like the time domain[15] . Despite many conducted studies using the frequency domain a few studies have been carried out on the error of the frequency domain [16-19].

Lee et al. [16] showed that by increasing the valve opening size during the excitation, the system does not act as linear system and the linearization errors are increased. Lee and Vítkovský [17] introduced the dimensionless parameter, k, which was a criterion for measurement of the head loss at the valve, by dividing a pipe system into two states of friction dominant and valve dominant. For large values of k, the state of the valve is called valve dominant and for small k values, it is called the friction dominant. They represented that for the small values of k, the frequency response method (FRM) showed larger values compared to the method of characteristics, and when k has larger values, the FRM showed smaller values than the method of characteristics. They also investigated the generated errors between the characteristics method and the FRM by using a reservoir- pipe- valve (RPV) system. They indicated that in the openings less than 20%, the system did not show too many errors.

Lee [18] demonstrated that in the small excitations using a RPV system, the obtained values from using the transmission line model and characteristics model are similar. By increasing the magnitude of valve excitation, the created errors between the transmission line model and the characteristics model increases. Additionally, this paper demonstrates that the output of the transfer linear model has only one frequency, while the output of the characteristics model has the highest frequencies, causing a difference in the pressure head output at the time domain between two models. In this paper, the energy phase diagram was used to assess the created errors between the transfer linear model and characteristics model.

Riyahi and Haghighi [19] transmitted the linear equations of the frequency domain to the time domain; they replaced these equations in the MOC and compared them with the outputs of the frequency and full nonlinear MOC. It was concluded that the effect of the linearity or nonlinearity of the steady friction term in the frequency domain output is negligible and the main source of the error is the linear term of the valve equation. In addition, they showed that calibration in the frequency domain, unlike time domain, cannot be done with steady friction term; instead, it can be done with reforming of valve opening rate.

The main aim of this study is reducing the linearization errors of frequency domain analysis of transient flow in the pipeline using the soft computing model of genetic programming (GP). For this purpose, by applying the correction factors obtained by the GP to the valve opening, the output of the frequency domain has been corrected for the first frequency and higher-order

frequencies. Finally, the generality of the proposed modifications is evaluated through solving several different examples and the results are discussed.

2. Governing Equations and Valve Equation

2.1. Governing Equations

For analyzing the transient flow in pipelines, the governing equations must be solved. In many engineering problems, the governing equations on transient flows in elastic pipelines are as follows [20]:

$$\frac{\partial Q}{\partial t} + gA\frac{\partial H}{\partial x} + \frac{fQ|Q|}{2DA} = 0 \quad (1)$$

$$\frac{\partial H}{\partial t} + \frac{a^2}{gA}\frac{\partial Q}{\partial x} = 0 \quad (2)$$

where, Q is the discharge, H is the pressure head, g is the gravitational acceleration, A is the pipe cross-section area, D is the pipe diameter, f is the Darcy-Weisbach factor, and x is the location in pipe length.

There are two methods for the analysis of transient flows in the frequency domain; the transfer matrix method and the impedance method. In this study, the transfer matrix method is used, in order to maintain simplicity and easy understanding. In the transfer matrix method, the pressure head and discharge at the upstream and downstream of the system are related to each other through the transfer matrix.

The produced flows in the frequency domain are considered as oscillatory steady flows; therefore, in order to solve the governing equations on the transient flows in pipelines at the frequency domain, firstly, it must be assumed that the discharge, pressure head, and valve opening are equal to the average values plus their fluctuation values.

$$Q = Q_0 + q^* \quad (3)$$

$$H = H_0 + h^* \quad (4)$$

$$\tau = \tau_0 + \tau^* \quad (5)$$

where, Q_0, H_0, and τ_0 represent the average values and q^*, h^* and τ^* are the fluctuation values around the average value.

Now, by substituting Eqs. (3) to (5) into Eqs. (1) and (2), and eliminating the non-linear term of the momentum equation, the following equation is obtained.

$$\frac{\partial q^*}{\partial x} + \frac{gA}{a^2}\frac{\partial h^*}{\partial x} = 0 \quad (6)$$

$$\frac{\partial h^*}{\partial x} + \frac{1}{gA}\frac{\partial q^*}{\partial t} + \frac{fQ_0}{gDA^2}q^* = 0 \quad (7)$$

By applying the Fourier transform on Eqs. (6) and (7), the following equations can be written:

$$\frac{\partial q}{\partial x}+\frac{gA}{a^2}hj\omega=0 \tag{8}$$

$$\frac{\partial h}{\partial x}+\frac{1}{gA}qj\omega+\frac{fQ_0}{gDA^2}q=0 \tag{9}$$

where, q and h are the Fourier transform of q^* and h^* values. Also, ω is the angular frequency and $j=\sqrt{-1}$. By solving Eqs. (8) and (9), the following equations are obtained:

$$q_D=-\frac{h_U}{Z_c}\sinh(\mu x)+q_U\cosh(\mu x) \tag{10}$$

$$h_D=-Z_c q_U\sinh(\mu x)+h_U\cosh(\mu x) \tag{11}$$

$$z_c={(\mu a^2)}\Big/{(j\omega gA)} \tag{12}$$

$$\mu^2=\frac{aAj\omega}{a^2}\left(\frac{j\omega}{gA}+\frac{fQ_0}{gDA^2}\right) \tag{13}$$

where, Z_c and μ are called the characteristic impedance and the propagation constant, respectively. The subscripts *U* and *D* are also referred to as the upstream and downstream of the pipe, respectively. Thus, the field matrix with respect of Eqs. (10) to (13) can be written as follows:

$$\mathrm{F}=\begin{bmatrix}\cosh(\mu x) & -\frac{1}{Z_c}\sinh(\mu x) & 0\\ -Z_c\sinh(\mu x) & \cosh(\mu x) & 0\\ 0 & 0 & 1\end{bmatrix} \tag{14}$$

2.2. Valve Equation

The valve equation can be written as follows [4]:

$$\frac{Q}{Q_0}=\frac{C_dA}{(C_dA)_0}\left(\frac{H}{H_0}\right)^{1/2} \tag{15}$$

in which, C_d is the coefficient of discharge and $(C_dA)_0$, C_dA are equal τ_0 and τ, respectively. By replacing Eqs. (6) and (7) into the Eq. (15), the following equation can be achieved:

$$\left(1+\frac{q^*}{Q_0}\right)=\left(1+\frac{\tau^*}{\tau_0}\right)\left(1+\frac{h^*}{H_0}\right)^{1/2} \tag{16}$$

The Expression $\left(1+\frac{h^*}{H_0}\right)^{1/2}$ in Eq. (16) can be approximated by Taylor expansion.

$$\left(1+\frac{q^*}{Q_0}\right)=\left(1+\frac{\tau^*}{\tau_0}\right)\left(1+\frac{h^*}{H_0}\right)^{1/2}=$$

$$(1+\frac{\tau^*}{\tau})(1+\frac{1}{2}\frac{h^*}{H_0}-\frac{1}{8}\left(\frac{h^*}{H_0}\right)^2+\frac{3}{48}\left(\frac{h^*}{H_0}\right)^2+\cdots) \quad (17)$$

With removing the non-linear terms in Eq. (17), the following equation is obtained.

$$\left(1+\frac{q^*}{Q_0}\right)=1+\left(\frac{\tau^*}{\tau_0}\right)+\left(\frac{1}{2}\frac{h^*}{H_0}\right) \quad (18)$$

By applying the Fourier transform in Eq. (18), the following equation can be achieved:

$$h-\frac{2H_0}{Q_0}q+\frac{2H_0\Delta\tau}{\tau_0}=0 \quad (19)$$

in which, $\Delta\tau$ indicates the Fourier transform of τ^* and equals to maximum valve opening. The point matrix can be written using Eq. (19), as follows:

$$\mathrm{P}=\begin{bmatrix}1 & 0 & 0\\ -\frac{2H_0}{Q_0} & 1 & \frac{2H_0\Delta\tau}{\tau_0}\\ 0 & 0 & 1\end{bmatrix} \quad (20)$$

2.3. Overall Matrix

The overall matrix can be achieved by multiplying the point matrix to the field matrix. Accordingly, by multiplying Eq. (20) in Eq. (14), the overall matrix can be obtained, as follows:

$$U=\begin{bmatrix}1 & 0 & 0\\ -\frac{2H_0}{Q_0} & 1 & \frac{2H_0\Delta\tau}{\tau_0}\\ 0 & 0 & 1\end{bmatrix}\begin{bmatrix}\cosh(\mu x) & -\frac{1}{Z_c}\sinh(\mu x) & 0\\ -Z_c\sinh(\mu x) & \cosh(\mu x) & 0\\ 0 & 0 & 1\end{bmatrix} \quad (21)$$

3. Genetic Programming

The GP is one of the branches of artificial intelligence and nowadays it has been applied in many water engineering researches [21, 22]. The best relationship between outputs can be obtained by applying several steps through data-driven models [23]. One of the branches of data-driven models is artificial intelligence. Artificial intelligence is a computational approach that solves the problems based on the imitation of human learning [24]. Methods like artificial neural networks (ANNs) and GP are the branches of artificial intelligence. The model recognition methods can be categorized based on colour, including [25]; (a) White Box: these methods are based on physical and mathematical relationships, (b) Black Box: these models are data-driven models, in which the relationship between inputs and outputs

of a system is unknown, and (c) Grey box: they are conceptual systems that create a mathematical relationship between inputs and outputs of a system and make it available for the users. According to the above-mentioned categories, GP and ANNs are considered as the grey and black categories, respectively.

GP is an evolutionary computation method which solves the problem without knowing the solution and/or recognition of it by the user [26]. GP is derived from the genetic algorithm (GA) method and treats according to the genetic rules. This model was first discovered by Carmer [27]; then developed by Koza [28]. The difference between the GA and GP method is that the GA method is used to find the best value for a series of parameters for the model, while the GP provides a structure to associate the input data to the output data [23]. In fact, the GA optimizes the parameters, whereas the GP performs the modelling. In GP firstly, a population from the computer programs is generated using one of the three, full, Growing, and ramped half-and-half methods. A program, which is formed in the GP method, consists of two main parts, terminals and functions. The terminals include non-numeric and numeric variables and the functions include mathematical operators and functions, Boolean operators, and logical expressions. The output of a program can be illustrated like a tree (Fig. 1). Functions and terminals have been shown in the Fig. 1. Functions are placed in the middle points and terminals in the branches.

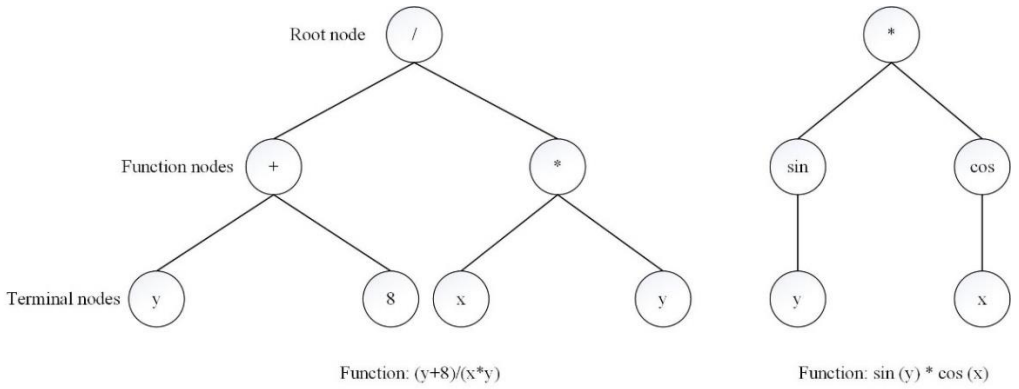


Fig. 1 GP structure

After generating the initial population from the programs, the parents are selected based on their fitness. The fitness value is usually obtained according to the errors created between the predicted and observed values. Parent selection is performed based on the fitness and by using one of the three methods of Roulette Wheel, Ranking, and Tournament. After selecting the parents, one of the three Crossover, Mutation, or Reproduction methods is used for creating the next generation. The single point crossover method is chosen as the crossover point for both parents. Then, the new offspring is produced with a combination of two sub-roots of the chosen location. The crossover method is shown in Fig. 2. The mutation method has different types, where, the point mutation method is one of the common types. In this method, one point in a tree is randomly selected as a mutation point and if that point is a function, it is converted to another function and, similarly, if it is a terminal, it is converted to another terminal. Another type of mutation is a sub-tree mutation. In this method, one point of the tree is selected as the mutation point; then, all of the members below this point are substituted by new members. The point mutation method has been

shown in Fig. 3. In the reproduction method, a program is selected based on fitness and it is transferred to the next generation. After creating the new generation, the same cycle as described above is repeated until the number of iterations is finished; then, the best program among the available programs is selected in accordance with fitness.

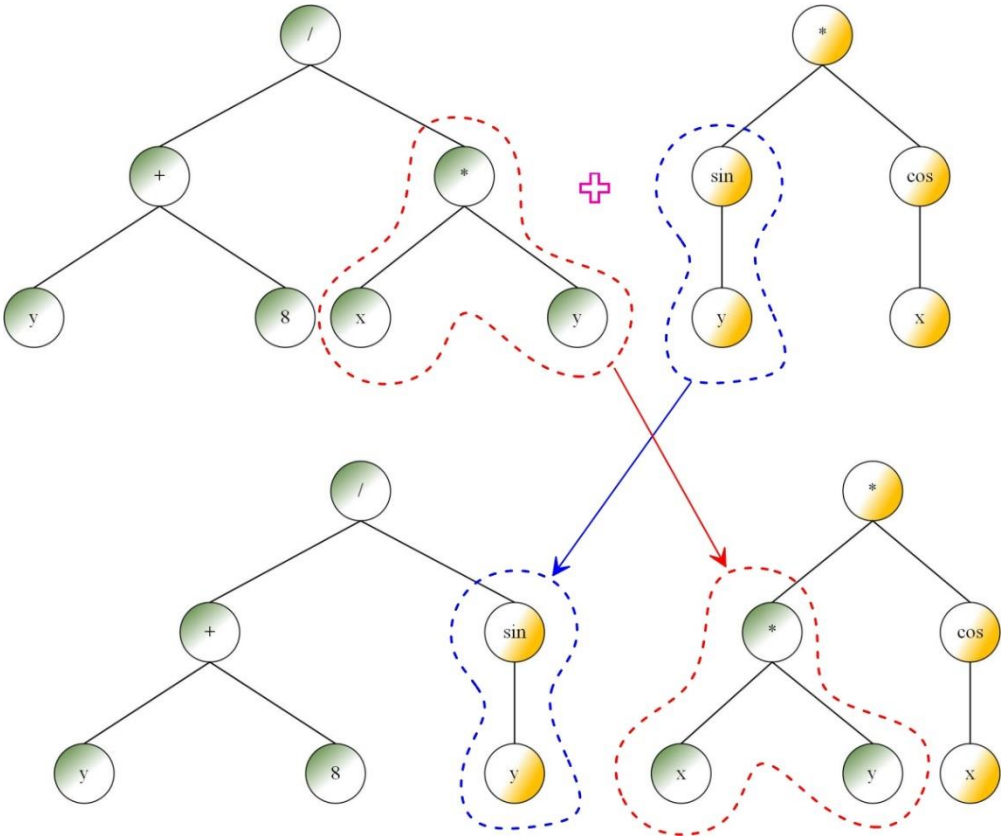


Fig. 2 Example of Crossover method in GP

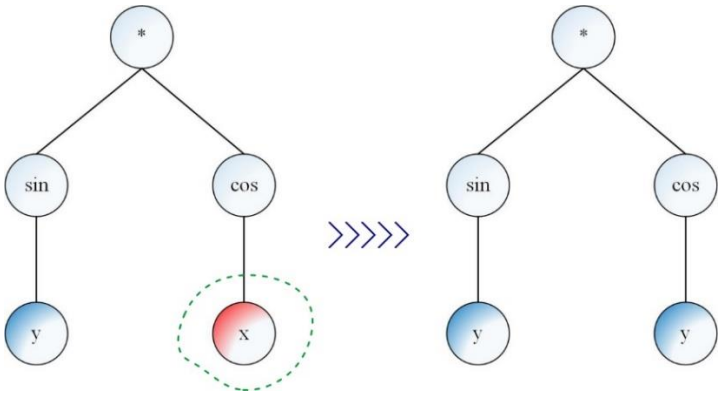


Fig. 3 Example of point mutation

4. Reducing Error with Genetic Programming

In this research, as shown in Fig. 4, a simple RPV system was used. This system is consists of a reservoir with 50 m head at its upstream, a pipe with 1000 m length, 250 mm diameter, Darcy friction factor of 0.021 and wave speed of 1000 ms^{-1}. The excitation is produced by the valve which is sinusoidal excited and is located at the end of RPV system.

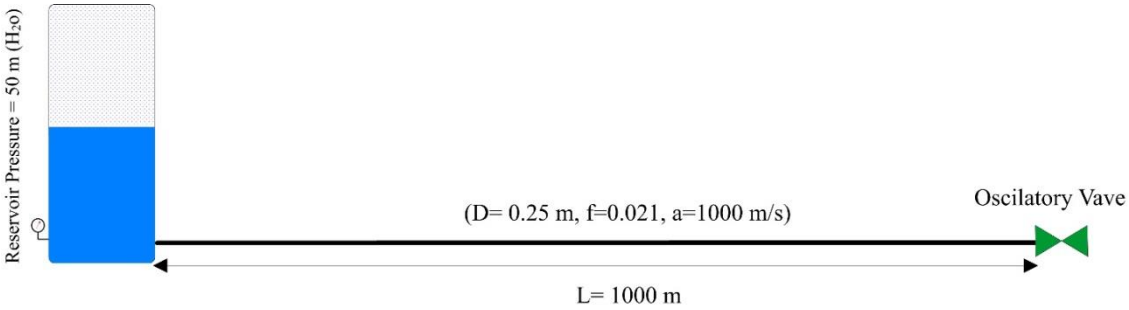


Fig. 4 Reservoir-Pipe-Valve system

The results of the FDM have been compared with the results of the MOC in Fig. 5, using the provided system in Fig. 4. In this system, the valve has been excited sinusoidal with the theoretical frequency of the system f_{thr} which is equal to $a/4L$ and C_d is 0.8. The results have been compared at the location of the valve and the Fast Fourier Transformation (FFT) has been used for transferring the obtained pressure heads from the characteristic method to the frequency domain. Fig. 5 indicates, that the frequency domain only produces the first frequency which is not equal to the output of the characteristic method, due to the large excitation of the valve. Thus, the FDM needs to produce and correct higher-order frequencies in addition to the correction of the first frequency.

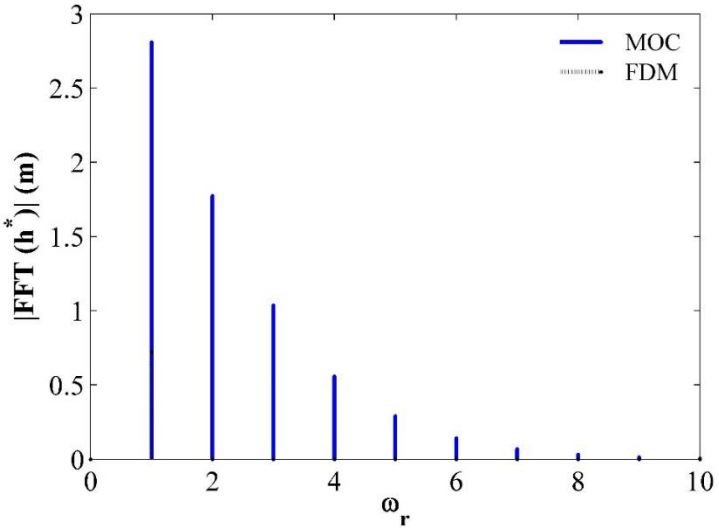


Fig. 5 Comparison of the responses between MOC & FDM

It can be mentioned that the results of the FDM and the MOC are periodically repeated. Therefore, the existing system in Fig. 4 is used and the error between the FDM and the MOC is

obtained for frequencies 1 to 12 and discharge coefficients 0.3, 0.5, and 0.8 (Fig. 6). Consequently, the corrections can be made for a frequency interval and the other frequencies can also be corrected by the similar corrected frequencies. In this research, the frequency intervals ranging from 1 to 3 have been corrected.

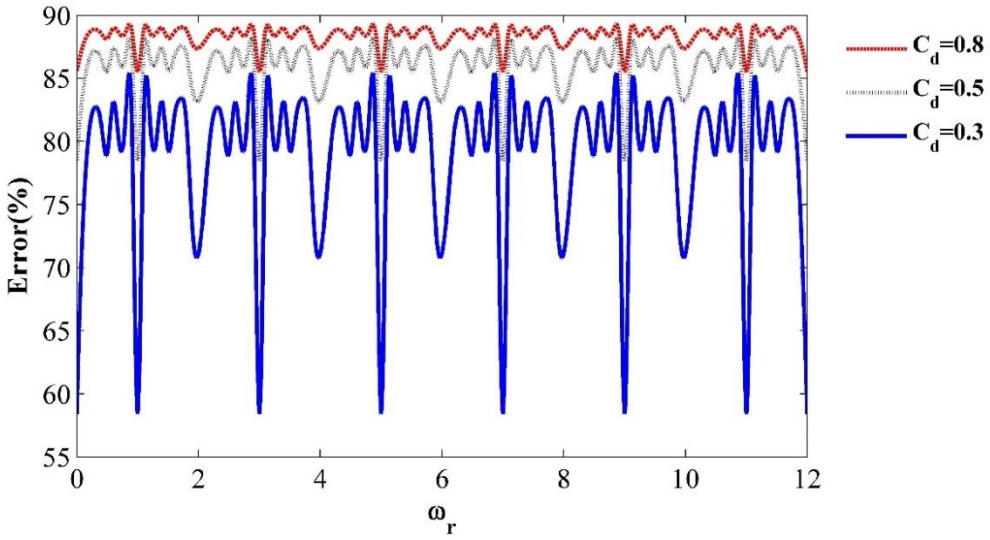


Fig. 6 The linearization error of the FDM for ω_r from 0 to 12 and coefficient of discharge 0.3, 0.5 and 0.8

For correction of the output frequencies, a correction coefficient (α) is multiplied to the valve opening. Since, the correction coefficient is considered in the valve relationships in the transfer matrix method; as a result, the point matrix is changed, and it can be rewritten as follows:

$$\mathrm{P} = \begin{bmatrix} 1 & 0 & 0 \\ -\dfrac{2H_0}{Q_0} & 1 & \dfrac{2\alpha H_0 \Delta\tau}{\tau_0} \\ 0 & 0 & 1 \end{bmatrix} \tag{22}$$

Due to the changes in the point matrix, the overall matrix is also changed. The overall matrix can be rewritten as follows.

$$U = \begin{bmatrix} 1 & 0 & 0 \\ -\dfrac{2H_0}{Q_0} & 1 & \dfrac{2\alpha H_0 \Delta\tau}{\tau_0} \\ 0 & 0 & 1 \end{bmatrix} \begin{bmatrix} \cosh(\mu x) & -\dfrac{1}{Z_c}\sinh(\mu x) & 0 \\ -Z_c \sinh(\mu x) & \cosh(\mu x) & 0 \\ 0 & 0 & 1 \end{bmatrix} \tag{23}$$

According to Eqs. (22) and (23), when the correction coefficient equals 1, the same equations described before, are achieved. The following steps are considered for computing the value of α,. The relevant flowchart is represented in Fig. 7;

a) First, the MOC is applied to the situation that the valve is excited sinusoidal with a specific frequency, a given opening size and discharge coefficient.
b) A FFT is taken from the fluctuations of pressure head around the average value at the valve location.

c) Then, each obtained amplitude at each output frequency is set equal to the output of the FDM.
d) The value of q is calculated by the following formula. Notice that the value of h has been calculated from the previous step.

$$q = \frac{h}{-Z_C}\sinh(\mu x) \tag{24}$$

e) The value of α is calculated as follows:

$$\alpha = q\left(-Z_C\ \sinh(\mu x) - \frac{2H_0}{Q_0}\cosh(\mu x)\right)\left(\frac{-\tau_0}{2H_0\Delta\tau}\right) \tag{25}$$

The value of α has been calculated for the values of Δτ and C_d from 0.1 to 0.8 and values of ω from 1 to 3. Then, the data has been divided into two categories of training and test data; afterwards, using the GP method, four equations have been achieved for α based on the input and output frequency, valve opening, and discharge coefficient, these equations are α_1, α_2, α_3 and α_4 which are related to the first frequency, frequencies 2 and 3, frequencies 4 to 6 and frequencies 7 to 10, respectively. The determined parameters in the GP method are expressed in Table 1:

Table1. The determined parameters in the GP method

Parameter	Setting of parameter
Population size	300
Number of generations	650
Maximum depth size of a tree	3
Total nodes	inf
Function set	+, -, ×, power, log, ln, atan, tan, tanh, sin
Tournament size	3
Maximum numbers of genes	4
the range of constant input numbers	[-10,10]

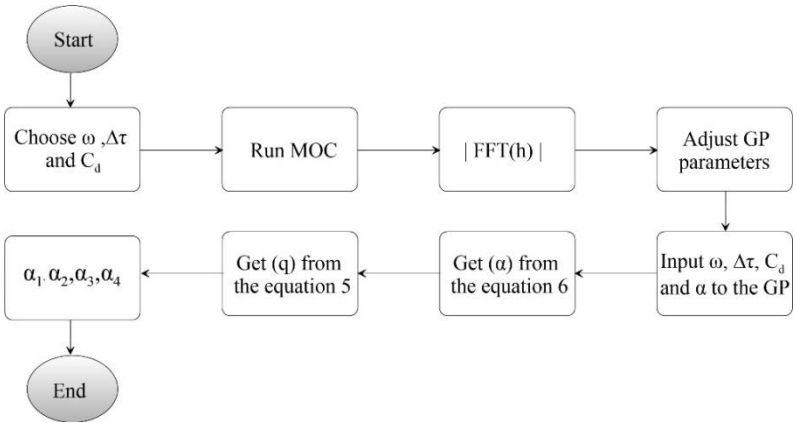


Fig 7. flowchart of the α value computation

In this study, the GP is implemented by means of MATLAB toolbox (GPTIPS2).[29, 30]

The equations for the correction coefficients, α, are given as follows. Moreover, the values of determination coefficient for each equation are 0.94, 0.95, 0.93, and 0.90, respectively.

$$\alpha_1 = 12.5 * \sin(\Delta\tau^{4.3} * \tan(C_d)) - 0.93 * \sin\left(\text{atan}(C_d)^{\text{atan}(\omega_{in})}\right) + 1.62 \quad (26)$$

$$\alpha_2 = 5.4 * \tan(\tan(\Delta\tau)) * \tanh(\tanh(C_d)) - 4.63 * \tan(\Delta\tau) * \tanh(C_d) - 1.5 * \log(\omega_{out})^{\tan(\tanh(\Delta\tau))} + 1.56 \quad (27)$$

$$\alpha_3 = 7.4 * x1^{2*\omega_{out}} \text{atan}(C_d) + 0.66 * \tanh(\Delta\tau)^{\omega_{out}} - 2\exp(-3) \quad (28)$$

$$\alpha_4 = 10.7 * \Delta\tau^{2*\omega_{out}} * \log(\omega_{out}) * \sin(C_d) - 2.81 * \Delta\tau * x1^{2*\omega_{out}} \omega_{out} * \sin(C_d) + 6.15 * 10^{-4} \quad (29)$$

5. Examples

To investigate the efficiency of the obtained correction coefficients and their generality in different situations the provided systems in Table 2 have been used. In these examples, the systems with different properties like the length, wave speed, Darcy- Weisbach factor have been used that are presented in Table 2. In all examples, oscillatory-state flows are generated by sinusoidal exciting the vale.

Each system is implemented one time using the MOC, then the obtained fluctuations of the pressure head are transferred into the frequency domain by the FFT. The pressure head amplitudes obtained by the MOC are adopted as the exact solutions. After that, each system has been implemented by the standard FDM (SFDM) and modified FDM (MFDM). Finally, the results of the SFDM and MFDM are compared with MOC.

Table 2. Examples of the RPV systems

Example	a (m/s)	d (m)	L (m)	f	H_{up} (m)	C_d	ω_r	$\Delta\tau$
1	1000	0.25	1000	0.021	50	1	1	0.8
2	1200	0.4	1000	0.022	10	1	2.5	0.8
3	800	0.3	800	0.02	20	0.5	1.5	0.5
4	1000	0.45	1000	0.02	30	0.8	2	0.6
5	1200	0.25	1200	0.022	50	0.3	2.5	0.3
6	1100	0.25	900	0.022	10	0.3	1	0.8
7	1200	0.35	800	0.022	40	1	2	0.6
8	1000	0.15	1000	0.02	20	0.2	2.5	0.2
9	800	0.25	900	0.02	35	0.5	1.4	0.7
10	1000	0.2	800	0.021	22	0.4	2.3	0.6
11	1200	0.1	600	0.018	40	0.95	1.7	0.4
12	1100	0.15	1000	0.02	50	0.5	2.6	0.3

As earlier discussed, the system's nonlinearities not only cause the FRM to under predict or over predict the system response at the excitation frequency but also produces responses at higher-order frequencies which are completely missed by the SFRM. In this research with introducing correction factor that is named α_1 can reform the first frequency of SFDM. To generate higher-order frequencies, these frequencies are made like the first frequency. Then by applying correction coefficients that are named α_2, α_3 and α_4 they can be approximated to their

actual values. The output of SFDM, MFDM and MOC are shown in Fig. 8.

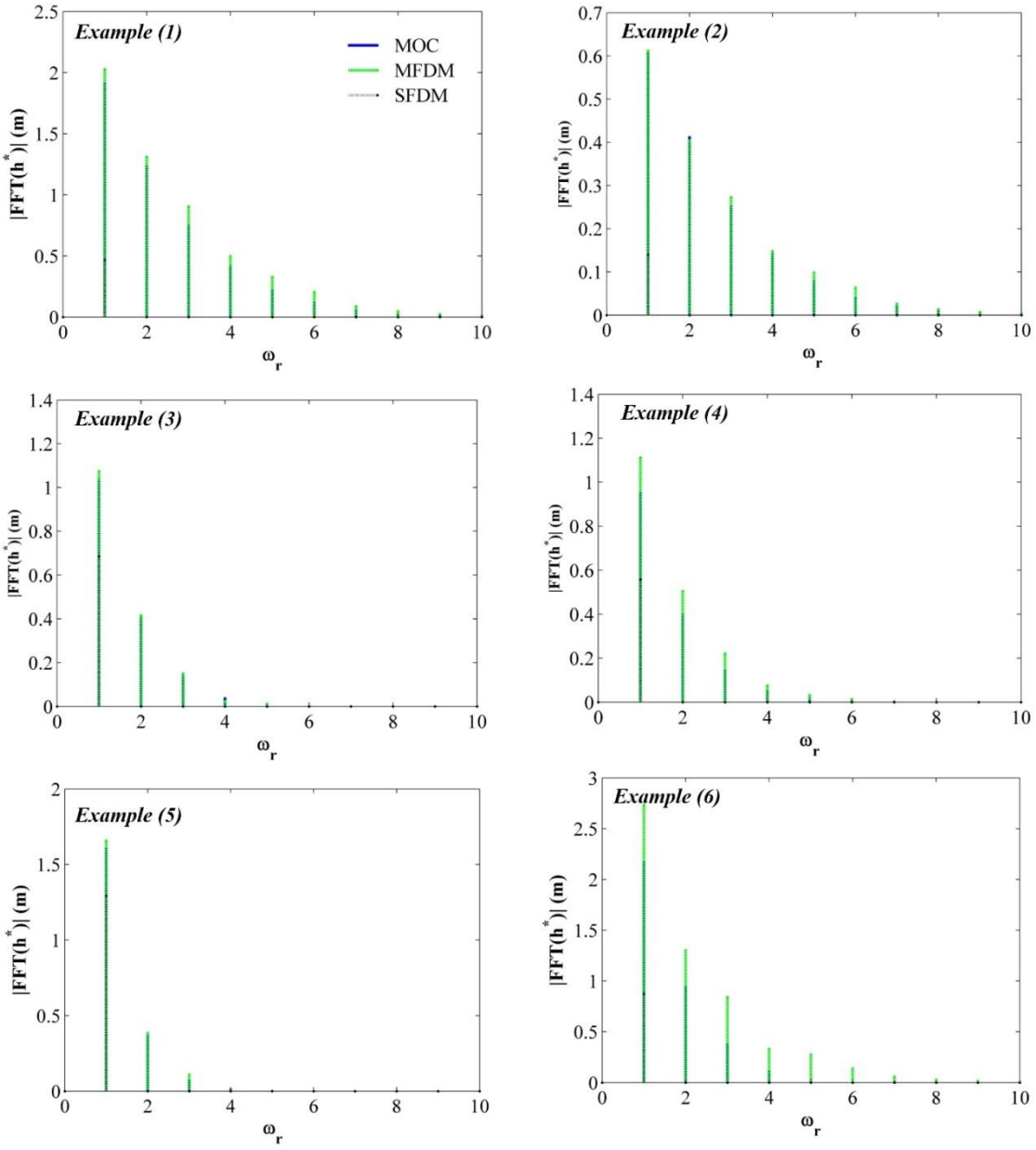
Table 3 represents the errors between the MOC and the SFDM, as well as the errors between the MOC and the MFDM for the first frequency output. This table shows a significant reduction in errors by applying correction coefficients in the SFDM.

Table 3. Error between MOC and SFDM and also MOC and MFDM in the first frequency output

Example	Error between MOC & SFDM (ω_1)	Error between MOC & MFDM (ω_1)
1	75.67	6.06
2	76.99	0.3
3	33.69	4.16
4	41.29	16.74
5	19.38	3.26
6	59.72	25.59
7	44.64	11.98
8	17.73	1.65
9	60.16	0.016
10	45.32	2.47
11	23.27	5.16
12	16.52	6.82

6. Conclusion

Despite the advantages of the FDM, such as fast computations and providing more insight towards the system, it suffers from a big limitation that is the linearization of the non-linear equations. Linearization causes this method to only have an exact response for small excitations and when the system loses its linearization state, it is not able to make accurate predictions. Furthermore, this method is not capable to produce higher-order frequencies. Despite increasing the application growth of the frequency domain in water engineering; Althogh currently, there are few investigations on reducing the frequency domain errors. In this study, by using GP which has been one of the most widely used tools in the recent years in various fields such as water engineering, it is possible to correct the response output of the frequency domain for the first frequency and for higher frequencies, they can be corrected after producing each of them. This correction coefficient depends on the input and output frequencies, valve opening, and discharge coefficient. The coefficient obtained from GP is multiplied to the valve opening; then by correcting the relevant output, the FRM is improved. In accordance with the mentioned examples, in the worst situation, the error value of the first frequency has decreased from 76.98 to 0.3 %.


Example (1)
MOC
MFDM
SFDM
|FFT(h*)| (m)
ωr
Example (2)
Example (3)
Example (4)
Example (5)
Example (6)

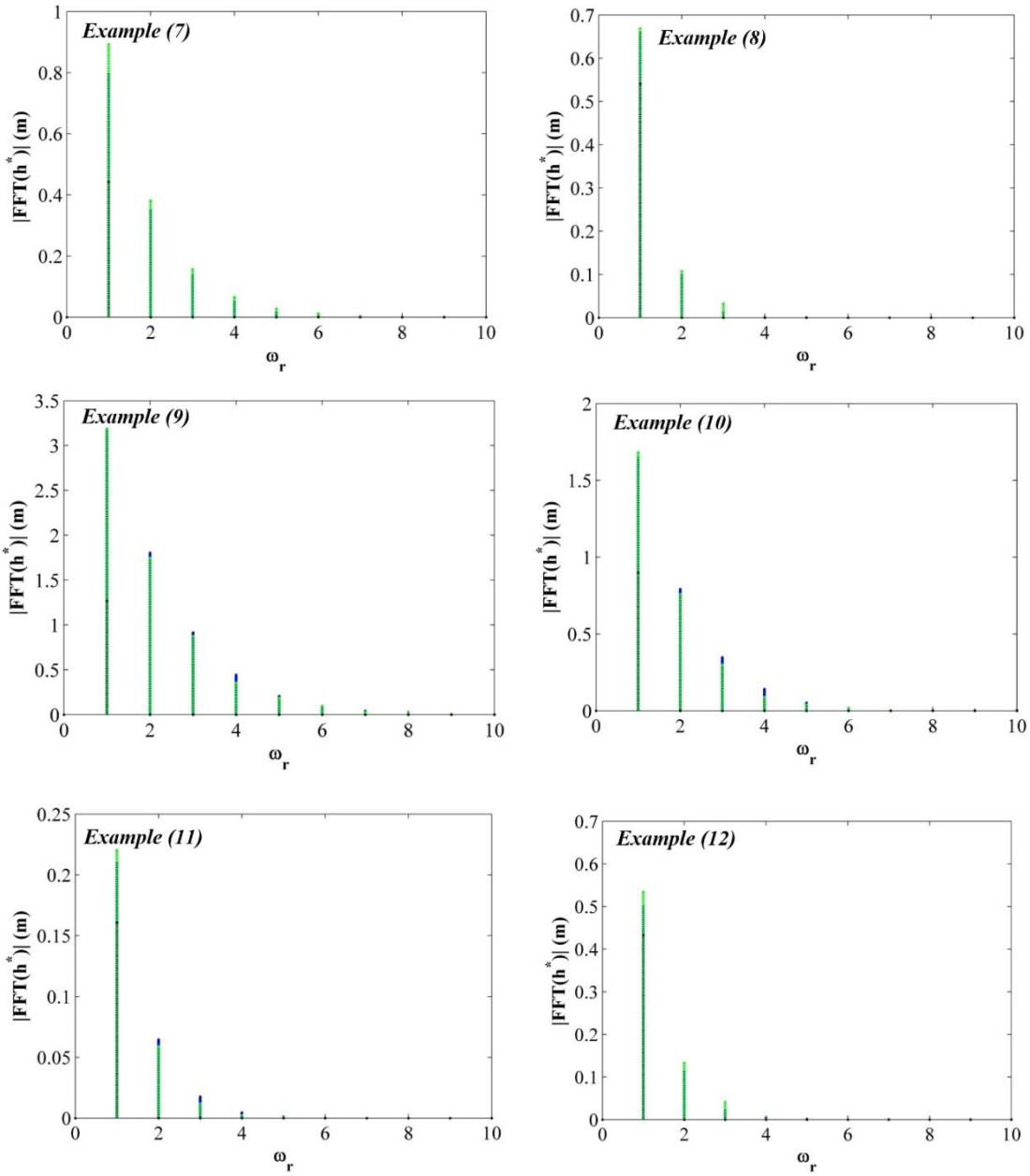


Fig. 8 Responses of the examples in the frequency domain

References

1. Izquierdo J, Iglesias P, (2002). Mathematical modelling of hydraulic transients in simple systems. Mathematical and Computer Modelling, pp: 801-812.
2. Wood D.J, et al., (2005). Numerical methods for modeling transient flow in distribution systems. Journal (American Water Works Association), pp: 104-115.
3. Zhao M, Ghidaoui MS, (2004). Godunov-type solutions for water hammer flows. Journal of Hydraulic Engineering, pp: 341-348.
4. Chaudhry, M.H., Applied Hydraulic Transients, Springer New York, 2013.

5. Wylie E.B., Streeter V.L., and Suo L., Fluid transients in systems. Prentice Hall Englewood Cliffs, NJ, Vol. 1. 1993.
6. Lee P.J, et al., (2013). Frequency domain analysis of pipe fluid transient behaviour. Journal of hydraulic research, pp: 609-622.
7. Kim S.-H., (2010). Design of surge tank for water supply systems using the impulse response method with the GA algorithm. Journal of Mechanical Science and Technology, pp: 629-636.
8. Ranginkaman MH, Haghighi A, and Samani H.M.V, (2017). Application of the Frequency Response Method for Transient Flow Analysis of Looped Pipe Networks. International Journal of Civil Engineering, pp: 677-687.
9. Riasi A, Nourbakhsh A, and Raisee M, (2010). Numerical modeling for hydraulic resonance in hydropower systems using impulse response. Journal of Hydraulic Engineering, pp. 929-934.
10. Capponi C, et al., (2017). Leak Detection in a Branched System by Inverse Transient Analysis with the Admittance Matrix Method. Water Resources Management, pp: 1-15.
11. Ferrante M, et al., (2016). Numerical transient analysis of random leakage in time and frequency domains. Civil Engineering and Environmental Systems, pp: 70-84.
12. Ranginkaman M, Haghighi A, and Vali Samani H, (2016). Inverse frequency response analysis for pipelines leak detection using the particle swarm optimization. Iran University of Science & Technology, pp: 1-12.
13. Duan H, et al., (2014). Transient wave-blockage interaction and extended blockage detection in elastic water pipelines. Journal of fluids and structures, pp: 2-16.
14. Duan H.-F., et al., (2013). Extended blockage detection in pipes using the system frequency response: analytical analysis and experimental verification. Journal of Hydraulic Engineering, pp: 763-771.
15. Bergant A, et al., (2013). Waterhammer tests in a long PVC pipeline with short steel end sections. Journal of Hydraulic Structures, pp: 24-36.
16. Lee PJ, et al., (2003). Leak detection in pipes by frequency response method using a step excitation: By WITNESS MPESHA, M. HANIF CHAUDHRY, and SARAH L. GASSMAN, Journal of Hydraulic Research, pp: 55-62.
17. Lee PJ, and Vítkovský JP, (2010). Quantifying linearization error when modeling fluid pipeline transients using the frequency response method. Journal of Hydraulic Engineering, pp: 831-836.
18. Lee, PJ, (2013). Energy analysis for the illustration of inaccuracies in the linear modelling of pipe fluid transients. Journal of Hydraulic Research, pp: 133-144.
19. Riyahi M.M, Haghighi A, (2018). Investigation of error resources in the transient flow simulation of pipelines in the frequency domain using the transfer matrix method, Modares Mechanical Engineering, pp: 10-18 (in Persian).
20. Ghidaoui M.S, et al., (2005).A review of water hammer theory and practice. Applied Mechanics Reviews, pp: 49.
21. Bozorg-Haddad O, Soleimani S, and Loáiciga HA, (2017). Modeling Water-Quality Parameters Using Genetic Algorithm–Least Squares Support Vector Regression and Genetic Programming. Journal of Environmental Engineering, pp: 04017021.
22. Pourzangbar A, et al., (2017). Predicting scour depth at seawalls using GP and ANNs. Journal of Hydroinformatics, pp: 349-363.
23. Gandomi A.H., Alavi A.H., and Ryan C., Handbook of genetic programming applications. Springer, 2015.

24. Flood I, (2008). Towards the next generation of artificial neural networks for civil engineering. Advanced Engineering Informatics, pp: 4-14.
25. Giustolisi O, et al., (2007). A multi-model approach to analysis of environmental phenomena. Environmental Modelling & Software, pp: 674-682.
26. Poli R, Langdon W, and McPhee N, (2008). A field guide to genetic programming (With contributions by JR Koza). Published via http://lulu.com .
27. Cramer N.L., A representation for the adaptive generation of simple sequential programs. in Proceedings of the first international conference on genetic algorithms. 1985.
28. Koza J.R., Genetic programming: on the programming of computers by means of natural selection, MIT press, 1992.
29. Searson D.P., Leahy D.E. Willis M.J. (2010). GPTIPS: an open source genetic programming toolbox for multigene symbolic regression. in Proceedings of the International multiconference of engineers and computer scientists.
30. Searson D.P., Leahy D.E., Willis M.J. (2011). Predicting the toxicity of chemical compounds using GPTIPS: a free genetic programming toolbox for MATLAB, in Intelligent Control and Computer Engineering. Springer.

نشریه تخصصی

سازه های هیدرولیکی

صاحب امتیاز: دانشگاه شهید چمران اهواز

مدیر مسئول: دکتر حمیدرضا غفوری
سردبیر: دکتر علی حقیقی
مدیر داخلی: دکتر سید محمد اشرفی
گروه مهندسی عمران، دانشکده مهندسی، دانشگاه شهید چمران اهواز، اهواز، ایران

دارای اعتبار **علمی پژوهشی** از وزارت علوم تحقیقات و فناوری

Print ISSN: 2345-413X
Online ISSN: 2345-5156

اعضای هیأت تحریریه

دکتر حسین محمدولی سامانی
گروه مهندسی عمران، دانشکده مهندسی، دانشگاه شهید چمران اهواز
(تخصص: سازه های هیدرولیکی)

دکتر محمود شفاعی بجستان
گروه سازه های آبی، دانشکده مهندسی علوم آب، دانشگاه شهید چمران اهواز
(تخصص: سازه های هیدرولیکی)

دکتر علی حقیقی
گروه مهندسی عمران، دانشکده مهندسی، دانشگاه شهید چمران اهواز
(تخصص: آب و فاضلاب و هیدرولیک)

دکتر محمدسیروس پاکباز
گروه مهندسی عمران، دانشکده مهندسی، دانشگاه شهید چمران اهواز
(تخصص: ژئوتکنیک)

دکتر سعیدرضا صباغ یزدی
دانشکده مهندسی عمران، دانشگاه صنعتی خواجه نصیرالدین طوسی (تخصص: سازه های هیدرولیکی و مدلسازی عددی)

دکتر مجتبی لبیب زاده
گروه مهندسی عمران، دانشکده مهندسی، دانشگاه شهید چمران اهواز (تخصص: سازه و سازه های هیدرولیکی)

دکتر هلنا راموس
گروه مهندسی عمران، دانشگاه لیسبون پرتغال (تخصص: هیدرولیک سیستم های تحت فشار و هیدروانفورماتیک)

دکتر عبدالرسول تلوری
گروه مهندسی عمران، دانشگاه آزاد اسلامی، واحد تهران شمال
(تخصص: هیدرولوژی و منابع آب)

دکتر آرش ادیب
گروه مهندسی عمران، دانشکده مهندسی، دانشگاه شهید چمران اهواز
(تخصص: هیدرولوژی و منابع آب)

دکتر سید عباس حق شناس
گروه فیزیک فضا، موسسه ژئوفیزیک دانشگاه تهران (تخصص: سواحل و بنادر)

دکتر محمد واقفی
گروه مهندسی عمران، دانشکده فنی و مهندسی، دانشگاه خلیج فارس (تخصص: سازه های هیدرولیکی)

دکتر محمد ذونعمت کرمانی
بخش مهندسی آب، دانشگاه شهید باهنر کرمان (تخصص: هیدرولیک محاسباتی)

دکتر طاهر رجایی
گروه مهندسی عمران، دانشکده فنی و مهندسی، دانشگاه قم (تخصص: آب و محیط زیست)

Journal of
Hydraulic Structures
Scientific Professional Journal

Contents

Volume 4, Issue 1, Summer 2018

Development of a Direct Explicit Equation for Hydraulic Design of Semi-elliptical Channels (1-7)
H. Nikroy Motlagh; Hossein M.V. Samani; H. Hassanpour Darvishi

An Alternating Direction Implicit Method for Modeling of Fluid Flow (8-18)
I. Saeedpanah; A. Adib

Wave Evolution in Water Bodies using Turbulent MPS Simulation (19-35)
H. Imanian; M. Kolahdoozan; A.R. Zarrati

Ocean Currents Modeling along the Iranian Coastline of the Oman Sea and the Northern Indian Ocean (36-54)
M. Jedari Attari; S.A. Haghshenas; A. Bakhtiari; M.H. Nemati

Study of Streamlines under the Influence of Displacement of Submerged Vanes in Channel Width, and at the Upstream Area of a Cylindrical Bridge Pier in a 180 Degree Sharp Bend (55-74)
C.A. Chooplou; M. Vaghefi; S.H. Meraji

Frequency domain analysis of transient flow in pipelines; application of the genetic programming to reduce the linearization errors (75-90)
M.M. Riyahi; M. Rahmanshahi; M.H. Ranginkaman

Address:
Department of Civil Engineering, Faculty of Engineering,
Shahid Chamran University of Ahvaz
Phone: +986133330011, +986133330012
Website: jhs.scu.ac.ir
Email: jhs@scu.ac.ir
Ahvaz, Khouzestan Province, Iran